

Electronic Properties of Quantum Wire Networks

Thesis submitted in partial fulfillment
of the requirements for the degree of
DOCTOR OF PHILOSOPHY

by

Igor Kuzmenko

Submitted to the Senate of Ben-Gurion University
of the Negev

August 29, 2005

Beer-Sheva

Electronic Properties of Quantum Wire Networks

Thesis submitted in partial fulfillment
of the requirements for the degree of
DOCTOR OF PHILOSOPHY

by

Igor Kuzmenko

Submitted to the Senate of Ben-Gurion University
of the Negev

Approved by the advisor

Approved by the Dean of the Kreitman School of Advanced Graduate Studies

August 29, 2005

Beer-Sheva

This work was carried out under the supervision of Prof. Yshai Avishai

In the Department of Physics

Faculty of Natural Sciences

Acknowledgments

I am grateful to my advisers Professor Sergey Gredeskul, Professor Konstantin Kikoin, and Professor Yshai Avishai for their guidance, help and many hours of fruitful discussions.

Abstract

Quantum wire networks are novel artificial nano-objects that represent a two dimensional ($2D$) grid formed by superimposed crossing arrays of parallel conducting quantum wires, molecular chains or metallic single-wall carbon nanotubes. Similar structures arise naturally as crossed striped phases of doped transition metaloxides. The mechanical flexibility of the networks, the possibility of excitation of some of their constituents (a nanotube or a single wire) by external electric field, and the existence of bistable conformations in some of them (molecular chain) make the networks one of the most attractive architectures for designing molecular-electronic circuits for computational application.

Since such networks have the geometry of crossbars, we call them “quantum crossbars” (QCB). Spectral properties of QCB cannot be treated in terms of purely $1D$ or $2D$ electron liquid theory. A constituent element of QCB (quantum wire or nanotube) possesses the Luttinger liquid (LL) fixed point. A single array of parallel quantum wires is still a LL-like system qualified as a sliding LL phase provided only the density-density or/and current-current interaction between adjacent wires is taken into account. Two crossing arrays (QCB) coupled only by capacitive interaction in the crosses have similar low-energy, long-wave properties characterized as a crossed sliding LL phase. QCB with electrostatic interaction in the crosses possess a cross-sliding Luttinger liquid (CSLL) zero energy fixed point.

In this Thesis we develop a theory of interacting Bose excitations (plasmons) in a superlattice formed by m crossed arrays of quantum wires. The subject of the theory is the spectrum of excitations and response functions in the $2D$ Brillouin zone so it goes far beyond the problem of stability of the CSLL fixed point.

In the first part we analyze spectrum of boson fields and two-point correlators in double ($m = 2$) square QCB [double tilted and triple ($m = 3$) QCB are considered in Appendices C and D, respectively]. We show that the standard bosonization procedure is valid, and the system behaves as a cross-sliding Luttinger liquid in the infrared limit, but the high frequency spectral and correlation characteristics have either $1D$ or $2D$ nature depending on the direction of the wave vector in the $2D$ elementary cell of reciprocal lattice. As a result, the crossover from $1D$ to $2D$ regime may be experimentally observed. It manifests itself as appearance of additional peaks of optical absorption, non-zero transverse space correlators and periodic energy transfer between arrays (“Rabi oscillations”).

In the second part, the effectiveness of infrared (IR) spectroscopy is studied. IR spectroscopy can be used as an important and effective tool for probing QCB at finite frequencies far from the LL fixed point. Plasmon excitations in QCB may be involved in resonance diffraction of incident electromagnetic waves and in optical absorption in the IR part of

the spectrum. The plasmon velocity is much smaller than the light velocity. Therefore, an infrared radiation incident on an *isolated* array, cannot excite plasmons at all. However in QCB geometry, each array serves as a diffraction lattice for its partner, giving rise to Umklapp processes of reciprocal super-lattice vectors. As a result, excitation of plasmons in the center of the Brillouin zone (BZ) occurs.

To excite QCB plasmons with non-zero wave vectors, an additional diffraction lattice (DL) coplanar with the QCB can be used. Here the diffraction field contains space harmonics with wave vectors perpendicular to the DL that enable one to eliminate the wave vector mismatch and to scan plasmon spectrum within the BZ. In the general case, one can observe single absorption lines forming two equidistant series. However, in case where the wave vector of the diffraction field is oriented along some resonance directions, additional absorption lines appear. As a result, an equidistant series of split doublets can be observed in the main resonance direction (BZ diagonal). This is the central concept of dimensional crossover mentioned above with direction serving as a control parameter. In higher resonance directions, absorption lines form an alternating series of singlets and split doublets demonstrating new type of dimensional crossover. The latter occurs in a given direction with frequency as a control parameter.

In the third part, dielectric properties of QCB interacting with semiconductor substrate are studied. It is shown that a capacitive contact between QCB and a semiconductor substrate does not destroy the Luttinger liquid character of the long wave QCB excitations. However, the dielectric losses of a substrate surface are drastically modified due to diffraction processes on the QCB superlattice. QCB-substrate interaction results in additional Landau damping regions of the substrate plasmons. Their existence, form and the spectral density of dielectric losses are sensitive to the QCB lattice constant and the direction of the wave vector of the substrate plasmon. Thus, the dielectric losses in the QCB-substrate system serve as a feasible tool for studying QCB spectral properties.

In the fourth part we formulate the principles of ultraviolet (UV) spectroscopy, i.e., Raman-like scattering. UV scattering on QCB is an effective tool for probing QCB spectral properties, leading to excitation of QCB plasmon(s). Experimentally, such a process corresponds to sharp peaks in the frequency dependence of the differential scattering cross section. The peak frequency strongly depends on the direction of the scattered light. As a result, $1D \rightarrow 2D$ crossover can be observed in the scattering spectrum. It manifests itself as a splitting of single lines into multiplets (mostly doublets). The splitting magnitude increases with interaction in the QCB crosses, while the peak amplitudes decrease with electron-electron interaction within a QCB constituent.

The following novel results were obtained in the course of this research:

- It is shown that the bosonization procedure may be applied to the Hamiltonian of $2D$

quantum networks. QCB plasmons may have either $1D$ or $2D$ character depending on the direction of the wave vector. The crossover from $1D$ to $2D$ regime may be experimentally observed. Indeed, due to inter-wire interaction, unperturbed states, propagating along the two arrays are always mixed, and transverse components of correlation functions do not vanish. For quasi-momenta near the resonant line of the BZ, such mixing is strong, and the transverse correlators possess specific dynamical properties. One of the main effects is the possibility of a periodic energy transfer between the two arrays of wires.

- The principles of spectroscopic studies of the excitation spectrum of quantum crossbars are established, which possesses unique property of dimensional crossover. The plasmon excitations in QCB may be involved in resonance diffraction of incident light and in optical absorption in the IR part of the spectrum. One can observe $1D \rightarrow 2D$ crossover behavior of QCB by scanning an incident angle. The crossover manifests itself in the appearance of a set of absorption doublets instead of the set of single lines. At special directions, one can observe new type of crossover where doublets replace the single lines with changing frequency at a fixed direction of a wave vector.
- It is shown that a capacitive contact between QCB and semiconductor substrate does not destroy the LL character of the long wave excitations. However, quite unexpectedly the interaction between the surface plasmons and plasmon-like excitations of QCB essentially influences the dielectric properties of a substrate. First, combined resonances manifest themselves in a complicated absorption spectra. Second, the QCB may be treated as the diffraction grid for a substrate surface, and an Umklapp diffraction processes radically change the plasmon dielectric losses. So the surface plasmons are more fragile against interaction with superlattice of quantum wires than the LL plasmons against interaction with $2D$ electron gas in a substrate.
- The principles of inelastic UV Raman spectroscopy of QCB are formulated. An effective Hamiltonian for QCB-light interaction is expressed via the same boson fields as the Hamiltonian of the QCB themselves. One can observe $1D \rightarrow 2D$ crossover of QCB by scanning an scattered angle. The crossover manifests itself in the appearance of multiplets (mostly doublets) instead of single lines.

Key Words

Quantum crossbars, Luttinger liquid, strongly correlated electrons, bosonization, plasmons, dimensional crossover, Rabi oscillations, *ac* conductivity, infrared absorption spectroscopy, dielectric function, Dyson equation, Landau damping, Raman spectroscopy.

Table of Contents

Table of Contents	1
1 Background and Objectives	7
2 From Quantum Wires to Quantum Crossbars	14
2.1 Introduction	14
2.2 Luttinger-Liquid Theory	14
2.3 Quasi One Dimensional Quantum Wire	16
2.4 Luttinger Liquid Behavior in Single-Wall Carbon Nanotubes (SWCNT) . . .	17
2.5 Sliding Luttinger Liquid Phase	23
2.6 Cross-Sliding Luttinger Liquid Phase	25
2.7 Quantum Crossbars with Virtual Wire-to-Wire Tunneling	27
3 Plasmon Excitations and One to Two Dimensional Crossover in Quantum Crossbars	29
3.1 Introduction	29
3.2 Basic Notions	30
3.3 Hamiltonian	33
3.4 Approximations	35
3.5 Spectrum	36
3.6 Correlations and Observables	40
3.6.1 Optical Absorption	40
3.6.2 Space Perturbation	41
3.6.3 Rabi Oscillations	42
3.7 Conclusions	43
4 Infrared Spectroscopy of Quantum Crossbars	44
4.1 Introduction	44
4.2 Long Wave Absorption	46
4.3 Scanning of the QCB Spectrum within the BZ	49
4.4 Conclusions	53
5 Landau Damping in a 2D Electron Gas with Imposed Quantum Grid	54
5.1 Introduction	54
5.2 Quantum Crossbars on Semiconductor Substrate	55
5.2.1 Substrate Characteristics	55
5.2.2 Interaction	57
5.3 Dielectric Function	57
5.4 Landau Damping	59

5.5	Conclusions	65
6	Ultraviolet Probing of Quantum Crossbars	66
6.1	Introduction	66
6.2	Light Scattering on QCB	66
6.3	Scattering Cross Section	69
6.3.1	Cross Section: Basic Types	69
6.3.2	Scattering Indicatrices	71
6.4	Conclusions	73
A	Empty Super-Chain	75
B	Spectrum and Correlators of Square QCB	77
B.1	Square QCB Spectrum	77
B.2	AC Conductivity	82
C	Tilted QCB	84
C.1	Geometry, Notions and Hamiltonian	84
C.2	Spectrum	85
D	Triple QCB	89
D.1	Notions and Hamiltonian	89
D.2	Spectrum	91
D.3	Observables	93
E	Derivation of QCB-Light Interaction Hamiltonian	96
	Bibliography	101

List of Figures

2.1	The low energy part of the free-electron spectrum. Here $p_0 = \pi/R_0$ and $E_0 = \hbar^2 p_0^2 / (2m_e)$. k is measured from p_F ($-p_F$) for right-moving (left-moving) fermions. Tilted lines describe the linear approximation $E_F \pm \hbar v_F k$ for right/left moving electrons.	17
2.2	(a) Honeycomb lattice of $2D$ carbon sheet and the coordinate system. Hexagonal sublattices A and B are labelled by \bullet and \circ , respectively. Two primitive translation vectors are \mathbf{a}_1 and \mathbf{a}_2 , where $ \mathbf{a}_1 = \mathbf{a}_2 = a_0 = 2.5 \text{ \AA}$ [49]. The vector directed from an A site to a nearest neighbor B site is \mathbf{d}_{AB} . A nanotube is specified by a chiral vector \mathbf{T} corresponding to the circumference of the nanotube whereas the x -axis is oriented along the nanotube axes. (b) First BZ of $2D$ carbon sheet. Here \circ and \bullet are two vertices of the BZ corresponding to the vectors \mathbf{K} and $-\mathbf{K}$ respectively, $ \mathbf{K} = 4\pi/(\sqrt{3}a_0)$. Wave vectors of low-energy quasi-particles lie at the axes k in the vicinity of the points $\pm\mathbf{K}$	19
2.3	The low-energy part of the band structure of a metallic nanotube in the vicinity of the vertices \mathbf{K} and \mathbf{K}' of the BZ (see Fig. 2.2). Lines 1, 2 (3, 4) correspond to excitations with orbital quantum number $m = 0$ ($m = \pm 1$). The bandwidth cutoff scale is $\omega_0 = v_F/R_0$. The Fermi level E_F (and momentum $q_F = E_F/v_F$) can be tuned by an external gate.	20
2.4	$2D$ crossbars formed by two interacting arrays of parallel quantum wires. Here $\mathbf{e}_1, \mathbf{e}_2$ are the unit vectors of the superlattice, $a_1 = a_2 \equiv a$ is the superlattice period (the case $a_1 \neq a_2$ is considered in Appendix C) and d is the vertical inter-array distance.	26
3.1	The Bragg lines in conventional $2D$ square lattice (a) and that of $2D$ square crossbars (b). In both panels, solid lines are the Bragg lines, whereas points correspond to reciprocal superlattice vectors.	31
3.2	Fermi surface of $2D$ metallic quantum bars in the absence of charge transfer between wires.	32

3.3	Two dimensional BZ of square QCB (left panel). The energy spectrum of QCB (solid lines) and noninteracting arrays (dashed lines) for quasimomenta at the lines $\Gamma\Gamma$, ΓX_1 , X_1W , and WT of BZ (right panel).	37
3.4	Lines of equal frequency of the lowest mode for QCB (solid lines) and for noninteracting arrays (dashed lines). The lines 1, 2, 3 correspond to the frequencies $\omega_1 = 0.1$, $\omega_2 = 0.25$, $\omega_3 = 0.4$	39
3.5	The transverse correlation function $G_{12}(x_1, x_2; t)$ for $r_0 = 1$ and $vt = 10$	41
3.6	Periodic energy exchange between arrays (Rabi oscillations).	42
4.1	The incident field orientation with respect to QCB. The axes x_1 and x_2 are directed along the corresponding arrays, and d is the inter-array vertical distance (along the x_3 axis).	46
4.2	QCB and DL. The X, Y axes are oriented along the DL stripes and the wave vector \mathbf{K} of the diffraction field respectively. The DL (QCB) period is A (a).	49
5.1	QCB on a substrate. \mathbf{e}_μ ($\mu = 1, 2, 3$) are basic vectors of the coordinate system. The vector \mathbf{e}_1 (\mathbf{e}_2) is oriented along the first (second) array. The inter-array distance is d and the distance between the substrate and the first (lower) array is D	55
5.2	Dispersion of the substrate plasmons (upper line) and quasi-continuum spectrum of electron-hole excitations, (dashed area). Frequency is measured in $\omega_0 = v_F/r_B$ units.	56
5.3	Phase diagram describing appearance and structure of new regions of Landau damping. Lines 1 – 6 separate different types of new damping regions. Points $a - f$ correspond to the structures displayed below in Figs. 5.4-5.6.	60
5.4	Left panel: New Landau damping region PUW for QCB with period $a = 20$ nm (point a in Fig. 5.3) corresponds to the Umklapp vector -1 . Right panel: New damping region $STUW$ for $a = 30$ nm (point b in Fig. 5.3) corresponds to the Umklapp vector -1 and describes Landau damping tail (within the arc TU) or separate Landau band (within the arc TP). Other details of this figure are explained in the text.	61
5.5	Left panel: In the case $a = 40$ nm (point c in Fig. 5.3), new Landau damping regions PVD , $STRUW$, and UHR correspond to the Umklapp vectors -2 , -1 , and $+1$. Right panel: New regions of Landau damping for $a = 50$ nm (point d in Fig. 5.3). Regions $ACVD$, STR , and FHR correspond to the Umklapp vectors -2 , -1 , and $+1$	62

5.6	Left panel: New regions of Landau damping for $a = 60$ nm (point e in Fig. 5.3). Besides the regions $ACVD$, STR , and FHR corresponding, as in the case $a = 50$ nm, to the Umklapp vectors -2 , -1 , and $+1$, new Umklapp vector -3 appears (region PEG). Right panel: The case $a = 70$ nm (point f in Fig. 5.3). New regions of Landau damping PEG , $ACVD$, STR , whole sector ΓPR , and VOR correspond to the Umklapp vectors -3 , -2 , -1 , $+1$, and $+2$.	63
5.7	Damping tail for $\varphi \approx 16^\circ$ (left panel) and $\varphi \approx 33^\circ$ (right panel). Precursor of the resonant peak and the resonant peak are resolved quite well.	63
5.8	Damping tail for $\varphi = 20^\circ$ for different distances D between QCB and substrate. The curves 1 , 2 , 3 , and 4 correspond to $D = 1$ nm, 1.5 nm, 2 nm, and 2.5 nm, respectively. With increasing D , the resonant peak narrows and slowly increases, whereas the area under the curve decreases.	65
6.1	(a) The scattering process geometry (all notations are explained in the text). (b) Second order diagram describing light scattering on QCB. Solid lines correspond to fermions, whereas dashed lines are related to photons. The vertices are described by the interaction Hamiltonian (6.1). (c) Effective photon-plasmon vertex. QCB excitation is denoted by wavy line.	67
6.2	Part of inverse space. The small square $k_j/Q \leq 0.5$ is the quarter of the first QCB BZ. High symmetry lines are parallel to the coordinate axes. Resonant lines are parallel to BZ diagonals. The arcs coming over the point B_1 , B_2 , B_3 , B_4 , B_5 , correspond to different wave numbers of excited plasmons: $ k/Q = 0.3; 0.5; 0.6; 0.7; 0.8$	70
6.3	Left panel: Positions of the scattering peaks for $ k/Q = 0.3$. The doublet in the resonance direction (point B_1 in Fig. 6.2) is well pronounced. Right panel: Positions of the scattering peaks for $ k/Q = 0.5$. Two doublets appear at the BZ boundaries (points C_1 and D_1 in Fig. 6.2).	72
6.4	Left panel: Positions of the scattering peaks for $ k/Q = 0.6$. Two doublets at the BZ boundaries (points C_2 and D_2) in Fig. 6.2) are shifted from the high symmetry directions. Right panel: Positions of the scattering peaks for $ k/Q = \sqrt{2}/2$. Resonance triplet corresponding to point B_4 in Fig. 6.2 (two of four frequencies remain degenerate in our approximation). In IR experiments only one of the triplet components is seen.	73
6.5	Positions of the scattering peaks for $ k/Q = 0.8$. Two pairs of doublets appear corresponding to excitation of two pairs of plasmons in the two arrays (points E and F in Fig. 6.2).	74
C.1	BZ of a tilted QCB.	86

C.2	The energy spectrum of a tilted QCB (solid lines) and noninteracting arrays (dashed lines) for quasimomenta (a) on the resonant line of the BZ (line ODE in Fig. C.1); (b) for quasimomenta at the BZ boundary (line FCF' in the Fig. C.1).	87
C.3	The energy spectrum of a titled QCB (solid lines) and noninteracting arrays (dashed lines) for quasimomenta on the BZ diagonal (line OC in Fig. C.1). .	87
C.4	Lines of equal frequency for a tilted QCB (solid lines) and noninteracting arrays (dashed lines). (a) Lines 1, 2, 3 correspond to frequencies $\omega_1 = 0.1$, $\omega_2 = 0.25$, $\omega_3 = 0.45$. (b) Lines 4, 5 correspond to frequencies $\omega_4 = 0.55$, $\omega_5 = 0.65$	88
D.1	Triple QCB (left panel). Elementary cell $BIJL$ of the reciprocal lattice and the BZ hexagon of the triple QCB (right panel).	90
D.2	Dispersion curves at the $OAMBO$ polygon of BZ.	93
D.3	Periodic energy transfer between three arrays at the triple resonant point C of the BZ.	95

Chapter 1

Background and Objectives

The behavior of electrons in arrays of one-dimensional ($1D$) quantum wires was recognized as a challenging problem soon after the consistent theory of elementary excitations and correlations in a Luttinger liquid (LL) of interacting electrons in one dimension was formulated (see [1] for a review). In contrast to the Fermi liquid (FL) theory [2, 3], one dimensional electron liquids exhibits the following properties:

- There is no elementary fermionic quasi-particles, the generic excitations are bosonic fluctuations.
- Charge and spin quasi-particles are spatially separated and move with different velocities (*charge-spin separation*).
- The correlations between these excitations show up as an interaction-dependent non-universal power law.

There are several possible regimes in which a $1D$ electron liquid can exist [4]. First, there is an insulating regime, where charge and spin excitations are gapped. Second, there is a conducting (Tomonaga-Luttinger) regime where the charge sector is gapless. In this case the spin sector is either gapped (Luther-Emery regime) or gapless.

One of the fascinating challenges is a search for LL features in higher dimensions [5]. Although the Fermi liquid state seems to be rather robust for $D > 1$, a possible way to retain some $1D$ excitation modes in $2D$ and even $3D$ systems is to consider highly anisotropic objects, in which the electron motion is spatially confined in the major part of real space (e.g., it is confined to separate linear regions by potential relief). One may hope that in this case, weak enough interaction does not violate the generic long-wave properties of the LL state.

Recent achievements in material science and technology have led to fabrication of an unprecedented variety of artificial structures that possess properties never encountered in "natural" quantum objects. One of the most exciting developments in this field is fabrication

of $2D$ networks by means of self-assembling, etching, lithography and imprinting techniques [6, 7]. Another development is the construction of $2D$ molecular electronic circuits [8] where the network is formed by chemically assembled molecular chains. Arrays of interacting quantum wires may be formed in organic materials and in striped phases of doped transition metal oxides. Artificially fabricated structures with controllable configurations of arrays and variable interactions are available now (see, e.g., Refs. [9, 10, 11]). Such networks have the geometry of crossbars, and bistable conformations of molecular chains may be used as logical elements [12]. Especially remarkable is a recent experimental proposal to fabricate $2D$ periodic grids from single-wall carbon nanotubes (SWCNT) suspended above a dielectric substrate [9]. The possibility of excitation of a SWCNT by external electric field together with its mechanical flexibility makes such a grid formed by nanotubes an excellent candidate for an element of random access memory for molecular computing.

From a theoretical point of view, such double $2D$ grid, i.e., two superimposed crossing arrays of parallel conducting quantum wires [13, 14, 15] or nanotubes [16], represents a unique nano-object - quantum crossbars (QCB). Its spectral properties cannot be treated in terms of purely $1D$ or $2D$ electron liquid theory. A constituent element of QCB (quantum wire or nanotube) possesses the Luttinger liquid (LL)-like spectrum [17, 18]. The inter-wire interaction may transform the LL state existing in isolated quantum wires into various phases of $2D$ quantum liquid. The most drastic transformation is caused by *inter-wire* tunneling in arrays of quantum wires with *intra-wire* Coulomb repulsion. The tunneling constant rescales towards higher values for strong intra-wire interaction, and the electrons in an array transform into $2D$ Fermi liquid [19, 20]. The reason for this instability is the orthogonality catastrophe, i.e., the infrared divergence in the low-energy excitation spectrum that accompanies the inter-wire hopping processes.

Unlike inter-wire tunneling, density-density or current-current inter-wire interaction does not modify the low-energy behavior of quantum arrays under certain conditions. In particular, it was shown recently [21, 22, 23, 16] that “vertical” interaction which depends only on the distance between the wires, imparts the properties of a *sliding phase* to $2D$ array of $1D$ quantum wires. Such LL structure can be interpreted as a quantum analog of classical sliding phases of coupled XY chains [24]. Recently, it was found [25, 26] that a hierarchy of quantum Hall states emerges in sliding phases when a quantizing magnetic field is applied to an array.

Similar low-energy, long-wave properties are characteristic of QCB as well. Its phase diagram inherits some properties of sliding phases in case when the wires and arrays are coupled only by capacitive interaction [16]. When the inter-array electron tunneling is possible, say, in crosses, dimensional crossover from LL to $2D$ FL occurs [27, 16]. If tunneling is suppressed and the two arrays are coupled only by electrostatic interaction in the crosses, the system possesses the LL zero energy fixed point [23].

The physics of dimensional crossover is quite well studied, e.g., in thin semiconductor or superconductor films where the film thickness serves as a control parameter that governs the crossover (see e.g. Ref. [28, 29]). It occurs in strongly anisotropic systems like quasi-one-dimensional organic conductors [30] or layered metals [31, 32, 33, 34, 35]. In the latter cases, temperature serves as a control parameter and crossover manifests itself in inter-layer transport. In metals, the layers appear “isolated” at high temperature, but become connected at low temperatures to manifest $3D$ conducting properties.

The most promising type of artificial structures where dimensional crossover is expected is a periodic $2D$ system of m crossing arrays of parallel quantum wires or carbon nanotubes. We call it “quantum crossbars” (QCB). Square grids of this type consisting of two arrays were considered in various physical contexts in Refs. [13, 14, 15, 27]. In Refs. [15, 27] the fragility of the LL state against inter-wire tunnelling in the crossing areas of QCB was studied. It was found that a new periodicity imposed by the inter-wire hopping term results in the appearance of a low-energy cutoff $\Delta_l \sim \hbar v/a$ where v is the Fermi velocity and a is the period of the quantum grid. Below this energy, the system is “frozen” in its lowest one-electron state. As a result, the LL state remains robust against orthogonality catastrophe, and the Fermi surface conserves its $1D$ character in the corresponding parts of the $2D$ Brillouin zone (BZ). This cutoff energy tends to zero at the points where the one-electron energies for two perpendicular arrays ϵ_{k_1} and ϵ_{k_2} become degenerate. As a result, a dimensional crossover from $1D$ to $2D$ Fermi surface (or from LL to FL behavior) arises around the points $\epsilon_{F_1} = \epsilon_{F_2}$.

Unlike inter-wire tunneling, the density-density or current-current inter-wire interaction does not modify the low-energy behavior of quantum arrays under certain conditions. In particular, it was shown recently [21, 22, 23] that “vertical” interaction which depends only on the distance between the wires, imparts the properties of a *sliding Luttinger liquid phase* to $2D$ array of $1D$ quantum wires. Such LL structure can be interpreted as a quantum analog of classical sliding phases of coupled XY chains [24]. Recently, it was found [25] that a hierarchy of quantum Hall states emerges in sliding phases when a quantizing magnetic field is applied to an array. Similar low-energy, long-wave properties are characteristic of QCB as well. Its phase diagram inherits some properties of sliding phases in case when the wires and arrays are coupled only by capacitive interaction [16]. If tunneling is suppressed and the two arrays are coupled only by electrostatic interaction in the crosses, the system possesses a *cross-sliding Luttinger liquid* (CSLL) zero energy fixed point.

In this Thesis we develop a theory of interacting Bose excitations (plasmons) in a superlattice formed by crossed interacting arrays of quantum wires. This theory goes far beyond the problem of stability of the CSLL fixed point. We do not confine ourselves with the studying the conditions under which the LL behavior is preserved in spite of inter-wire interaction. We consider situations where the *dimensional crossover* from $1D$ to $2D$ occurs. It turns out that the standard bosonization procedure is valid in a $2D$ reciprocal space under

certain conditions. The QCB behaves as a sliding Luttinger liquid in the infrared limit, and exhibits a rich Bose-type excitation spectrum (plasmon modes) arising at finite energies in $2D$ BZ. We derive the Hamiltonian of the QCB, analyze the spectrum of boson fields away from the LL fixed point and compute two-point correlation functions in QCB with short range inter-array capacitive interaction. We study new type of dimensional crossover, i.e., a *geometrical* crossover where the quasimomentum serves as a control parameter, and the excitations in a system of quantum arrays demonstrate either $1D$ or $2D$ behavior in different parts of reciprocal space. A rather pronounced manifestation of this kind of dimensional crossover is related to the QCB response to an external ac electromagnetic field. We formulate the principles of spectroscopy for the QCB. We consider an infrared (IR) absorption spectroscopy of the QCB and an ultraviolet (UV) scattering on the QCB, and study the main characteristics of IR absorption spectra and UV scattering observables.

The structure of the Thesis is as follows. In the second Chapter the progress in the theory of interacting fermions in low-dimensional systems (such as quantum wires, metallic carbon nanotubes, array of quantum wires, and QCB) exhibiting LL-like behavior is briefly reviewed. The bosonization procedure is introduced for a simple model of $1D$ spinless interacting electrons. The LL theory is applied for describing the low-energy behavior of interacting electrons in real systems such as quasi one-dimensional quantum wires and single-wall carbon nanotubes. The existence of sliding LL phase is established for an array of weakly coupled parallel quantum wires. This analysis is extended to a system of two crossed arrays of $1D$ quantum wires (QCB) with a capacitive inter-wire coupling. Such a system exhibits a crossed-sliding LL phase. We also consider QCB with virtual wire-to-wire electron tunneling, and find the necessary condition under which the one-electron tunneling is suppressed and the cross-sliding LL phase is stable.

In the third Chapter the spectrum of boson fields and two-point correlation functions are analyzed in a double square QCB. We show that the standard bosonization procedure is valid, and that the system behaves as a sliding Luttinger liquid in the infrared limit, but the high frequency spectral and correlation characteristics have either $1D$ or $2D$ nature depending on the direction of the wave vector in the $2D$ elementary cell of the reciprocal lattice. As a result, the crossover from $1D$ to $2D$ regime may be experimentally observed. It manifests itself as appearance of additional peaks of optical absorption, non-zero transverse space correlators and periodic energy transfer between arrays (“Rabi oscillations”).

In the fourth Chapter the effectiveness of infrared spectroscopy is studied. It is shown that plasmon excitations in the QCB may be involved in resonance diffraction of incident electromagnetic waves and in optical absorption in the IR part of the spectrum. The plasmon velocity is much smaller than the light velocity. Therefore, an infrared radiation incident on an *isolated* array, cannot excite plasmons at all. However in QCB geometry, each array serves as a diffraction lattice for its partner, giving rise to Umklapp processes of reciprocal

super-lattices vectors. As a result, plasmons may be excited in the BZ center. To excite QCB plasmons with non-zero wave vectors, an additional diffraction lattice (DL) coplanar with the QCB can be used. Here the diffraction field contains space harmonics with wave vectors perpendicular to the DL that enable one to eliminate the wave vector mismatch and to scan plasmon spectrum within the BZ. In the general case, one can observe single absorption lines forming two equidistant series. However, in case where the wave vector of the diffraction field is oriented along some resonance directions, additional absorption lines appear. As a result, an equidistant series of split doublets can be observed in the main resonance direction (BZ diagonal). This is the central concept of dimensional crossover mentioned above with direction serving as a control parameter. In higher resonance directions, absorption lines form an alternating series of singlets and split doublets demonstrating new type of dimensional crossover. The latter occurs in a given direction with a frequency as a control parameter.

The fifth Chapter is devoted to the study of dielectric properties of a semiconductor substrate with the imposed $2D$ QCB. We demonstrate that a capacitive contact between the QCB and semiconductor substrate does not destroy the Luttinger liquid character of the long wave QCB excitations. However, dielectric losses of a substrate surface are drastically modified due to diffraction processes on the QCB superlattice. QCB-substrate interaction results in additional Landau damping regions of the substrate plasmons. Their existence, form and the density of dielectric losses are strongly sensitive to the QCB lattice constant and the direction of the wave vector of the substrate plasmon. Thus, dielectric losses in the QCB-substrate system serve as a good tool for studying QCB spectral properties.

In the sixth Chapter, the principles of UV spectroscopy for QCB are formulated and the main characteristics of scattering spectra are described. We study inelastic scattering of an incident photon leading to the creation of a QCB plasmon. Experimentally, such a process corresponds to sharp peaks in the frequency dependence of the differential scattering cross section. We show that the peak frequency strongly depends on the direction of the scattered light. As a result, the $1D \rightarrow 2D$ crossover can be observed in the scattering spectrum. It manifests itself as a splitting of single lines into multiplets (mostly doublets).

All technical details are contained in Appendices A, B, and E. Double tilted and triple QCB are considered in Appendices C and D, respectively.

This work was partially presented by posters and lectures in scientific conferences and schools (see List of Presentations). The first part of the results was published in Refs. 1-4 (see List of Publications). The second and third parts were published in Refs. 5-8. The fourth part was published in Refs. 9, 10.

The author is grateful to V. Liubin, M. Klebanov, and Y. Imry for discussions of the effectiveness of the infrared absorption and ultraviolet scattering in probing spectral properties of QCB.

List of Presentations

1. I. Kuzmenko. *Ultraviolet Scattering on Quantum Crossbars* (poster). Third Windsor School on Condensed Matter Theory “Field Theory on Quantum Coherence, Correlations and Mesoscopics”, Windsor, UK, August 9-22, 2004.
2. I. Kuzmenko, S. Gredeskul, K. Kikoin, Y. Avishai. *Optical Properties of Quantum Crossbars* (poster). SCES’04, the International Conference, on Strongly Correlated Electron Systems, Karlsruhe, Germany, July 26-30, 2004.
3. I. Kuzmenko. *Spectrum and Optical Properties of Quantum Crossbars* (lecture). Condensed Matter Seminar, Department of Physics, Ben-Gurion University of the Negev, Beer Sheva, Israel, June 7, 2004.
4. I. Kuzmenko, S. Gredeskul, K. Kikoin, Y. Avishai. *Dielectric Properties of Quantum Crossbars* (lecture). International School and Workshop on Nanotubes & Nanostructures, Frascati, Italy, September 15-19, 2003.
5. I. Kuzmenko, S. Gredeskul, K. Kikoin, Y. Avishai. *Optical Absorption and Dimensional Crossover in Quantum Crossbars* (poster). International Seminar and Workshop on Quantum transport and Correlations in Mesoscopic Systems and Quantum Hall Effect, Dresden, Germany, July 28 - August 22, 2003.
6. I. Kuzmenko, S. Gredeskul, K. Kikoin, Y. Avishai. *Electronic Excitations in 2D Crossbars* (poster). International School of Physics ”Enrico Fermi”, Varenna, July 9-19, 2002.
7. I. Kuzmenko, S. Gredeskul, K. Kikoin, Y. Avishai. *Electronic Properties of Quantum Wire Networks* (poster). 19th Winter School for Theoretical Physics, Jerusalem, December 30, 2001 - January 8, 2002.
8. I. Kuzmenko, S. Gredeskul, K. Kikoin, Y. Avishai. *Electronic Properties of Quantum Bars* (poster). Meeting of Israel Physical Society, Tel-Aviv, December 17, 2001.
9. I. Kuzmenko, S. Gredeskul, K. Kikoin, Y. Avishai. *Energy Spectrum of Quantum Bars* (poster). NATO ASI at Windsor, UK, August 13-26, 2001.

List of Publications

1. I. Kuzmenko, S. Gredeskul, K. Kikoin, Y. Avishai. *Electronic Excitations and Correlations in Quantum Bars*. Low Temperature Physics, **28**, 539 (2002); [Fizika Nizkikh Temperatur, **28**, 752 (2002)].
2. K. Kikoin, I. Kuzmenko, S. Gredeskul, Y. Avishai. *Dimensional Crossover in 2D Crossbars*. Proceedings of NATO Advanced Research Workshop “Recent Trends in Theory of Physical Phenomena in High Magnetic Fields” (Les Houches, France, February 25 - March 1, 2002), p. 89; cond-mat/0205120.
3. I. Kuzmenko, S. Gredeskul, K. Kikoin, Y. Avishai. *Plasmon Excitations and One to Two Dimensional Crossover in Quantum Crossbars*. Phys. Rev. B **67**, 115331 (2003); cond-mat/0208211.
4. S. Gredeskul, I. Kuzmenko, K. Kikoin, Y. Avishai. *Spectrum, Correlations and Dimensional Crossover in Triple 2D Quantum Crossbars*. Physica E **17**, 187 (2003).
5. S. Gredeskul, I. Kuzmenko, K. Kikoin, and Y. Avishai. *Quantum Crossbars: Spectra and Spectroscopy*. Proceeding of NATO Conference MQO, Bled, Slovenia, September 7-10, 2003, p.219.
6. I. Kuzmenko, S. Gredeskul. *Infrared Absorption in Quantum Crossbars*. HAIT. Journal of Science and Engineering **1**, 130 (2004).
7. I. Kuzmenko, S. Gredeskul, K. Kikoin, and Y. Avishai, *Infrared Spectroscopy of Quantum Crossbars*. Phys. Rev. B **69**, 165402 (2004); cond-mat 0306409.
8. I. Kuzmenko. *Landau Damping in a 2D Electron Gas with Imposed Quantum Grid*. Nanotechnology **15**, 441 (2004); cond-mat 0309546.
9. I. Kuzmenko. *X-ray Scattering on Quantum Crossbars*. Physica B **359-361**, 1421 (2005).
10. I. Kuzmenko, S. Gredeskul, K. Kikoin, and Y. Avishai, *Ultraviolet Probing of Quantum Crossbars*. Phys. Rev. B **71**, 045421 (2005); cond-mat 0411184.

Chapter 2

From Quantum Wires to Quantum Crossbars

2.1 Introduction

In this Chapter, a brief review of electron properties of low-dimensional systems is presented. In Section 2.2, Luttinger-liquid (LL) theory is introduced. In Sections 2.3 and 2.4, the LL theory is applied to describe low-energy properties of an electron liquid in a quasi one dimensional quantum wire and a carbon nanotube. In Section 2.5, an array of quantum wires or carbon nanotubes with local density-density and/or current-current inter-wire interactions is considered which result in generalized Luttinger-liquid theory. Similar Luttinger-liquid behavior of electron liquid in crossed arrays is considered in Sections 2.6 and 2.7.

2.2 Luttinger-Liquid Theory

Following conventional Luttinger liquid (LL) theory [36, 37, 38, 39], we consider in this Section a simple model: a $1D$ conductor containing spinless right- and left-moving electrons (spin sector is assumed to be gapped). In the Tomonaga-Luttinger model, the free-electron dispersion is assumed to be linear $\varepsilon_{Lk} = \pm\hbar v_F k$ around two Fermi points $\pm k_F$, and a local electron-electron interaction is parameterized by the dimensionless coupling constants g_2 and g_4 . The model Hamiltonian $H_{TL} = H_{\text{kin}} + H_{\text{int}}$ is

$$H_{\text{kin}} = i\hbar v_F \int_{-L/2}^{L/2} dx \left(\psi_L^\dagger(x) \partial_x \psi_L(x) - \psi_R^\dagger(x) \partial_x \psi_R(x) \right), \quad (2.1)$$

$$H_{\text{int}} = \pi\hbar v_F \int_{-L/2}^{L/2} dx \left[g_4 (\rho_L^2(x) + \rho_R^2(x)) + 2g_2 \rho_L(x) \rho_R(x) \right]. \quad (2.2)$$

Here $\psi_L(x)$ ($\psi_R(x)$) is the field operator for left-moving (right-moving) fermions satisfying the anti-commutation relations $\{\psi_\alpha(x), \psi_{\alpha'}^\dagger(x')\} = \delta_{\alpha\alpha'}\delta(x-x')$ ($\alpha, \alpha' = L, R$); $\rho_\alpha(x) = \psi_\alpha^\dagger(x)\psi_\alpha(x)$ are the density operators for left- and right-movers. The total number of left (right) moving electrons is a good quantum number. Therefore all excitations are electron-hole-like and hence have bosonic character.

It is convenient to write the Hamiltonian in terms of bosonic fields. The electron density $\rho_{L/R}(x)$ can be expressed in terms of derivative fields $\partial_x\varphi_{L/R}(x)$:

$$:\rho_L(x) := \frac{1}{2\pi}\partial_x\varphi_L(x), \quad :\rho_R(x) := -\frac{1}{2\pi}\partial_x\varphi_R(x). \quad (2.3)$$

Here $:\rho_{L/R} := \rho_{L,R} - \langle 0|\rho_{L,R}|0\rangle$ denotes the fermion-normal-ordering with respect to the Fermi sea $|0\rangle$ defined as following [38], to normal-order a function of operators of creation and annihilation of fermions, operators of creation of fermions above the Fermi level and operators of annihilation of fermions below the Fermi level are to be moved to the left of all other operators (namely operators of creation of fermions below the Fermi level and operators of annihilation of fermions above Fermi level). The fields $\varphi_{L,R}(x)$ satisfy the following commutation relations [38]

$$[\varphi_{L/R}(x), \varphi_{L/R}(x')] = \mp i\pi\text{sign}(x-x'), \quad [\varphi_L(x), \varphi_R(x')] = 0. \quad (2.4)$$

It is convenient to define

$$\theta(x) = \frac{1}{\sqrt{4\pi}}[\varphi_L(x) - \varphi_R(x)], \quad \phi(x) = \frac{1}{\sqrt{4\pi}}[\varphi_L(x) + \varphi_R(x)], \quad (2.5)$$

where $\theta(x)$ is a density variable and $\phi(x)$ is the conjugate phase variable [39]. Then one obtains

$$H_{TL} = \frac{\hbar v}{2} \int_{-L/2}^{L/2} dx \left(\frac{1}{g}\pi^2(x) + g(\partial_x\theta(x))^2 \right). \quad (2.6)$$

The Hamiltonian (2.6) describes a set of harmonic oscillators, where $\theta(x)$ and $\pi(x) = \partial_x\phi(x)$ satisfy the commutation relations of conventional canonically conjugate operators of a ‘‘coordinate’’ and a ‘‘momentum’’: $[\theta(x), \pi(x')] = i\delta(x-x')$. The renormalized Fermi velocity v and the LL parameter g are given by the equations

$$v = v_F\sqrt{(1+g_4)^2 - g_2^2}, \quad g = \sqrt{\frac{1+g_4-g_2}{1+g_4+g_2}}. \quad (2.7)$$

The dimensionless parameter g is a measure of the strength of the electron-electron interactions. It plays a central role in the LL theory. The noninteracting value of g (i.e., for $g_2 = 0$) is 1, and for repulsive interactions ($g_2 > 0$) g is less than 1.

2.3 Quasi One Dimensional Quantum Wire

In this Section, the LL theory is applied to a conductor slab of length L , width R_0 and thickness r_0 ($L \gg R_0 \gg r_0$) containing free spinless electrons (spin sector is still assumed to be gapped). In experimentally realizable setups, such a structure can be created by cleverly gating 2D electron gas in GaAs inversion layers [40, 41, 42, 43], and doped helical polyacetylene nanofibres [44]. The position of an electron is described by a 2D vector $\mathbf{r} = (x, y)$, where the x -axis is taken along the wire direction ($0 < x < L$), and y is taken along transverse direction ($0 < y < R_0$). The 2D momentum of an electron is $\mathbf{p} = (p, \kappa)$ and its dispersion is $E(\mathbf{p}) = \hbar^2 \mathbf{p}^2 / (2m_e)$ (see Fig. 2.1). Here p (κ) is the wave number in the direction of the wire axes (in the transverse direction), m_e is an effective electron mass. Up to scales $|p| < p_0 = \pi/R_0$ and $E < E_0 = \hbar^2 p_0^2 / (2m_e)$, all the excitations are one dimensional. In the subsequent discussion we assume that $p_F < p_0$ and $E_F < E_0$. Then we have “left”- and “right”-moving quasi-particles with energies near the Fermi level and momenta near p_F ($-p_F$) for right-moving (left-moving) fermions. We introduce the momentum index $k = p - p_F$ ($k = p + p_F$) for right-moving (left-moving) fermions. It is seen that $-p_F < k < \infty$ ($-\infty < k < p_F$) for right-moving (left-moving) fermions.

Following Ref. [38], we extend the range of k to be unbounded by introducing additional unphysical “positron states” at the bottom of the Fermi sea. Next, we factor out the rapidly fluctuating $e^{\pm ip_F x}$ phase factors and express the physical fermion field $\Psi(x)$ in terms of two fields $\psi_{L/R}(x)$ that vary slowly on the scale of $1/p_F$:

$$\Psi(x) = e^{ip_F x} \psi_R(x) + e^{-ip_F x} \psi_L(x). \quad (2.8)$$

The energies near the Fermi level can be written as $E_k = E_F + \hbar v_F k$ ($E_k = E_F - \hbar v_F k$) for right-moving (left-moving) fermions, where $v_F = \hbar p_F / m_e$ is Fermi velocity. Then in this approximation the kinetic energy Hamiltonian has the form of the Hamiltonian (2.1).

Electron-electron interaction is a Coulomb interaction screened in the long-wave limit [45]. Indeed, quantum wires are not pure 1D objects and screening arise due to their finite transverse size R_0 which is the characteristic screening length [46]. It is described by the following Hamiltonian

$$H_{\text{int}} = \frac{1}{2} \int \frac{dx dy}{R_0} \int \frac{dx' dy'}{R_0} U(\mathbf{r} - \mathbf{r}') \rho(x, y) \rho(x', y'). \quad (2.9)$$

Here

$$U(\mathbf{r}) = \frac{e^2 \zeta\left(\frac{x}{R_0}\right)}{\sqrt{|\mathbf{r}|^2 + r_0^2}}, \quad (2.10)$$

where r_0 is the stripe thickness, the screening function $\zeta(\xi)$ (introduced phenomenologically) is of order unity for $|\xi| < 1$ and vanishes for $|\xi| > 1$. In the long-wavelength limit, the electron

density operator $\rho(x, y) \equiv \rho(x) = \Psi^\dagger(x)\Psi(x)$ can be written as

$$\rho(x) = \rho_L(x) + \rho_R(x) + \psi_L^\dagger(x)\psi_R(x)e^{2ip_Fx} + \psi_R^\dagger(x)\psi_L(x)e^{-2ip_Fx}, \quad (2.11)$$

where $\rho_\alpha(x) = \psi_\alpha^\dagger(x)\psi_\alpha(x)$ ($\alpha = L, R$) are density operators for left- and right-moving fermions.

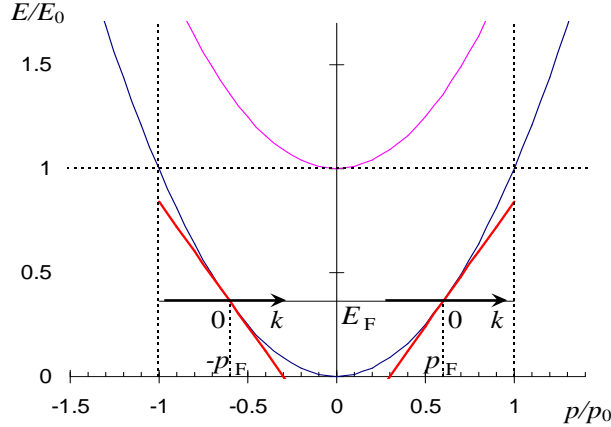


Figure 2.1: The low energy part of the free-electron spectrum. Here $p_0 = \pi/R_0$ and $E_0 = \hbar^2 p_0^2 / (2m_e)$. k is measured from p_F ($-p_F$) for right-moving (left-moving) fermions. Tilted lines describe the linear approximation $E_F \pm \hbar v_F k$ for right/left moving electrons.

Then one can write the interaction (2.9) in the form (2.2), where

$$g_4 = \frac{1}{\pi} \int \frac{dx dy}{R_0} \frac{U(\mathbf{r})}{\hbar v_F} \approx \frac{2e^2}{\hbar v_F}, \quad g_2 = \frac{1}{\pi} \int \frac{dx dy}{R_0} \frac{U(\mathbf{r})}{\hbar v_F} (1 - \cos(2p_F x)) \approx \frac{2e^2}{3\hbar v_F} (p_F R_0)^2.$$

With Eqs. (2.3) and (2.5), the Hamiltonian $H = H_{\text{kin}} + H_{\text{int}}$ acquires the form (2.6), where renormalized Fermi velocity v and the dimensionless interaction parameter g are given by Eqs. (2.7). In the GaAs slab with a density of one electron per 10 nm and the width $R_0 \sim 1$ nm, $m_e = 0.068m_0$ (m_0 is the free electron mass), $v_F \sim 10^7$ cm/sec and then $g \sim 0.97$.

2.4 Luttinger Liquid Behavior in Single-Wall Carbon Nanotubes (SWCNT)

Nanotubes are tubular nanoscale objects which can be thought as a graphite sheet wrapped into a cylinder [47, 48]. The arrangement of carbon atoms on the tube surface is determined by the integer indices $0 \leq m \leq n$ of the wrapping superlattice vector $\mathbf{T} = n\mathbf{a}_1 + m\mathbf{a}_2$ [49, 50], where \mathbf{a}_1 and \mathbf{a}_2 are the primitive Bravais translation vectors of the honeycomb lattice (see Fig. 2.2). The first Brillouin zone of the honeycomb lattice is a hexagon, and there are two independent Fermi points denoted by \mathbf{K} and $-\mathbf{K}$, with two linearly dispersing bands around each of these points. The necessary condition of metallicity of SWCNT is $2n + m = 3I$

for an integer I [49]. If this condition is not fulfilled, the nanotube exhibits the band gap $\Delta E \sim 2\hbar v_F/(3R_0) \sim 1$ eV [49, 51], where v_F is the Fermi velocity and R_0 is the nanotube radius. Even if the necessary condition is fulfilled, the rearrangement of local bonds due to the curvature of the cylinder can introduce a gap, $\Delta E \sim 10$ meV, which implies narrow-gap semiconducting behavior. For very small tube diameter (1 nm or less), due to the strong curvature-induced hybridization of σ and π orbitals, this effect can be quite pronounced [52]. In the cases of “*armchair*” ($n = m$) and “*zigzag*” ($m = 0$) nanotubes, however, the formation of a secondary gap is prevented by the high symmetry, and therefore armchair and zigzag nanotubes are metallic [53].

In this Section, a single metallic SWCNT is under consideration. The effective low-energy description of SWCNT is derived. Coulomb interaction between electrons induce a breakdown of Fermi liquid theory. It is shown that the bosonization procedure (similar to the procedure derived in Section 2.1) is valid. As a result, interacting electrons in a metallic SWCNT exhibit Luttinger liquid behavior.

The electronic properties of carbon nanotubes are due to special band-structure of the π -electrons in graphite [54]. The band structure exhibits two Fermi points $\kappa\mathbf{K}$ ($\kappa = \pm$) with a right- and left-moving ($\alpha = R/L$) branch around each Fermi point. These branches are highly linear with Fermi velocity $v_F \approx 8 \times 10^7$ cm/s. The R- and L-movers arise as linear combinations of the $\tau = A, B$ sublattice states reflecting the two C atoms in the basis of the honeycomb lattice. The dispersion relation is linear for energy scale $E < D$, with the bandwidth cutoff scale $D \approx \hbar v_F/R_0$ for tube radius R_0 . For typical SWCNT, D is of the order 1 eV. The large overall energy scale together with the structural stability of SWCNTs explain their unique potential for revealing Luttinger liquid (LL) physics. The fermionic quasi-particles in the vicinity of the Fermi level of graphite are described by the $2D$ massless Dirac Hamiltonian [49]. This result can also be derived in terms of $\mathbf{k} \cdot \mathbf{p}$ theory [50].

Wrapping the graphite sheet onto a cylinder then leads to the generic band-structure of a metallic SWCNT shown in Fig. 2.3. Quantization of transverse (azimuthal) motion now allows for a contribution $\propto \exp(imy/R_0)$ to the wave function. Here the x -axis is taken along the tube direction, the circumferential variable is $0 < y < 2\pi R_0$ (y is really the azimuthal angle multiplied by the nanotube radius R_0). However, excitation of angular momentum states other than $m = 0$ costs a huge energy of order $D \approx 1$ eV. In an effective low-energy theory, we may thus omit all transport bands except $m = 0$ (assuming that the SWCNT is not excessively doped). Evidently, the nanotube forms a $1D$ quantum wire with only two transport bands intersecting the Fermi energy. This strict one-dimensionality is fulfilled up to a remarkably high energy scales (eV) here, in contrast to conventional $1D$ conductors. The Hamiltonian of kinetic energy is:

$$H_{\text{kin}} = -i\hbar v_F \sum_{\kappa\sigma} \int dx \left(\psi_{A\kappa\sigma}^\dagger(x) \partial_x \psi_{B\kappa\sigma}(x) + \psi_{B\kappa\sigma}^\dagger(x) \partial_x \psi_{A\kappa\sigma}(x) \right), \quad (2.12)$$

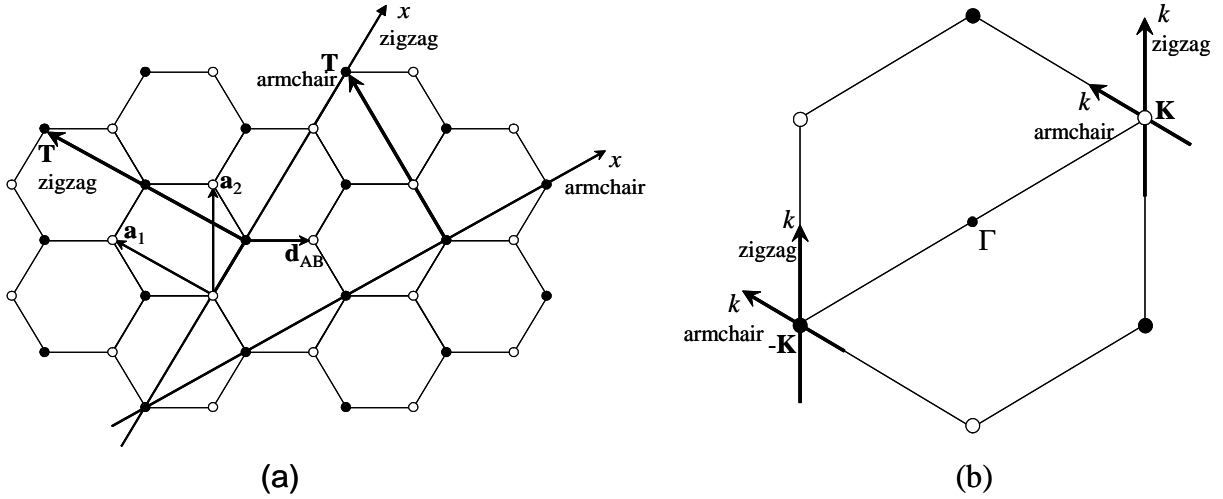


Figure 2.2: **(a)** Honeycomb lattice of 2D carbon sheet and the coordinate system. Hexagonal sublattices A and B are labelled by \bullet and \circ , respectively. Two primitive translation vectors are \mathbf{a}_1 and \mathbf{a}_2 , where $|\mathbf{a}_1| = |\mathbf{a}_2| = a_0 = 2.5 \text{ \AA}$ [49]. The vector directed from an A site to a nearest neighbor B site is \mathbf{d}_{AB} . A nanotube is specified by a chiral vector \mathbf{T} corresponding to the circumference of the nanotube whereas the x -axes is oriented along the nanotube axes. **(b)** First BZ of 2D carbon sheet. Here \circ and \bullet are two vertices of the BZ corresponding to the vectors \mathbf{K} and $-\mathbf{K}$ respectively, $|\mathbf{K}| = 4\pi/(\sqrt{3}a_0)$. Wave vectors of low-energy quasi-particles lie at the axes k in the vicinity of the points $\pm\mathbf{K}$.

where $\psi_{\tau\kappa\sigma}(x)$ is the “smooth” field operator of fermions in the sublattice $\tau = A, B$ in the vicinity of the Fermi point $\kappa\mathbf{K}$ ($\kappa = \pm$) with spin $\sigma = \uparrow, \downarrow$ [51]. Switching from the sublattice ($\tau = A, B$) description to the right- and left-movers ($\alpha = R, L$),

$$\psi_{R/L\kappa\sigma}(x) = \frac{1}{\sqrt{2}} (\psi_{A\kappa\sigma}(x) \mp \psi_{B\kappa\sigma}(x)),$$

implies two copies ($\kappa = \pm$) of massless 1D Dirac Hamiltonians (similar to the Hamiltonian (2.1)) for each spin direction,

$$H_{\text{kin}} = i\hbar v_F \sum_{\kappa\sigma} \int dx \left(\psi_{L\kappa\sigma}^\dagger(x) \partial_x \psi_{L\kappa\sigma}(x) - \psi_{R\kappa\sigma}^\dagger(x) \partial_x \psi_{R\kappa\sigma}(x) \right).$$

The electron-electron interaction is the screened Coulomb interaction between charge fluctuations [46]. The re-distribution of a charge induced by “external” charge can be described by the envelope function (introduced phenomenologically) $\zeta(\xi)$, $\xi = x/R_0$, $\zeta(\xi) = \zeta(-\xi)$, $\zeta(0) \sim 1$. This function is of order of unity for $|\xi| \sim 1$ and vanishes outside this region. Thus similarly to Eq. (2.10), the interaction is introduced as

$$U(\mathbf{r}) = \frac{e^2 \zeta\left(\frac{x}{R_0}\right)}{\left[x^2 + 4R_0^2 \sin^2\left(\frac{y}{2R_0}\right) + r_B^2 \right]^{1/2}}, \quad (2.13)$$

where r_B denotes the average distance between a $2p_z$ electron and the nucleus, i.e., the “thickness” of the graphite sheet. In the long-wavelength limit, electron-electron interactions

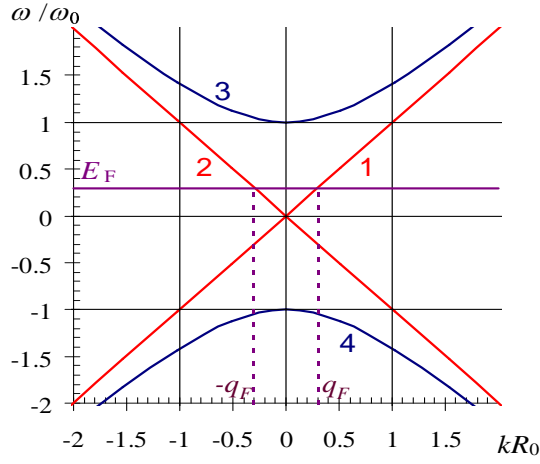


Figure 2.3: The low-energy part of the band structure of a metallic nanotube in the vicinity of the vertices \mathbf{K} and \mathbf{K}' of the BZ (see Fig. 2.2). Lines 1, 2 (3, 4) correspond to excitations with orbital quantum number $m = 0$ ($m = \pm 1$). The bandwidth cutoff scale is $\omega_0 = v_F/R_0$. The Fermi level E_F (and momentum $q_F = E_F/v_F$) can be tuned by an external gate.

are then described by the second-quantized Hamiltonian [51]

$$H_I = \frac{1}{2} \sum_{\tau\tau'\sigma\sigma'} \sum_{\{\kappa_i\}} \int dx dx' V_{\{\kappa_i\}}^{\tau\tau'}(x-x') \psi_{\tau\kappa_1\sigma}^\dagger(x) \psi_{\tau'\kappa_2\sigma'}^\dagger(x') \psi_{\tau'\kappa_3\sigma'}(x') \psi_{\tau\kappa_4\sigma}(x), \quad (2.14)$$

with the 1D interaction potentials

$$V_{\{\kappa_i\}}^{\tau\tau'}(x-x') = \int \frac{dy dy'}{(2\pi R_0)^2} e^{i\mathbf{K}((\kappa_1-\kappa_4)\mathbf{r}+(\kappa_2-\kappa_3)\mathbf{r}')} U(\mathbf{r}-\mathbf{r}'+\mathbf{d}_{pp'}). \quad (2.15)$$

These potentials depend only on $x-x'$ and on the 1D fermion quantum numbers. For interactions involving different sublattices $\tau \neq \tau'$ for \mathbf{r} and \mathbf{r}' in Eq. (2.15), one needs to take into account the shift vector $\mathbf{d}_{pp'}$ ($\mathbf{d}_{AB} = -\mathbf{d}_{BA}$, $|\mathbf{d}_{AB}| = 1.44 \text{ \AA}$ [49]) between sublattices (see Fig. 2.2).

To simplify the resulting 1D interaction (2.14), we now exploit momentum conservation, assuming $E_F \neq 0$ (see Fig. 2.3) so that Umklapp electron-electron scattering can be ignored, and only the processes conserving the number of electrons for each channel $\tau\kappa$ will be considered, i.e., $\kappa_1 + \kappa_2 = \kappa_3 + \kappa_4$. We then have “forward scattering” processes and “exchange interaction”, where $\kappa_1 = \kappa_4$ and $\kappa_2 = \kappa_3$. In addition, “backscattering” processes may be important, where $\kappa_1 = -\kappa_2 = \kappa_3 = -\kappa_4$.

In the next step, we employ the fact that the potentials $V_{\{\kappa_i\}}(x-x')$ are screened with the radius of screening being of order of the nanotube radius R_0 , whereas the field operators ψ 's are slowly varying on this distance scale. As a result, one can approximate the short-range potentials $V_{\{\kappa_i\}}(x-x')$ by delta-like potentials. Then, switching to the right- and left-mover

representation, the Hamiltonian (2.14) can be written in the form

$$\begin{aligned} H_I &= H_f + H_x + H_b, \\ H_f &= \frac{e^2}{2} \int dx \left[\gamma_0 \rho^2(x) + \frac{\gamma_1}{4} \sum_{\kappa} \rho_{L\kappa}(x) \rho_{R\kappa}(x) \right], \end{aligned} \quad (2.16)$$

$$H_x = \frac{e^2 \gamma_1}{8} \int dx \left[\sum_{\kappa} \rho_{L\kappa\bar{\kappa}}(x) \rho_{R\bar{\kappa}\kappa}(x) + 2 \sum_{\kappa\kappa'} \mathbf{S}_{L\kappa\kappa'}(x) \mathbf{S}_{R\kappa'\kappa}(x) \right], \quad (2.17)$$

$$H_b = \frac{e^2 \gamma_b}{2} \sum_{\alpha\alpha'\kappa} \int dx \rho_{\alpha\kappa\bar{\kappa}}(x) \rho_{\alpha'\bar{\kappa}\kappa}(x), \quad \alpha, \alpha' = L, R, \quad \kappa = \pm, \quad \bar{\kappa} = \mp. \quad (2.18)$$

Here H_f describes the ‘‘forward scattering’’ processes, H_x is the exchange interaction, and H_b corresponds to ‘‘backscattering’’,

$$\begin{aligned} \rho_{\alpha\kappa\kappa'}(x) &= \sum_{\sigma} \psi_{\alpha\kappa\sigma}^{\dagger}(x) \psi_{\alpha\kappa'\sigma}(x), \quad \rho_{\alpha\kappa}(x) = \rho_{\alpha\kappa\kappa}(x), \quad \rho(x) = \sum_{\alpha\kappa} \rho_{\alpha\kappa}(x), \\ \mathbf{S}_{\alpha\kappa\kappa'}(x) &= \sum_{\sigma\sigma'} \psi_{\alpha\kappa\sigma}^{\dagger}(x) \boldsymbol{\tau}_{\sigma\sigma'} \psi_{\alpha\kappa'\sigma'}(x), \end{aligned}$$

$\boldsymbol{\tau}_{\sigma\sigma'}$ is the vector of Pauli matrices. The effective coupling constants γ_0 , γ_1 , and γ_b are given by the equations:

$$e^2 \gamma_0 = \int \frac{d^2 \mathbf{r}}{2\pi R_0} U(\mathbf{r}), \quad \gamma_1 \approx (2q_F d_x^{AB})^2 \gamma_0, \quad e^2 \gamma_b = \int \frac{d^2 \mathbf{r}}{2\pi R_0} e^{i\mathbf{K}\mathbf{r}} U(\mathbf{r}), \quad (2.19)$$

where $d_x^{pp'}$ is the x -component of the vector $\mathbf{d}_{pp'}$, $q_F = E_F/(\hbar v_F)$. For carbon nanotube, $d^{AB} = 1.44 \text{ \AA}$, $q_F \approx 1/(3R_0)$, $R_0 \approx 4 \text{ \AA}$ [18], $K = 4\pi/(a_0\sqrt{3})$, $a_0 = 2.5 \text{ \AA}$ [49], then $\gamma_0 = 1.3$, $\gamma_1 \approx 0.09$, $\gamma_b \approx 0.08$, i.e., $\gamma_1, \gamma_b \ll \gamma_0$.

The electron density $\rho_{\alpha\kappa\sigma}$ can be expressed in terms of the derivative fields $\partial_x \varphi_{\alpha\kappa\sigma}$ similar to (2.3)

$$: \rho_{L\kappa\sigma}(x) : = \frac{1}{2\pi} \partial_x \varphi_{L\kappa\sigma}(x), \quad : \rho_{R\kappa\sigma}(x) : = -\frac{1}{2\pi} \partial_x \varphi_{R\kappa\sigma}(x).$$

Here $: \rho_{\alpha\kappa\sigma} := \rho_{\alpha\kappa\sigma} - \langle 0 | \rho_{\alpha\kappa\sigma} | 0 \rangle$ denotes fermion normal ordering with respect to the Fermi sea $|0\rangle$ [38]. The fields $\varphi_{\alpha\kappa\sigma}(x)$ satisfy the following commutation relations

$$[\varphi_{L/R \kappa\sigma}(x), \varphi_{L/R \kappa'\sigma'}(x')] = \mp i\pi \delta_{\kappa\kappa'} \delta_{\sigma\sigma'} \text{sign}(x - x'), \quad [\varphi_{L\kappa\sigma}(x), \varphi_{R\kappa'\sigma'}(x')] = 0.$$

It is natural to introduce the standard linear combinations $\theta_{\lambda\nu}(x)$ and their dual fields $\phi_{\lambda\nu}(x)$ subject to the algebra

$$[\theta_{\lambda\nu}(x), \phi_{\lambda'\nu'}(x')] = -\frac{i}{2} \delta_{\lambda\lambda'} \delta_{\nu\nu'} \text{sign}(x - x'). \quad (2.20)$$

The bosonic density fields $\theta_{\lambda\nu}(x)$ for the total ($\nu = g$) and relative ($\nu = u$) charge ($\lambda = c$) and spin ($\lambda = s$) channels are constructed as

$$\begin{aligned} \theta_{c,g/u} &= \frac{1}{4\sqrt{\pi}} [\varphi_{L+\uparrow} - \varphi_{R+\uparrow} \pm \varphi_{L-\uparrow} \mp \varphi_{R-\uparrow} + \varphi_{L+\downarrow} - \varphi_{R+\downarrow} \pm \varphi_{L-\downarrow} \mp \varphi_{R-\downarrow}], \\ \theta_{s,g/u} &= \frac{1}{4\sqrt{\pi}} [\varphi_{L+\uparrow} - \varphi_{R+\uparrow} \pm \varphi_{L-\uparrow} \mp \varphi_{R-\uparrow} - \varphi_{L+\downarrow} + \varphi_{R+\downarrow} \mp \varphi_{L-\downarrow} \pm \varphi_{R-\downarrow}]. \end{aligned}$$

Their dual phase fields $\phi_{\lambda\nu}$ are defined similarly

$$\begin{aligned}\phi_{c,g/u} &= \frac{1}{4\sqrt{\pi}} [\varphi_{L+\uparrow} + \varphi_{R+\uparrow} \pm \varphi_{L-\uparrow} \pm \varphi_{R-\uparrow} + \varphi_{L+\downarrow} + \varphi_{R+\downarrow} \pm \varphi_{L-\downarrow} \pm \varphi_{R-\downarrow}], \\ \phi_{s,g/u} &= \frac{1}{4\sqrt{\pi}} [\varphi_{L+\uparrow} + \varphi_{R+\uparrow} \pm \varphi_{L-\uparrow} \pm \varphi_{R-\uparrow} - \varphi_{L+\downarrow} - \varphi_{R+\downarrow} \mp \varphi_{L-\downarrow} \mp \varphi_{R-\downarrow}].\end{aligned}$$

The Hamiltonian H_f can be written purely in terms of charge bosonic field operators $\theta_{c,g/u}(x)$ and $\pi_{c,g/u}(x) = \partial_x \phi_{c,g/u}(x)$,

$$H_f = e^2 \int dx \left\{ \left(2\gamma_0 - \frac{\gamma_1}{8} \right) (\partial_x \theta_{cg}(x))^2 - \frac{\gamma_1}{8} [\pi_{cg}^2(x) + \pi_{cu}^2(x) - (\partial_x \theta_{cu}(x))^2] \right\}.$$

The Hamiltonian H_x leads to nonlinearities in the θ_{cu} charge field and the $\theta_{s,g/u}$ spin fields. The four channels are obtained by combining charge and spin degrees of freedom as well as symmetric and antisymmetric linear combinations of the two Fermi points, $\kappa = \pm$. The bosonized expression for H_x reads [55]

$$\begin{aligned}H_x &= -\frac{4\gamma_1}{L^2} \int dx : \left[\cos(\sqrt{4\pi} \theta_{cu}(x)) \cos(\sqrt{4\pi} \theta_{su}(x)) + \right. \\ &\quad \left. + \cos(\sqrt{4\pi} \theta_{cu}(x)) \cos(\sqrt{4\pi} \theta_{sg}(x)) - \cos(\sqrt{4\pi} \theta_{sg}(x)) \cos(\sqrt{4\pi} \theta_{su}(x)) \right] : .\end{aligned}\quad (2.21)$$

Here $: \dots :$ denotes boson-normal-ordering defined as follows: to boson-normal-order a function of operators of creation and annihilation of bosons, all creation operators are to be moved to the left of all annihilation operators.

Similar to H_x , the backscattering Hamiltonian leads to nonlinearities in the θ_{cu} and θ_{su} fields. The bosonized expression for H_b takes the form [55]

$$\begin{aligned}H_b &= \frac{4\gamma_b}{L^2} \int dx : \left[\cos(\sqrt{4\pi} \theta_{cu}(x)) \cos(\sqrt{4\pi} \theta_{su}(x)) + \right. \\ &\quad \left. + \cos(\sqrt{4\pi} \theta_{cu}(x)) \cos(\sqrt{4\pi} \phi_{su}(x)) + \cos(\sqrt{4\pi} \theta_{su}(x)) \cos(\sqrt{4\pi} \phi_{su}(x)) \right] : .\end{aligned}\quad (2.22)$$

Writing the non-interacting Hamiltonian H_0 (2.12) in terms of bosonic field operators, one obtains

$$H = \sum_{\lambda\nu} H_{\lambda\nu} + H_x + H_b, \quad H_{\lambda\nu} = \frac{\hbar v_{\lambda\nu}}{2} \int dx \left[g_{\lambda\nu} \pi_{\lambda\nu}^2(x) + \frac{1}{g_{\lambda\nu}} (\partial_x \theta_{\lambda\nu}(x))^2 \right], \quad (2.23)$$

where $\lambda = c, s; \nu = g, u$; H_x is given by Eq. (2.21), H_b is given by Eq. (2.22),

$$v_{\lambda\nu} = \frac{v_F}{g_{\lambda\nu}}, \quad g_{cg} \equiv g = \left[\frac{1 - \tilde{g}_1}{1 + \tilde{g}_0 + \tilde{g}_1} \right]^{1/2} \approx 0.25, \quad g_{cu} \approx g_{s,g/u} \approx 1.$$

Here

$$\tilde{g}_1 = \frac{\gamma_1 e^2}{4\hbar v_F}, \quad \tilde{g}_0 = \frac{4\gamma_0 e^2}{\hbar v_F}.$$

Clearly, the charged (cg) mode propagates with significantly higher velocity than the three neutral modes. There is a further renormalization of the values v_{cu} and $v_{s,g/u}$, however, this

effect is very small and can be neglected. Renormalization group analysis [51] shows that the contribution H_x is *marginally irrelevant*, whereas the backscattering part H_b is *marginally relevant*.

There are several possible regimes in which a nanotube can exist [4]. First, there is an insulating regime with the density at half filling ($q_F = 0$), where all excitations are gapped. Second, there are conducting states which can be realized by applying various external fields. These fields may close some gaps or even all of them, provided their magnitudes exceed certain critical values. For example, by varying the chemical potential (or changing q_F), one can close all the gaps. This leads to a transition into a metallic regime.

2.5 Sliding Luttinger Liquid Phase

The simplest $2D$ ensemble of $1D$ nanoobjects is an array of parallel quantum wires or nanotubes. The inter-wire interaction may transform the LL state existing in isolated quantum wires into various phases of $2D$ quantum liquid. However, the density-density or/and current-current inter-wire interactions do not modify the low-energy behavior of quantum arrays under certain conditions. In particular, it was shown recently [22] that “vertical” interaction which depends only on the distance between the wires, imparts the properties of a *sliding phase* to $2D$ array of $1D$ quantum wires.

In this Section, a $2D$ array of coupled $1D$ quantum wires is considered and the question of existence of a stable $2D$ phase that retains some of the properties of $1D$ Luttinger liquid is addressed. Following Ref. [22] this phase will be called as *sliding Luttinger liquid* (SLL). An anisotropic $2D$ system composed of parallel chains with spinless Luttinger liquids (LL) in each chain (LL in the spin-gapped phase) is considered. It will be shown that the long-wavelength density-density and/or current-current interactions between neighboring Luttinger liquids are marginal operators which result in the sliding Luttinger-liquid phase.

Let us consider an array with N chains, each labelled by an integer $n_2 = 1, 2, \dots, N$. The conventional LL regime in a single $1D$ quantum wire is characterized by bosonic fields describing charge modes (LL in the spin-gapped phase). It is assumed that all wires of the array are identical. They have the same length L , Fermi velocity v and Luttinger liquid parameter g . The period of the array is a . The axis x_1 is chosen along the array direction, whereas the x_2 axis is perpendicular to the array. The excitation motion in QCB is one-dimensional in major part of the $2D$ plane. The anisotropy in real space imposes restrictions on the possible values of the coordinate x_2 . It should be an integer multiple of the array period a , so that the vector $\mathbf{r} = (x_1, n_2 a)$ characterizes the point with the $1D$ coordinate x_1 lying at the n_2 -th wire of the array. The low-energy Luttinger liquid of each wire with spinless interacting fermions is described by the Hamiltonian (2.6). The Hamiltonian of the

array without inter-wire interaction reads

$$H_1^0 = \frac{\hbar v}{2} \sum_{n_2} \int_{-L/2}^{L/2} dx_1 \left\{ g\pi^2(x_1, n_2 a) + \frac{1}{g} (\partial_{x_1} \theta(x_1, n_2 a))^2 \right\}, \quad (2.24)$$

where θ, π are the conventional canonically conjugate boson fields.

The interactions between the chains correspond to couplings between the long wavelength components of the densities $\rho(x_1, n_2 a)$ and of the currents $j(x_1, n_2 a)$ [23]:

$$H_{\text{int}} = \frac{\pi \hbar v}{2} \sum_{n_2 \neq n'_2} \int_{-L/2}^{L/2} dx_1 \left[W_J(n_2 - n'_2) j(x_1, n_2 a) j(x_1, n'_2 a) + W_\rho(n_2 - n'_2) \rho(x_1, n_2 a) \rho(x_1, n'_2 a) \right]. \quad (2.25)$$

With Eqs. (2.3) and (2.5), the electron density $\rho = \rho_L + \rho_R$ and current $j = \rho_L - \rho_R$ can be expressed in terms of $\partial_{x_1} \theta$ and π respectively. Then the bosonized form of the Hamiltonian $H_1 = H_1^0 + H_{\text{int}}$ for the interacting liquids has the form

$$H_1 = \frac{\hbar v}{2} \sum_{n_2 n'_2} \int_{-L/2}^{L/2} dx_1 \left\{ K_J(n_2 - n'_2) \pi(x_1, n_2 a) \pi(x_1, n'_2 a) + K_\rho(n_2 - n'_2) (\partial_{x_1} \theta(x_1, n_2 a)) (\partial_{x_1} \theta(x_1, n'_2 a)) \right\},$$

where the coupling matrices are

$$K_J(n_2 - n'_2) = (g\delta_{n_2 n'_2} + W_J(n_2 - n'_2)), \quad K_\rho(n_2 - n'_2) = \left(\frac{\delta_{n_2 n'_2}}{g} + W_\rho(n_2 - n'_2) \right).$$

The Hamiltonian H_1 describes coupled harmonic oscillators and can be diagonalized. By introducing Fourier transforms in the direction perpendicular to the wires,

$$\theta(x_1, n_2 a) = \frac{1}{\sqrt{N}} \sum_{q_2} e^{iq_2 n_2 a} \theta_{q_2}(x_1), \quad \pi(x_1, n_2 a) = \frac{1}{\sqrt{N}} \sum_{q_2} e^{iq_2 n_2 a} \pi_{q_2}(x_1),$$

($|q_2| < Q/2$, $Q = 2\pi/a$, $\theta_{q_2}^\dagger = \theta_{-q_2}$, $\pi_{q_2}^\dagger = \pi_{-q_2}$) the Hamiltonian H_1 can be rewritten in the form similar to the Hamiltonian (2.24):

$$H_1 = \sum_{q_2} \frac{\hbar v_{q_2}}{2} \int_{-L/2}^{L/2} dx_1 \left\{ g_{q_2} \pi_{q_2}^\dagger(x_1) \pi_{q_2}(x_1) + \frac{1}{g_{q_2}} (\partial_{x_1} \theta_{q_2}^\dagger(x_1)) (\partial_{x_1} \theta_{q_2}(x_1)) \right\}, \quad (2.26)$$

where the Luttinger liquid parameters g_{q_2} and the velocities v_{q_2} are defined as [23]

$$v_{q_2} = v \sqrt{K_J(q_2) K_\rho(q_2)}, \quad g_{q_2} = \sqrt{\frac{K_J(q_2)}{K_\rho(q_2)}}, \quad K_{J/\rho}(q_2) = \sum_{n_2} K_{J/\rho}(n_2) e^{iq_2 n_2 a}.$$

The Hamiltonian (2.25) is invariant under the transformations $\phi(x_1, n_2a) \rightarrow \phi(x_1, n_2a) + C_{n_2}$ and $\theta(x_1, n_2a) \rightarrow \theta(x_1, n_2a) + D_{n_2}$, where $\pi(x_1, n_2a) = \partial_{x_1}\phi(x_1, n_2a)$, C_{n_2} and D_{n_2} are constants on each wire. The corresponding phase is called as a SLL one [22]. In this phase, the total numbers of left (right) moving electrons on each chain are good quantum numbers and expectation values $\langle \psi_\alpha(x_1, n_2a; t)\psi_{\alpha'}^\dagger(x'_1, n'_2a; 0) \rangle$ ($\alpha, \alpha' = L, R$) for $n_2 \neq n'_2$ are *necessarily zero* in this phase. This corresponds to a perfect charge insulator in the transverse direction. Density correlations in the transverse direction are, however, nontrivial. For short ranged density-density and current-current interactions, they decay exponentially with increasing distance between the wires. The low energy modes are sets of 1D density oscillations (sound) propagating along *each* wire of the array with a wave number k_1 and a phase shift q_2a between adjacent wires. The dispersion of the modes is linear with respect to 1D wave number k_1 , $E(k_1, q_2) = v_{q_2}|k_1|$. These modes can, for instance, transport heat perpendicular to the chains although the system is a perfect charge insulator in this direction.

2.6 Cross-Sliding Luttinger Liquid Phase

Next, a square network of 1D wires formed by coupling two perpendicular arrays of chains is considered. In experimentally realizable setups [9] these are cross-structures of suspended single-wall carbon nanotubes placed in two parallel planes separated by an inter-plane distance d . However, some generic properties of QCB may be described in assumption that QCB is a genuine 2D system. The system consists of two periodically crossed arrays of 1D quantum wires. It is assumed that all wires are identical. They have the same length L , Fermi velocity v and Luttinger parameter g . A coordinate system is chosen so that the axes x_j and the corresponding basic unit vectors \mathbf{e}_j are oriented along the j -th array ($j = 1, 2$ is the array index). The period of crossbars is a , and the basic vectors are $\mathbf{a}_j = a\mathbf{e}_j$ (Fig. 2.4). The interaction between the excitations in different wires includes both interaction between wires from the same array (intra-array interaction) and wires from different arrays (inter-array interaction). The former is given by Eq.(2.25), the latter is assumed to be concentrated around the crossing points with coordinates $n_1\mathbf{a}_1 + n_2\mathbf{a}_2 \equiv (n_1a, n_2a)$. The integers n_j enumerate the wires within the j -th array. Following Refs. [21, 23] it will be shown that it exhibits a new *crossed sliding Luttinger liquid* (CSLL) phase.

The LL of the first array is described by the Hamiltonian H_1 (2.26). The Hamiltonian H_2 of the second array is obtained from H_1 after permutation $1 \leftrightarrow 2$ in the arguments of the fields. The density-density interactions between electrons on intersecting wires gives rise to a term in the Hamiltonian in the form

$$H_{12} = \sum_{n_1 n_2} \int_{-L/2}^{L/2} dx_1 dx_2 V(x_1 - n_1a, x_2 - n_2a) \rho_1(x_1, n_2a) \rho_2(n_1a, x_2), \quad (2.27)$$

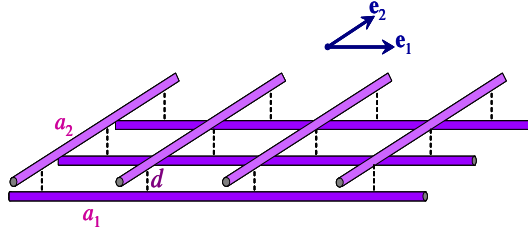


Figure 2.4: 2D crossbars formed by two interacting arrays of parallel quantum wires. Here $\mathbf{e}_1, \mathbf{e}_2$ are the unit vectors of the superlattice, $a_1 = a_2 \equiv a$ is the superlattice period (the case $a_1 \neq a_2$ is considered in Appendix C) and d is the vertical inter-array distance.

where $V(x_1 - n_1a, x_2 - n_2a)$ is a short-range inter-array interaction. Using the definitions $\rho_1(x_1, n_2a) = \partial_{x_1}\theta_1(x_1, n_2a)/\sqrt{\pi}$ and $\rho_2(n_1a, x_2) = \partial_{x_2}\theta_2(n_1a, x_2)/\sqrt{\pi}$, one obtains the bosonized form of the Hamiltonian H_{12} [23]:

$$H_{12} = \frac{1}{\pi} \sum_{n_1 n_2} \int_{-L/2}^{L/2} dx_1 dx_2 V(x_1 - n_1a, x_2 - n_2a) \partial_{x_1}\theta_1(x_1, n_2a) \partial_{x_2}\theta_2(n_1a, x_2). \quad (2.28)$$

Let us introduce Fourier transforms according to [58]

$$\theta_1(x_1, n_2a) = \frac{1}{\sqrt{NL}} \sum_{\mathbf{q}, \mathbf{m}_1} e^{i(q_1 + m_1 Q)x_1 + iq_2 n_2 a} \theta_{1\mathbf{q} + \mathbf{m}_1}, \quad (2.29)$$

$$\theta_2(n_1a, x_2) = \frac{1}{\sqrt{NL}} \sum_{\mathbf{q}, \mathbf{m}_2} e^{iq_1 n_1 a + i(q_2 + m_2 Q)x_2} \theta_{2\mathbf{q} + \mathbf{m}_2}, \quad (2.30)$$

where wave vector \mathbf{q} belongs to the first Brillouin zone, $|q_{1,2}| < Q/2$, $\mathbf{m}_{1,2} = m_{1,2}Q\mathbf{e}_{1,2}$ are reciprocal superlattice vectors [61, 65] ($Q = 2\pi/a$ is reciprocal superlattice constant and $m_{1,2}$ are integers). Then removing degrees of freedom with wavelenghtes smaller than $2a$ (that is, considering only the modes with $\mathbf{m}_{1,2} = 0$), one obtains the total Hamiltonian $H = H_1 + H_2 + H_{12}$ [23]

$$H = \sum_{\mathbf{q}} \left(\frac{\hbar v_{q_2} g_{q_2}}{2} \pi_{1\mathbf{q}}^\dagger \pi_{1\mathbf{q}} + \frac{\hbar v_{q_1} g_{q_1}}{2} \pi_{2\mathbf{q}}^\dagger \pi_{2\mathbf{q}} \right) + \frac{\hbar v}{2g} \sum_{ij\mathbf{q}} \theta_{i\mathbf{q}}^\dagger \Omega_{\mathbf{q}}^{ij} \theta_{j\mathbf{q}}, \quad (2.31)$$

where $i, j = 1, 2$ denote the array number,

$$\Omega_{\mathbf{q}}^{ij} = q_i q_j \left[\left(\frac{v_{q_2}}{v} \frac{g}{g_{q_2}} \delta_{j1} + \frac{v_{q_1}}{v} \frac{g}{g_{q_1}} \delta_{j2} \right) \delta_{ij} + g \tilde{V}(\mathbf{q})(1 - \delta_{ij}) \right],$$

$$\tilde{V}(\mathbf{q}) = \frac{1}{\pi \hbar v a} \int_{-L/2}^{L/2} dx_1 dx_2 V(x_1, x_2) e^{iq_1 x_1 + iq_2 x_2}.$$

The Hamiltonian (2.31) exhibits a CSLL phase. Renormalization group analysis [23] shows that additional interactions between the two arrays, such as the Josephson and charge-density-wave couplings, are irrelevant and the CSLL phase is stable.

It should be noted that the Hamiltonian (2.31) does not include interactions of the long-wavelength plasmons with quasi-particles whose wavelenghtes smaller than $2a$, i.e., plasmons in higher energy bands. Being weak, these interactions renormalize the plasmon velocity (see Eq. (B.1)). When the interaction strength increases, the lowest QCB modes soften and their frequencies vanish *in a whole BZ* at a certain critical of the interaction strength (see Section 3.4).

2.7 Quantum Crossbars with Virtual Wire-to-Wire Tunneling

To finalize the substantiation of the CSLL family, consider the condition when the tunneling of electrons in quantum crossbars is suppressed and the Luttinger-liquid-like phase is stable. For the case when the charge degrees of freedom are quenched, we derive the effective spin Hamiltonian of QCB.

Let us consider two non-parallel metallic nanotubes. One of them belongs to the first array and has the number n_2 , and another one belongs to the second array and has the number n_1 . The intersecting point has the coordinates (n_1a, n_2a) . The electron hopping between the wires gives rise to a term in the Hamiltonian of the form: $\sum_{\sigma} t[\Psi_{1\sigma}^{\dagger}(n_1a, n_2a)\Psi_{2\sigma}(n_1a, n_2a) + h.c.]$, where t is an effective hopping constant, and $\sigma = \uparrow, \downarrow$ is a spin index. Next we introduce “slowly varying” field operators $\psi_{L\sigma}$ and $\psi_{R\sigma}$ (similar to (2.8)). Assuming that the Fermi vector k_F is not commensurate with the reciprocal superlattice vector $Q = 2\pi/a$, we can write $k_F = m_F Q + q_0$, with m_F being integer and $|q_0| < Q/2$. Then we represent the hopping between the two arrays as

$$H_t = t \sum_{n_1 n_2} \sum_{\alpha, \alpha'} \sum_{\sigma} \left[e^{-iq_{\alpha} n_1 a + iq_{\alpha'} n_2 a} \psi_{1\alpha\sigma}^{\dagger}(n_1 a, n_2 a) \psi_{2\alpha'\sigma}(n_1 a, n_2 a) + h.c. \right], \quad (2.32)$$

where $q_L = q_0$ and $q_R = -q_0$. Here and below we assume that t is real and positive.

The energy cost of the electron wire-to-wire tunneling is the energy $2E_C$ necessary to charge both wires,

$$E_C = \frac{2e^2}{L} \ln \left(\frac{L}{2R_0} \right), \quad (2.33)$$

where L is the nanotube length and R_0 is the nanotube radius. The tunneling is suppressed if $t \ll E_C$. The tunneling constant t can be estimated from the transport experiment through crossed nanotubes. The elastic and van der-Waals interactions between crossed nanotubes determine two equilibrium positions [9] with inter-wire distances $d = 1$ nm and 2 nm. It is shown that for $d = 2$ nm, the resistance is $R \sim 10^{10} \Omega$. On the other hand, resistance can be evaluated from the well known Landauer formula

$$R = \frac{1}{G}, \quad G = \frac{2e^2}{h} \frac{\nu_0 t^2}{E_C a^2}, \quad \nu_0 = \frac{L}{2\pi \hbar v_F}, \quad (2.34)$$

where ν_0 is the density of states in the quantum wires. For real nanotubes, the length of a ballistic transport is $L_{\text{exp}} \sim 1\mu\text{m}$ and $E_C \sim 20\text{ meV}$ [18]. Taking $v = 8 \cdot 10^7\text{ cm/sec}$, $R_0 = 0.4\text{ nm}$, and $a = 20\text{ nm}$, we have $t/a \sim 1\text{ }\mu\text{eV}$, i.e., $t \ll E_C$. Then, single-particle hopping between nanotubes is suppressed, and only backward scattering interaction can be relevant. However, if k_F is not commensurate with the reciprocal lattice constant Q , the back scattering is also suppressed.

In this case the effective interaction Hamiltonian can be obtained from the initial one (2.32) by means of elimination the states from adjacent charge sectors by using the second order perturbation theory with respect to $t/(aE_C) \ll 1$:

$$H_{\text{int}} = \frac{t^2}{2E_C} \sum_{n_1 n_2} \{ \rho_1(n_1 a, n_2 a) \rho_2(n_1 a, n_2 a) + 2\mathbf{S}_1(n_1 a, n_2 a) \cdot \mathbf{S}_2(n_1 a, n_2 a) \}. \quad (2.35)$$

Here ρ_j is the electron density operator and \mathbf{S}_j is the spin operator,

$$\rho_j = \sum_{\alpha\sigma} \psi_{j\alpha\sigma}^\dagger \psi_{j\alpha\sigma}, \quad \mathbf{S}_j = \frac{1}{2} \sum_{\alpha\sigma\sigma'} \psi_{j\alpha\sigma}^\dagger \boldsymbol{\tau}_{\sigma\sigma'} \psi_{j\alpha\sigma'},$$

where $\boldsymbol{\tau}$ is the vector of Pauli matrices.

The first term under the sum in the right-hand side of Eq.(2.35) describes the potential interaction between charge fluctuations and simply renormalizes the coupling strength $V(x_1, x_2)$ of the Coulomb inter-wire interaction (2.27). The second term under the sum in the right-hand side of Eq.(2.35) is spin-spin inter-wire interaction.

The Hamiltonian (2.35) shows that the virtual wire to wire hopping results in only a slight renormalization of the strength of the capacitive inter-wire interaction. However, the virtual hopping results in the effective spin-spin interaction.

Short summary and future outlook: *It was demonstrated in this Chapter that the LL fixed point is conserved in a quasi 2D periodic network (quantum crossbars). In the following chapters we concentrate on another aspect of the problem: we consider the properties of QCB at finite wave vectors \mathbf{q} and frequencies ω in the whole 2D Brillouin zone, study the spectrum of Bose excitations $\omega(q_1, q_2)$, consider situations where dimensional crossover $1D \leftrightarrow 2D$ occurs, formulate the principles of infrared and ultraviolet spectroscopy for QCB and study the basic characteristics of the spectra.*

Chapter 3

Plasmon Excitations and One to Two Dimensional Crossover in Quantum Crossbars

In this Chapter we analyze the spectrum of a specific nano-object - square double quantum crossbars (QCB). We show that the standard bosonization procedure is valid and the system behaves as cross-sliding Luttinger liquid in the infrared limit. However plasmon excitations in QCB demonstrate both $1D$ and $2D$ behavior depending on the direction of the plasmon wave vector. We discuss several crossover effects such as appearance of non-zero transverse space correlators and the periodic energy transfer between arrays (“Rabi oscillations”). The spectra of a tilted double and triple QCB are considered in Appendices C and D.

3.1 Introduction

A double $2D$ grid, i.e., two superimposed crossing arrays of parallel conducting quantum wires or nanotubes, represents a specific nano-object which is called quantum crossbars (QCB). Its spectral properties cannot be treated in terms of purely $1D$ or $2D$ electron liquid theory. A constituent element of QCB (quantum wire or nanotube) possesses the LL-like spectrum [17, 18]. A single array of parallel quantum wires is still a LL-like system qualified as a sliding phase [16] provided only the electrostatic interaction between adjacent wires is taken into account. If tunnelling is suppressed and the two arrays are coupled only by electrostatic interaction in the crosses, the system possesses the LL zero energy fixed point.

In the present Chapter we concentrate on another aspect of the problem of capacitively interacting arrays of quantum wires. Instead of studying the conditions under which the LL behavior is preserved in spite of inter-wire interaction, we show that a rich Bose-type excitation spectrum (plasmon modes) arises at finite energies in the $2D$ Brillouin zone (BZ)

[56, 57] and consider situations where the *dimensional crossover* from $1D$ to $2D$ occurs [58, 59]. We start our studies of QCB with a double square QCB, namely, $m = 2$. In the first two Sections 3.2 and 3.3 we introduce basic notations and construct the Hamiltonian of the QCB. The main approximations are discussed in Section 3.4. Here we substantiate the method used (separable interaction approximation) and show that interaction between arrays in QCB is weak. The energy spectra for square QCB are described in detail in Section 3.5. Various correlation functions and related experimentally observable quantities (optical absorption, space correlators) are discussed in the last Section 3.6. We predict here the effect of peculiar “Rabi oscillations” - periodic energy transfer from one of the QCB array to another. All technical details are placed in Appendices A and B.

Double tilted QCB is considered in Appendix C. Triple QCB ($m = 3$) formed by three arrays lying in parallel planes are studied in Appendix D. Such hexagonal grids may be useful for three-terminal nanoelectronic devices [8]. The plasmon spectra of triple QCB possess some specific features in comparison with double QCB. We introduce the main notions and construct the Hamiltonian of symmetric triple QCB (section D.1), analyze the peculiarities of the frequency spectrum (section D.2), and illustrate them by description of triple Rabi oscillations - periodic energy transfer between all three arrays (part D.3). The results are summarized in the Conclusions.

3.2 Basic Notions

Double square QCB is a $2D$ periodic grid, which is formed by two periodically crossed arrays of $1D$ quantum wires. In experimentally realizable setups [9] these are cross-structures of suspended single-wall carbon nanotubes placed in two parallel planes separated by an inter-plane distance d . However, some generic properties of QCB may be described in the assumption that QCB is a genuine $2D$ system. We assume that all wires of QCB are identical. They have the same length L , Fermi velocity v and Luttinger parameter g . The periods of a crossbars is a . The arrays are oriented along the unit vectors $\mathbf{e}_{1,2}$, and corresponding basic vectors are $\mathbf{a}_j = a\mathbf{e}_j$ (Fig. 2.4).

The interaction between the excitations in different wires is assumed to be concentrated around the crossing points with coordinates $n_1\mathbf{a}_1 + n_2\mathbf{a}_2 \equiv (n_1a, n_2a)$. The integers n_j enumerate the wires within the j -th array. Such an interaction imposes a super-periodicity on the energy spectrum of initially one dimensional quantum wires, and the eigenstates of this superlattice are characterized by a $2D$ quasimomentum $\mathbf{q} = q_1\mathbf{e}_1 + q_2\mathbf{e}_2 \equiv (q_1, q_2)$. The corresponding basic vectors of the reciprocal superlattice have the form $\mathbf{m} = \mathbf{m}_1 + \mathbf{m}_2$, where $\mathbf{m}_{1,2} = m_{1,2}Q\mathbf{e}_{1,2}$, $Q = 2\pi/a$ and $m_{1,2}$ are integers.

However, the crossbars kinematics differs from that of a standard $2D$ periodic system. In conventional $2D$ systems, forbidden states in the inverse space arise due to Bragg diffraction

in a $2D$ periodic potential, whereas the whole plane is allowed for wave propagation in real space, at least when the periodic potential is weak enough. A set of Bragg lines correspond to different reciprocal lattice vectors \mathbf{m} . A Brillouin zone is bounded by the Bragg lines. It coincides with a Wigner-Seitz cell of reciprocal lattice (Fig. 3.1a). In contrast, most of the real space is forbidden for electron and plasmon propagation in sharply anisotropic QCB. The Bragg conditions for the wave vectors of a quasi-particle in an array are modulated by a periodic potential created by another array, unlike those in conventional $2D$ plane. There are two sets of Bragg lines corresponding to reciprocal lattice vectors \mathbf{m}_1 and \mathbf{m}_2 . These conditions are essentially one-dimensional. The corresponding BZ is a Wigner-Seitz cell of a reciprocal lattice shown in Fig. 3.1b.

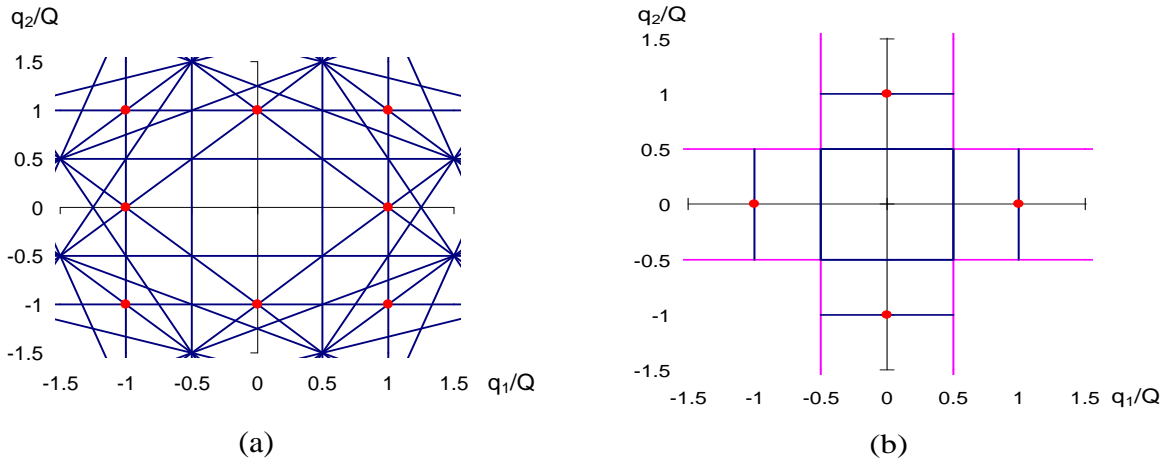


Figure 3.1: The Bragg lines in conventional $2D$ square lattice (a) and that of $2D$ square crossbars (b). In both panels, solid lines are the Bragg lines, whereas points correspond to reciprocal superlattice vectors.

Indeed, the excitation motion in QCB is one-dimensional in major part of the $2D$ plane. The anisotropy in real space imposes restrictions on the possible values of $2D$ coordinates x_1, x_2 ($\mathbf{r} = x_1\mathbf{e}_1 + x_2\mathbf{e}_2$). At least one of them, e.g., x_2 (x_1) should be an integer multiple of the corresponding array period a , so that the vector $\mathbf{r} = (x_1, n_2a)$ ($\mathbf{r} = (n_1a, x_2)$) characterizes the point with the $1D$ coordinate x_1 (x_2) lying at the n_2 -th (n_1 -th) wire of the first (second) array. As a result, one cannot resort to the standard basis of $2D$ plane waves when constructing the eigenstate with a given wave vector \mathbf{k} . Even in *non-interacting* arrays of quantum wires (empty superlattice) the $2D$ basis is formed as a superposition of two sets of $1D$ waves. The first of them is a set of $1D$ excitations propagating along *each* wire of the first array characterized by a unit vector $k_1\mathbf{e}_1$ with a phase shift ak_2 between adjacent wires. The second set is the similar manifold of excitations propagating along the wires of the second array with the wave vector $k_2\mathbf{e}_2$ and the phase shift ak_1 . The dispersion law of these excitations has the form $\omega^0(\mathbf{k}) = \omega(k_1) + \omega(k_2)$. The states of equal energy obtained by means of this procedure form straight lines in the $2D$ reciprocal space. For example, the Fermi surface of QCB developed from the points $\pm k_{F1,2}$ for individual quantum wire consists

of two sets of lines $|k_{1,2}| = k_{F1,2}$. Respectively, the Fermi sea is not a circle with radius k_F like in the case of free $2D$ gas, but a cross in the k plane bounded by these four lines [15] (see Fig. 3.2). Finally, the Bragg conditions read

$$\omega(k_1) - \omega(k_1 + m_1 Q) + \omega(k_2) - \omega(k_2 + m_2 Q) = 0.$$

and the lines $|k_1| = Q/2$ and $|k_2| = Q/2$ satisfying these conditions, form a $2D$ BZ of double QCB.

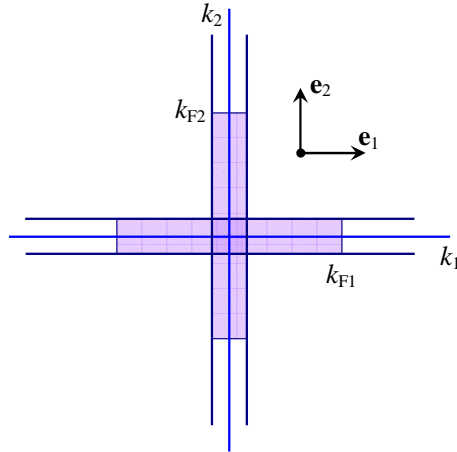


Figure 3.2: Fermi surface of $2D$ metallic quantum bars in the absence of charge transfer between wires.

Due to the inter-array interaction, the plasmons in QCB (see Figs. 3.3, C.1 below) exist in a $2D$ Brillouin zone. These excitations are characterized by the quasimomentum $\mathbf{q} = (q_1, q_2)$. However, in case of weak interaction, the $2D$ waves are constructed from the $1D$ plane waves in accordance with the above procedure. Two sets of $1D$ plane waves form an appropriate basis for the description of elementary excitations in QCB in close analogy with the nearly free electron approximation in conventional crystalline lattices. It is easily foreknown that a weak inter-array interaction does not completely destroy the above quasimomentum classification of eigenstates, and the $2D$ reconstruction of the spectrum may be described in terms of wave mixing similarly to the standard Bragg diffraction in a weak periodic potential. Moreover, the classification of eigenstates of an empty superlattice may be effectively employed for the classification of energy bands in a real QCB superlattice where the super-periodicity is imposed by interaction.

Complete kinematics of an empty super-chain (wave functions, dispersion laws, relations between quasiparticle second quantization operators) is developed in Appendix A. In terms of these $1D$ Bloch functions (see Eqs. (A.1), (A.2) of Appendix A) we construct the $2D$ basis of Bloch functions for an empty superlattice

$$\Psi_{ss'\mathbf{q}}(\mathbf{r}) = \psi_{sq_1}(x_1)\psi_{s'q_2}(x_2). \quad (3.1)$$

Here $s, s' = 1, 2, \dots$, are the band numbers, and the $2D$ quasimomentum $\mathbf{q} = (q_1, q_2)$ belongs to the first BZ, $|q_j| \leq Q/2$. The corresponding eigenfrequencies

$$\omega_{ss'}(\mathbf{q}) = \omega_{1s}(q_1) + \omega_{2s'}(q_2).$$

Here $\omega_{js}(q_j) \equiv \omega_s(q_j)$, and $\omega_s(q_j)$ are formed by two $1D$ acoustic branches propagating along the j -th array and belonging to the band s . Their explicit form is defined in Appendix A (Eq.(A.2)). Alternatively, each mode with quasimomentum \mathbf{q} in the energy band s (reduced BZ description) propagating along the j -th array can be described by the wave vector $\mathbf{q} + \mathbf{m}_j$ (extended BZ description), where $\mathbf{m}_j = m_j Q \mathbf{e}_j$ and $m_j = (-1)^s \text{sign}(q_j)[s/2]$. We will use both these bases in the next Section when constructing the excitation spectrum of QCB within the reduced band scheme and in the next Chapters where we formulate the spectroscopic principles of QCB within the extended band scheme.

3.3 Hamiltonian

When turning to the description of interaction in a QCB, one should refer to a real geometry of crossbars, and recollect the important fact that the equilibrium distance between two arrays is finite and large enough to suppress direct electron tunnelling [9]. We neglect also the elastic and van der-Waals components of the interaction between real nanotubes, because these interactions are not involved in the formation of collective excitations in QCB. Then the full Hamiltonian of the QCB is

$$H_{QCB} = H_1 + H_2 + H_{12}, \quad (3.2)$$

where the Hamiltonian H_1 (2.24) describes the $1D$ boson field in the first array, the Hamiltonian H_2 is obtained from H_1 after permutation $1 \leftrightarrow 2$ in the arguments of the fields.

The inter-wire interaction includes both interactions between wires from the same array (intra-array interaction) and wires from different arrays (inter-array interaction). The latter is the Hamiltonian (2.28) which results from a contact capacitive coupling in the crosses of the bars. Physically, the short-range inter-array interaction $V(x_1 - n_1 a, n_2 a - x_2)$ represents the screened Coulomb interaction between charge fluctuations around the crossing point $(n_1 a, n_2 a)$. We assume that the crossed nanotubes are suspended in an unpolarized medium, and screening arises due to intra-wire interaction. The nanotube diameter is the only physical parameter which determines the screening length r_0 in a tube (see e.g. Ref.[46]). We describe the re-distribution of a charge in tube j induced by the interaction with tube i by the envelope function (introduced phenomenologically)

$$\zeta(\xi_j), \quad \xi_j = \frac{x_j - n_j a}{r_0}, \quad \zeta(\xi) = \zeta(-\xi), \quad \zeta(0) \sim 1. \quad (3.3)$$

This function is of order unity for $|\xi| \sim 1$ and vanishes outside this region. Thus the on-cross interaction is introduced as

$$V(\mathbf{r}_{12}) = \frac{V_0}{2} \Phi \left(\frac{x_1 - n_1 a}{r_0}, \frac{n_2 a - x_2}{r_0} \right), \quad \Phi(\xi_1, \xi_2) = \frac{\zeta(\xi_1)\zeta(\xi_2)}{\sqrt{1 + \frac{|\mathbf{r}_{12}|^2}{d^2}}}, \quad (3.4)$$

where $\mathbf{r}_{12} = r_0 \xi_1 \mathbf{e}_1 - r_0 \xi_2 \mathbf{e}_2$. It is seen from these equations that $\Phi(\xi_1, \xi_2)$ vanishes for $|\xi_{1,2}| \geq 1$ and satisfies the condition $\Phi(0, 0) \sim 1$. The effective coupling strength is

$$V_0 = \frac{2e^2}{d}. \quad (3.5)$$

In terms of boson field operators θ_j , the inter-array interaction is written in the form similar to (2.28)

$$H_{int} = V_0 \sum_{n_1, n_2} \int dx_1 dx_2 \Phi \left(\frac{x_1 - n_1 a}{r_0}, \frac{n_2 a - x_2}{r_0} \right) \partial_{x_1} \theta_1(x_1, n_2 a) \partial_{x_2} \theta_2(n_1 a, x_2). \quad (3.6)$$

As for the inter-wire interaction within each array, one can neglect it for a couple of reasons. First, the inter-wire distance within the same array is much larger than the inter-array distance. Second, this interaction is irrelevant in the long-wave limit [23]. Thus Eq. (3.6) is the full interaction Hamiltonian.

In the quasimomentum representation (3.1) the full Hamiltonian (3.2) acquires the form,

$$H_{QCB} = \frac{\hbar v g}{2} \sum_{j=1}^2 \sum_{s, \mathbf{q}} \pi_{j s \mathbf{q}}^\dagger \pi_{j s \mathbf{q}} + \frac{\hbar}{2 v g} \sum_{j j'=1}^2 \sum_{s s' \mathbf{q}} \Omega_{j j' s s' \mathbf{q}} \theta_{j s \mathbf{q}}^\dagger \theta_{j' s' \mathbf{q}}, \quad (3.7)$$

where $\theta_{j s \mathbf{q}}$ and $\pi_{j s \mathbf{q}}$ are the Fourier components of the boson fields θ_j and π_j .

The matrix elements for inter-array coupling are given by:

$$\Omega_{j j' s s' \mathbf{q}} = \omega_s(q_j) \omega_{s'}(q_{j'}) [\delta_{j j'} \delta_{s s'} + \phi \Phi_{s s' \mathbf{q}} (1 - \delta_{j j'})], \quad \phi = \frac{g V_0 r_0^2}{\hbar v a}. \quad (3.8)$$

Here $\omega_s(q_j) = v ([s/2]Q + (-1)^{s-1}|q_j|)$ are eigenfrequencies of the ‘‘unperturbed’’ 1D mode (see Eq. (A.2) of Appendix A), pertaining to an array j , band s and quasimomentum $\mathbf{q} = q_j \mathbf{e}_j$. The coefficients

$$\Phi_{s s' \mathbf{q}} = (-1)^{s+s'} \text{sign}(q_1 q_2) \int d\xi_1 d\xi_2 \Phi(\xi_1, \xi_2) e^{-i r_0 (q_1 \xi_1 + q_2 \xi_2)} u_{s q_1}^*(r_0 \xi_1) u_{s' q_2}^*(r_0 \xi_2), \quad (3.9)$$

($\Phi_{s s' \mathbf{q}} = \Phi_{s' s \mathbf{q}}^*$) are proportional to the dimensionless Fourier component of the interaction strengths, where the Bloch amplitudes $u_{s q_j}(x_j)$ are given by Eq. (A.2) of Appendix A.

The Hamiltonian (3.7) describes a system of coupled harmonic oscillators, which can be *exactly* diagonalized with the help of a certain canonical linear transformation (note that it is already diagonal with respect to the quasimomentum \mathbf{q}). The diagonalization procedure is, nevertheless, rather cumbersome due to the mixing of states belonging to different bands and arrays. However, it will be shown below that provided $d \gg r_0$, a separable potential approximation is applicable, that significantly simplifies the calculations.

3.4 Approximations

As it has already been mentioned, we consider the rarefied QCB with short range capacitive interaction. In the case of QCB formed by nanotubes, this is a screened Coulomb interaction at a distance of the order of the nanotube radius R_0 [46], therefore $r_0 \sim R_0$. The minimal radius of a single-wall carbon nanotube is about $R_0 = 0.35 \div 0.4nm$ (see Ref. [54]). The inter-tube vertical distance d in artificially fabricated nanotube networks is estimated as $d \approx 2nm$ (see Ref. [9]). Therefore the ratio $r_0^2/d^2 \approx 0.04$ is really small and *the dimensionless interaction* $\Phi(\xi_1, \xi_2)$ (3.4) *in the main approximation is separable*

$$\Phi(\xi_1, \xi_2) \approx \Phi_0(\xi_1, \xi_2) = \zeta(\xi_1)\zeta(\xi_2). \quad (3.10)$$

To diagonalize the Hamiltonian (3.7), one should solve the system of equations of motion for the field operators. The generalized coordinates θ satisfy the equations

$$[\omega_s^2(q_1) - \omega^2] \theta_{1s\mathbf{q}} + \sqrt{\varepsilon} \zeta_s(q_1) \omega_s(q_1) \frac{r_0}{a} \sum_{s'} \zeta_{s'}(q_2) \omega_{s'}(q_2) \theta_{2s'\mathbf{q}} = 0, \quad s = 1, 2, \dots, \quad (3.11)$$

and the similar equations obtained by permutation $1 \leftrightarrow 2$. Here

$$\zeta_s(q) = (-1)^s \text{sign}(q) \int d\xi \zeta(\xi) e^{ir_0q\xi} u_{sq}(r_0\xi), \quad (3.12)$$

the Bloch amplitudes $u_{sq}(r_0\xi)$ are defined by Eq. (A.2) of Appendix A, and

$$\varepsilon = \left(\phi \frac{a}{r_0} \right)^2 = \left(\frac{gV_0 r_0}{\hbar v} \right)^2. \quad (3.13)$$

Due to separability of the interaction, the equations of motion (3.11) can be solved exactly. The corresponding eigenfrequencies are determined by the characteristic equation

$$F_{q_1}(\omega^2) F_{q_2}(\omega^2) = \frac{1}{\varepsilon}, \quad (3.14)$$

where

$$F_{q_j}(\omega^2) = \frac{r_0}{a} \sum_s \frac{\zeta_s^2(q_j) \omega_s^2(q_j)}{\omega_s^2(q_j) - \omega^2}. \quad (3.15)$$

The function $F_{q_j}(\omega^2)$ has a set of poles at $\omega^2 = \omega_s^2(q_j)$ ($s = 1, 2, 3, \dots$). For squared frequency smaller than all squared initial eigenfrequencies $\omega_s^2(q_j)$, i.e., within the interval $[0, \omega_1^2(q_j)]$, this is a positive and monotonically increasing function. Its minimal value F_0 on the interval is reached at $\omega^2 = 0$, and it does not depend on quasimomentum q_j

$$F_{q_j}(0) = \frac{r_0}{a} \sum_s \zeta_s^2(q_j) = \int d\xi \zeta^2(\xi) \equiv F_0 \quad (3.16)$$

(here Eqs. (3.15) and (3.12) are used). If the parameter ε is smaller than its critical value $\varepsilon_c = 1/F_0^2$, then all solutions ω^2 of the characteristic equation are positive. When ε increases,

the lowest QCB mode softens and its frequency vanishes *in the entire BZ* at $\varepsilon = \varepsilon_c$. For exponential charge density distribution $\zeta(\xi) = \exp(-|\xi|)$, one obtains $\varepsilon_c \approx 1$.

In our model, the dimensionless interaction ε in Eq.(3.13) can be written as

$$\varepsilon = \left(\frac{2R_0 g e^2}{d \hbar v} \right)^2. \quad (3.17)$$

For nanotube QCB, the first factor within parentheses is about 0.35. The second one which is nothing but the corresponding QCB “fine structure” constant, can be estimated as 0.9 (we used the values of $g = 1/3$ and $v = 8 \times 10^7$ cm/sec, see Ref. [18]). Therefore ε approximately equals 0.1, so this parameter is really small. Thus the considered system is stable, its spectrum is described by Eqs.(3.14), (3.15) with a *small* parameter ε .

The general Eq.(3.14) reduces in the infrared limit $\mathbf{q}, \omega \rightarrow 0$ to an equation describing the spectrum of two coupled sliding phases, i.e., 1 : 1 arrays in accordance with classification scheme, offered in Ref. [23]. Equation (3.13) of this paper is the long wave limit of our equations (B.2) and (B.13) derived in Appendix B. Therefore, the general analysis of stability of the LL fixed point is applicable in our approach.

3.5 Spectrum

Due to the weakness of the interaction, the systematics of unperturbed levels and states is grossly conserved, at least in the low energy region corresponding to the first few energy bands. This means that perturbed eigenstates could be described by the same quantum numbers (array number, band number and quasimomentum) as the unperturbed ones. Such a description fails in two specific regions of reciprocal space. The first of them is the vicinity of the high-symmetry lines $q_j = nQ_j/2$ with n integer. Indeed, as it follows from the equations of motion (3.11), around these lines the inter-band mixing is significant. These lines with $n = \pm 1$ include BZ boundaries. The second region is the vicinity of the lines where the resonance conditions are fulfilled

$$\omega_s^2(q_1) = \omega_s^2(q_2). \quad (3.18)$$

Here inter-array mixing within the same energy band s is significant. In what follows we will pay attention first of all to these two regions because in the rest of the BZ the initial systematics of the energy spectrum can be successfully used.

Equations (3.11), (3.14), describing the wave functions and the dispersion laws are analyzed in Appendix B. We describe below some of these dispersion curves for a square QCB based on this analysis (the case of tilted QCB is described in Appendix C).

We start with the simplest case of square QCB formed by identical wires. This means that all parameters (wire length, space period, Fermi velocity, LL parameter, screening radius)

are the same for both arrays. The corresponding BZ is also a square (see Fig. 3.3). The resonant lines are the diagonals of BZ.

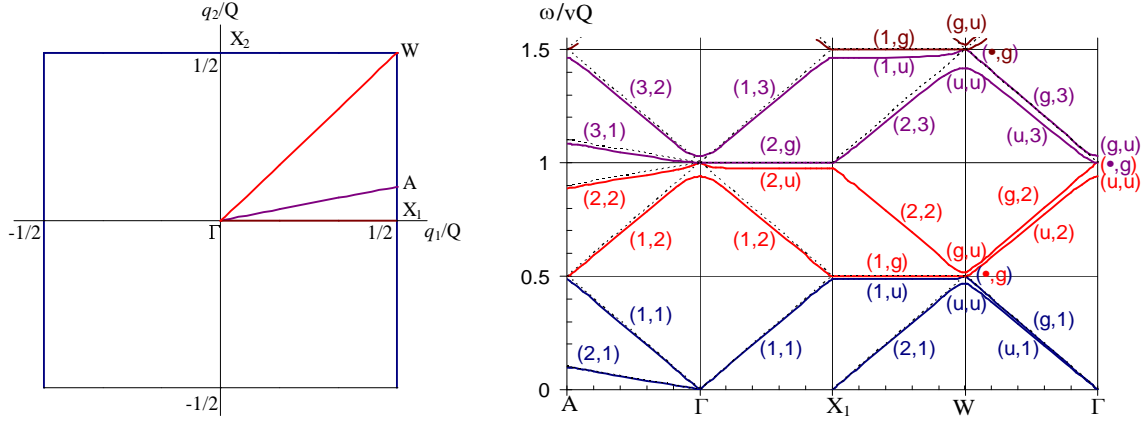


Figure 3.3: Two dimensional BZ of square QCB (left panel). The energy spectrum of QCB (solid lines) and noninteracting arrays (dashed lines) for quasimomenta at the lines AF , ΓX_1 , X_1W , and $W\Gamma$ of BZ (right panel).

In the major part of the BZ, for quasimomenta \mathbf{q} lying far from the diagonals, each eigenstate mostly conserves its initial systematics, i.e. belongs to a given array, and mostly depends on a given quasimomentum component. Corresponding dispersion laws remain linear being slightly modified near the BZ boundaries only. The main change is therefore the renormalization of the plasmon velocity.

i. General case: The point \mathbf{q} lies away from both the high symmetry lines and the resonant lines. This case is illustrated in the left part of Fig. 3.3, where we display dispersion curves corresponding to quasimomenta belonging to a generic ΓA line in the BZ. In what follows we use (j, s) notations for the unperturbed boson propagating along the j -th array in the s -th band. Then the lowest two curves in this part of Fig. 3.3 are, in fact, the slightly renormalized dispersion of $(2, 1)$ and $(1, 1)$ bosons. The middle curves describe $(1, 2)$ and $(2, 2)$ bosons, and the upper curves are the dispersion of $(2, 3)$ and $(1, 3)$ bosons. It is seen that the dispersion remains linear along the whole line ΓA except at the nearest vicinity of the BZ boundary (point A in Fig. 3.3 and point Γ for highest energy bands).

ii. Inter-band resonance in one of the arrays: the point \mathbf{q} lies on a high symmetry line of only one array. This case is illustrated by the lines ΓX_1 and X_1W in Fig. 3.3. Dispersion curves corresponding to quasi momenta lying at the line $q_2 = 0$, $0 \leq q_1 \leq Q/2$ (line ΓX_1 in Fig. 3.3) and the BZ boundary $q_1 = Q/2$, $0 \leq q_2 \leq Q/2$ (line X_1W in Fig. 3.3) are displayed in the central parts in Fig. 3.3). The characteristic feature of these lines is the intra-band degeneracy in one of two arrays. Indeed, in zero approximation, two modes $(2, s)$, $s = 2, 3$, propagating along the second array with a quasimomentum lying in the line ΓX_1 are degenerate with unperturbed frequency $\omega = 1$. The interaction lifts the degeneracy. This interaction appears to be repulsive. As a result, the lowest of the two

middle curves in Fig. 3.3 corresponds to $(2, u)$ boson, and the upper among them describes $(2, g)$ boson. Here the indices g, u denote a boson parity with respect to the transposition of the band numbers. Note that the $(2, g)$ boson exactly conserves its unperturbed frequency $\omega = 1$. The latter fact is related to the square symmetry of the QCB.

Other curves correspond to almost non perturbed bosons of the first array. The lowest two curves describe the dispersion of the $(1, 1)$ and $(1, 2)$ waves. Plasmons in the third band $(1, 3)$ are described by the uppermost curve in the figure. Their dispersion laws are nearly linear, and deviations from linearity are observed only near the boundary of the BZ (point X_1 in Fig. 3.3) and near the point Γ for the highest bands.

Similarly, in zero approximation, two modes $(1, s)$, $s = 1, 2$ ($3, 4$), propagating along the first array with a quasimomentum lying in the line X_1W are degenerate with unperturbed frequency $\omega = 0.5$ (1.5). The interaction lifts the degeneracy. As a result, the lowest of two middle (highest) curves in Fig. 3.3 corresponds to $(2, u)$ boson, and the upper of them describes $(2, g)$ boson. As in the previous case, $(2, g)$ boson exactly conserves its unperturbed frequency $\omega = 0.5$ (1.5).

Other curves correspond to almost non perturbed bosons of the second array. The lowest curve describes the dispersion of the $(2, 1)$ wave. The two middle curves describe the dispersion of $(2, 2)$ and $(2, 3)$ plasmons. Their dispersion laws are nearly linear, and deviations from linearity are observed only near the corner of the BZ (point W in Fig. 3.3) as well as in the vicinity of the point X_1 of the BZ.

iii Inter-band resonance in both arrays: the point X_1 (X_2) is a crossing point of the two high symmetry lines away from all resonant lines. This case is illustrated by the points X_1 and X_2 in Fig. 3.3. Consider for example point X_1 . Here $q_1 = Q/2$, $Q_2 = 0$. In zero approximation, two modes $(1, s)$, $s = 1, 2$ ($s = 3, 4$), propagating along the first array are degenerate with unperturbed frequency $\omega = 0.5$ ($\omega = 1.5$). The lower (higher) two lines correspond to even $(1, g)$ and odd $(1, u)$ superpositions of the 1-st array states of the first and second (third and fourth) bands. Similarly, two modes $(2, s)$ with $s = 2, 3$ are degenerate in zero approximation with unperturbed frequency $\omega = 1$. Therefore the middle two lines describe the same superpositions of the 2-d array states from the second and third bands.

iv. Inter-array resonance: The point \mathbf{q} lies only on one of the resonant lines away from the high symmetry lines. This case is illustrated by the diagonal ΓW of BZ. Consider now dispersion relations of modes with quasi-momenta on the diagonal ΓW of BZ and start with \mathbf{q} not too close to the BZ corner W ($q_1 = q_2 = Q/2$) and the Γ point. This diagonal is actually one of the resonance lines. Two modes in the first band corresponding to different arrays are strongly mixed. They mostly have a definite j -parity with respect to transposition of array numbers $j = 1, 2$. Interaction between these modes appears to be attractive (repulsive) for $q_1q_2 > 0$ ($q_1q_2 < 0$). Therefore the odd modes (u, s) , at the BZ

diagonal ΓW $s = 1, 2$, correspond to lower frequencies and the even modes (g, s) correspond to higher ones. The corresponding dispersion curves are displayed in the right part of Fig. 3.3.

v. Inter-array and inter-band resonance: The point q lies at the cross of two resonant lines. There are two points, the BZ corner W and the BZ center Γ in Fig. 3.3. At the BZ corner $q_1 = q_2 = Q/2$ (point W in Fig. 3.3) all four initial modes $j = 1, 2$ and $s = 1, 2$ ($s = 3, 4$) are degenerate in the lowest approximation. This four-fold degeneracy results from the square symmetry of BZ (the resonant lines are diagonals of the BZ). Weak inter-array interaction partially lifts the degeneracy. However, the split modes have a definite s -parity with respect to transposition of band numbers $s = 1, 2$ ($s = 3, 4$). The highest frequency corresponds mostly to (g, u) boson, symmetric with respect to transposition of array numbers, but antisymmetric with respect to the transposition of band numbers. The lower curve describes a (u, u) boson with both j -parity and s -parity odd. The two middle modes with even band parity, (g, g) and (u, g) bosons, remain degenerate and their frequencies conserve the unperturbed value $\omega = 0.5$ ($\omega = 1.5$). This also results from the square symmetry of QCB (3.4).

Similar behavior is observed in the BZ center Γ . All four initial modes $j = 1, 2$ and $s = 2, 3$ are degenerate in the lowest approximation. Weak inter-array interaction partially lifts the degeneracy. The highest frequency corresponds mostly to (g, u) boson, the lower curve describes a (u, u) boson, and the two middle bosons, (g, g) and (u, g) , remain degenerate and their frequencies conserve the unperturbed value $\omega = 1$.

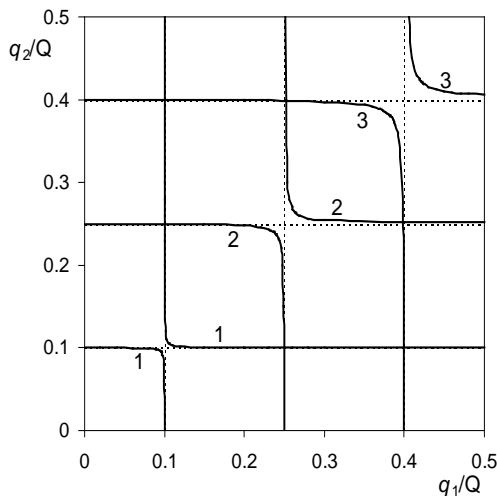


Figure 3.4: Lines of equal frequency of the lowest mode for QCB (solid lines) and for non-interacting arrays (dashed lines). The lines 1, 2, 3 correspond to the frequencies $\omega_1 = 0.1$, $\omega_2 = 0.25$, $\omega_3 = 0.4$.

All these results show that the quantum states of the $2D$ QCB conserve the quasi $1D$ character of the Luttinger-like liquid in major part of momentum space, and that $2D$ effects can be successfully calculated within the framework of perturbation theory. However, bosons

with quasimomenta close to the resonant line (diagonal OC) of the BZ are strongly mixed bare $1D$ bosons. These excitations are essentially two-dimensional, and therefore the lines of equal energy in this part of the BZ are modified by the $2D$ interaction (see Fig. 3.4). It is clearly seen that deviations from linearity occur only in a small part of the BZ. The crossover from LL to FL behavior around isolated points of the BZ due to a single-particle hybridization (tunnelling) for Fermi excitations was noticed in Refs. [15, 27], where a mesh of horizontal and vertical stripes in superconducting cuprates was studied.

3.6 Correlations and Observables

The structure of the energy spectrum analyzed above predetermines optical and transport properties of QCB. We consider here three types of correlation functions manifesting dimensional crossover in QCB.

3.6.1 Optical Absorption

We start with ac conductivity

$$\sigma_{jj'}(\mathbf{q}, \omega) = \sigma'_{jj'}(\mathbf{q}, \omega) + i\sigma''_{jj'}(\mathbf{q}, \omega).$$

The real part $\sigma'_{jj'}(\mathbf{q}, \omega)$ determines an optical absorption. The spectral properties of ac conductivity are given by a current-current correlator

$$\sigma_{jj'}(\mathbf{q}, \omega) = \frac{1}{\omega} \int_0^{\infty} dt e^{i\omega t} \left\langle \left[J_{j1\mathbf{q}}(t), J_{j'1\mathbf{q}}^\dagger(0) \right] \right\rangle. \quad (3.19)$$

Here $J_{js\mathbf{q}} = \sqrt{2}vg\pi_{js\mathbf{q}}$ is a current operator for the j -th array (we restrict ourselves to the first band, for the sake of simplicity).

The current-current correlator for non-interacting wires is reduced to the conventional LL expression [1],

$$\left\langle \left[J_{j1\mathbf{q}}(t), J_{j'1\mathbf{q}}^\dagger(0) \right] \right\rangle_0 = -2ivg\omega_{1\mathbf{q}} \sin(\omega_{1\mathbf{q}}t) \delta_{jj'}$$

with metallic-like peak

$$\sigma'_{jj'}(\mathbf{q}, \omega > 0) = \pi v g \delta(\omega - \omega_{1\mathbf{q}}) \delta_{jj'}. \quad (3.20)$$

For QCB this correlator is calculated in Appendix B. Its analysis leads to the following results. The longitudinal absorption

$$\sigma'_{11}(\mathbf{q}, \omega) \propto (1 - \phi_{1\mathbf{q}}^2) \delta(\omega - \tilde{\omega}_{1\mathbf{q}}) + \phi_{1\mathbf{q}}^2 \delta(\omega - \tilde{\omega}_{2\mathbf{q}})$$

contains well pronounced peak on the modified first array frequency and weak peak at the second array frequency (the parameter $\phi_{1\mathbf{q}} = \sqrt{\varepsilon}\zeta_1(q_1)\zeta_1(q_2)\omega_1(q_1)\omega_1(q_2)$ is small). The modified frequencies $\tilde{\omega}_{1\mathbf{q}}$ and $\tilde{\omega}_{2\mathbf{q}}$ coincide with the eigenfrequencies $\omega_{+1\mathbf{q}}$ and $\omega_{-2\mathbf{q}}$ respectively, if $\omega_{1\mathbf{q}} > \omega_{2\mathbf{q}}$. In the opposite case the signs $+, -$ should be changed to the opposite ones.

The transverse absorption component contains two weak peaks

$$\sigma'_{12}(\mathbf{q}, \omega) \propto \phi_{1\mathbf{q}} [\delta(\omega - \tilde{\omega}_{1\mathbf{q}}) + \delta(\omega - \tilde{\omega}_{2\mathbf{q}})].$$

At the resonant line, the results are drastically modified. Both longitudinal and transverse components of the optical absorption contain two well pronounced peaks corresponding to slightly split modified frequencies

$$\sigma'_{11}(\mathbf{q}, \omega) \propto \frac{1}{2} [\delta(\omega - \tilde{\omega}_{1\mathbf{q}}) + \delta(\omega - \tilde{\omega}_{2\mathbf{q}})].$$

3.6.2 Space Perturbation

One of the main effects specific for QCB is the appearance of non-zero transverse momentum–momentum correlation function. In space-time coordinates (\mathbf{x}, t) its representation reads,

$$G_{12}(\mathbf{x}; t) = i \langle [\pi_1(x_1, 0; t), \pi_2(0, x_2; 0)] \rangle, \quad \mathbf{x} = (x_1, x_2).$$

This function describes the momentum response at the point $(0, x_2)$ of the second array for

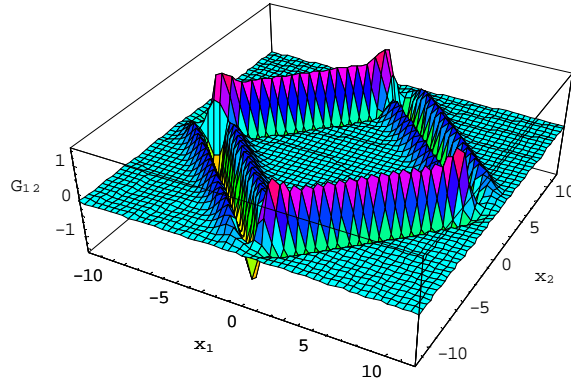


Figure 3.5: The transverse correlation function $G_{12}(x_1, x_2; t)$ for $r_0 = 1$ and $vt = 10$.

time t caused by an initial ($t = 0$) perturbation localized in coordinate space at the point $(x_1, 0)$ of the first array. Standard calculations similar to those described above, lead to the following expression,

$$G_{12}(\mathbf{x}; t) = \frac{V_0 r_0^2}{4\pi^2 \hbar} \int_{-\infty}^{\infty} dk_1 dk_2 \phi_1(k_1) \phi_2(k_2) k_1 k_2 \sin(k_1 x_1) \sin(k_2 x_2) \frac{v k_2 \sin(v k_2 t) - v k_1 \sin(v k_1 t)}{v^2 (k_2^2 - k_1^2)},$$

where $\phi_j(k)$ is the form-factor (3.12) written in the extended BZ. This correlator is shown in Fig. 3.5. It is mostly localized at the line determined by the obvious kinematic condition

$|x_1| + |x_2| = vt$ (“horizon of events”). The time t in the r.h.s. is the total time of plasmon propagation from the starting point $(x_1, 0)$ to the final point $(0, x_2)$ or vice versa, along any of the shortest ways compatible with a restricted geometry of the $2D$ grid. The finiteness of the interaction radius slightly spreads this peak and modifies its profile.

3.6.3 Rabi Oscillations

Further manifestation of the 2D character of QCB system is related to the possibility of periodic energy transfer between the two arrays. Consider an initial perturbation which excites a plane wave with amplitude θ_0 within the first array in the system of *non*-interacting arrays,

$$\theta_1(x_1, n_2 a; t) = \theta_0 \sin(q_1 x_1 + q_2 n_2 a - v|q_1|t).$$

If the wave vector \mathbf{q} , satisfying the condition $|\mathbf{q}| \ll Q/2$, is not close to the resonant line of the BZ, weak inter-array interaction ϕ (3.8) slightly changes the θ_1 component and leads to the appearance of a small $\theta_2 \sim \phi$ component. But for \mathbf{q} lying on the resonant line ($v|q_1| = v|q_2| \equiv \omega_{\mathbf{q}}$), both components within the main approximation have the same order of magnitude,

$$\begin{aligned} \theta_1(x_1, n_2 a; t) &= \theta_0 \cos\left(\frac{1}{2}\phi_{1\mathbf{q}}\omega_{\mathbf{q}}t\right) \sin(q_1 x_1 + q_2 n_2 a - \omega_{\mathbf{q}}t), \\ \theta_2(n_1 a, x_2; t) &= \theta_0 \sin\left(\frac{1}{2}\phi_{1\mathbf{q}}\omega_{\mathbf{q}}t\right) \cos(q_1 n_1 a + q_2 x_2 - \omega_{\mathbf{q}}t). \end{aligned}$$

This corresponds to 2D propagation of a plane wave with wave vector \mathbf{q} , *modulated* by a

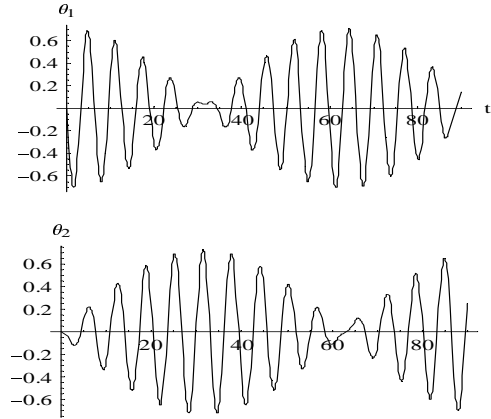


Figure 3.6: Periodic energy exchange between arrays (Rabi oscillations).

“slow” frequency $\sim \phi\omega$. As a result, beating arises due to periodic energy transfer from one array to another during a long period $T \sim (\phi\omega)^{-1}$ (see Fig. 3.6). These peculiar “Rabi oscillations” may be considered as one of the fingerprints of the physics exposed in QCB systems. Similar periodic energy transfer between three arrays can be observed in triple QCB (see Section D.3 of Appendix D).

3.7 Conclusions

We discussed in this Chapter the kinematics and dynamics of plasmon spectrum in QCB. These nanostructures may be fabricated from single-wall carbon nanotubes [9, 6]. On the one hand, QCB is promised to become an important component of future molecular electronics [9, 12]. On the other hand, the spectrum of elementary excitations (plasmons) in these grids possesses the features of both $1D$ and $2D$ electron liquid. As is shown in Refs. [21, 23] and confirmed in the present study, the energy spectrum of QCB preserves the characteristic properties of LL at $|\mathbf{q}|, \omega \rightarrow 0$. At finite \mathbf{q}, ω the density and momentum waves in QCB may have either $1D$ or $2D$ character depending on the direction of the wave vector. Due to inter-array interaction, unperturbed states, propagating along arrays are always mixed, and transverse components of correlation functions do not vanish. For quasi-momentum lying on the resonant lines of the BZ, such mixing is strong and transverse correlators have the same order of magnitude as the longitudinal ones. Periodic energy transfer between arrays (“Rabi oscillations”) is predicted.

The crossover from $1D$ to $2D$ regime may be experimentally observed. One of the experimental manifestations, i.e. the crossover from isotropic to anisotropic (spatially nonuniform) conductivity was pointed out in Ref. [23]. The current may be inserted in QCB at a point on an array j and extracted from another array i at a distance r . Then a temperature dependent length scale $l(T)$ arises, so that for $r \gg l$ the resistance is dominated by small q and therefore, the current is isotropic. In the opposite limit $r < l$ the dependence of the current on the points of injection/extraction may be detected. At $T = 0$ the length l becomes infinite, and current can only be carried along the wires. These effects are in fact manifestations of the LL behavior of the QCB in the infrared limit.

To observe the crossover at finite $\{\omega, \mathbf{q}\}$, one should find a way of exciting the corresponding plasmon modes. Then, scanning the $\omega(q_1, q_2)$ surfaces, one may in principle detect the crossover from quasi $1D$ to $2D$ behavior in accordance with the properties of the energy spectra presented in Section 3.5 and Appendices C and D. Plasmons in QCB may be excited either by means of microwave resonators or by means of interaction with surface plasmons. In the latter case one should prepare the grid on a corresponding semiconductor substrate and measure, e.g., the plasmon loss spectra. The theory of these plasmon losses will be presented in Chapter 5.

Chapter 4

Infrared Spectroscopy of Quantum Crossbars

4.1 Introduction

In this Chapter we consider various possibilities of direct observation of plasmon spectra at high frequencies and wave vectors by the methods of infrared (IR) spectroscopy. The QCB plasmons can be treated as a set of dipoles distributed within QCB constituents. In a single wire, the density of the dipole momenta is proportional to the LL boson field $\theta(x)$ (x is the coordinate along the wire). Few sets of coupled $1D$ dipoles form a unique system which possesses the properties of $1D$ and $2D$ liquid depending on the type of experimental probe. Some possibilities of observation of $1D \rightarrow 2D$ crossover in transport measurements were discussed in Ref. [16].

In transport measurements, the geometric factors regulate the crossover from anisotropic to isotropic resistivity of QCB: one may study the dc response for a field applied either parallel to one of the constituent arrays or in arbitrary direction. One may also study spatially nonuniform response by means of two probes inserted at different points of QCB and regulate the length scale, i.e., the distance between the two probes in comparison with the periods of the crossbar superlattice. These methods give information about the nearest vicinity of LL fixed point at $(\mathbf{q}, \omega, T) \rightarrow 0$.

Several crossover effects such as appearance of non-zero transverse space correlators and periodic energy transfer between arrays ("Rabi oscillations") were discussed in the previous Chapter. Unlike transport measurements, the methods of infrared spectroscopy provide an effective tool for investigating the excitation spectrum in a rather wide (\mathbf{q}, ω) area well beyond the sliding phase region [61]. We will show that the IR spectroscopy allows scanning of the $2D$ Brillouin zone in various directions and thereby elucidates dimensional crossover in the high symmetry points of the BZ.

The direct manifestation of dimensional crossover is through the response to an external ac electromagnetic field [60, 61, 62]. To estimate this response one should note that the two main parameters characterizing the plasmon spectrum in QCB are the Fermi velocity v of electrons in a wire and the QCB period a (we assume both periods to be equal). These parameters define both the typical QCB plasmon wave numbers $q = |\mathbf{q}| \sim Q = 2\pi/a$ and the typical plasmon frequencies $\omega \sim \omega_Q = vQ$. Choosing according to Refs. [9, 18] $v \approx 0.8 \cdot 10^6$ m/sec and $a \approx 20$ nm, one finds that characteristic plasmon frequencies lie in the far infrared region $\omega \sim 10^{14}$ sec $^{-1}$, while characteristic wave vectors are estimated as $q \sim 10^6$ cm $^{-1}$.

Here we study high frequency properties of the simplest double square QCB (generalization to more complicated geometries is straightforward). We start from QCB interacting with an external infrared radiation. The plasmon velocity v is much smaller than the light velocity c and the light wave vector k is three orders of magnitude smaller than the characteristic plasmon wave vector Q corresponding to the same frequency. Therefore, infrared radiation incident directly on an *isolated* array, can not excite plasmons at all (it could excite plasmon with $\omega \neq 0$). However in QCB geometry, each array serves as a diffraction lattice for its partner, giving rise to Umklapp processes of wave vectors nQ , n integer. As a result, excitation of plasmons in the BZ center $q = 0$ with frequencies nvQ occurs.

To excite QCB plasmons with $q \neq 0$ one may use an additional diffraction lattice (DL) with period $A > a$ coplanar to the QCB. Here the diffraction field contains space harmonics with wave vectors $2\pi M/A$, M integer, that enables one to scan plasmon spectrum within the BZ. Dimensional crossover manifests itself in the appearance of additional absorption lines when the wave vector of the diffraction field is oriented along specific directions. In the general case one observes the single absorption lines forming two sets of equidistant series. Instead of that, in the main resonance direction (QCB diagonal) an equidistant series of split doublets can be observed. In the case of higher resonance direction, absorption lines form an alternating series of singlets and split doublets demonstrating new type of dimensional crossover related to the frequency change with direction fixed.

The structure of the present Chapter is as follows: In Sections 4.2 and 4.3 we study interaction of QCB with an external field. In Section 4.2 we consider the case when the incident infrared radiation falls directly on the QCB. In Section 4.3 we study possible scanning of QCB spectrum with the help of an external DL. In the Conclusions we summarize the results obtained.

4.2 Long Wave Absorption

In the case of a dielectric substrate transparent in the infrared region, one can treat QCB as an isolated grid (without substrate) interacting directly with the incident radiation. Consider the simplest geometry where an external wave falls normally onto QCB plane, and its electrical field

$$\mathbf{E} = E_0 \mathbf{e}_1 \cos(\mathbf{k}\mathbf{r} - \omega t)$$

is parallel to the lower (first) array (see Fig. 4.1 for details). In this geometry the field \mathbf{E} is *longitudinal* for array 1 and *transverse* for the array 2. The eigenfrequencies of transverse modes in array 2 substantially exceed the IR frequency of the incident wave and even the standard LL ultraviolet cutoff frequency. Thus, the incident wave can be treated as a static polarization field for this array, and the factor $\cos \omega t$ can be omitted. Then, the polarization waves in array 2 form a longitudinal diffraction field for array 1 with quasi wave vectors nQ (n integer). Further, the characteristic order of magnitude Q of a QCB plasmon wave vector is much larger than the wave vector \mathbf{k} of the incident light, so one can assume the latter to be equal to zero from the very beginning. Then, the light wavelength is much larger than a nanotube diameter and the geometrical shadow effect can be neglected. As a result the total field which affects array 1 consists of an external field and a diffraction field produced by a static charge induced in array 2.

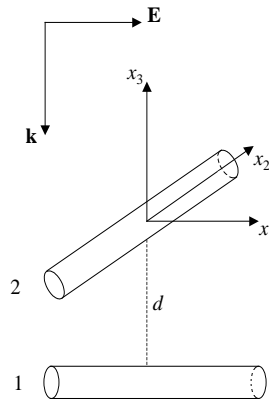


Figure 4.1: The incident field orientation with respect to QCB. The axes x_1 and x_2 are directed along the corresponding arrays, and d is the inter-array vertical distance (along the x_3 axis).

To calculate the diffraction field, we consider first the field \mathbf{E}^0 produced by the quantum wire of array 2 which is located at $x_1 = x_3 = 0$ and labelled by $n_1 = 0$. The large distance between the wire under consideration and its neighbor partners from the same array allows us to neglect the influence of the charges induced on them. The static potential on the surface of the wire includes external potential of an incident field and the potential Φ^0 of the charge induced on the wire. On the other hand, this static potential should be equal to a constant which we choose to be zero. In cylindrical coordinates $r, \vartheta, x_2, x_1 = r \cos \vartheta, x_3 = r \sin \vartheta$, this

condition reads

$$\Phi^0(R_0, \vartheta, x_2) = E_0 r_0 \cos \vartheta. \quad (4.1)$$

Outside the wire, the induced potential Φ^0 satisfies the Laplace equation $\Delta\Phi^0 = 0$. Solving this equation with boundary condition (4.1) we obtain the static part of the induced potential

$$\Phi^0(r, \vartheta, x_2) = \frac{E_0 r_0^2}{r} \cos \vartheta$$

and the corresponding static part of the induced field along the x_1 direction,

$$E_1^0(x_1, x_3) = -E_0 \frac{r_0^2 (x_3^2 - x_1^2)}{(x_3^2 + x_1^2)^2}.$$

The first component of the diffraction field is the sum of the fields induced by all wires of the upper array,

$$E_1(x_1; t) = \cos \omega t \sum_{n_1} E_1^0(x_1 - n_1 a, -d) = -E_0 \cos \omega t \sum_{n_1} \frac{r_0^2 (d^2 - (x_1 - n_1 a)^2)}{(d^2 + (x_1 - n_1 a)^2)^2}. \quad (4.2)$$

This field is a periodic function of x_1 with a period a . Therefore, its Fourier expansion contains only wave vectors $k_{1n} = nQ$ (n is the order of diffraction). This means that only frequencies $\omega_n = nvQ$ can be excited. In this case it is more convenient to expand the field over Bloch eigenfunctions of an ‘‘empty’’ wire [58]. These functions are labelled by quasimomentum q_1 , $|q_1| \leq Q/2$, and the band number s . The expansion includes only $q_1 = 0$ components and has the form

$$E_1(x_1; t) = \cos \omega t \sum_s E_{[s/2]} u_s(x_1),$$

where $u_s(x)$ is the $q_1 = 0^+$ Bloch amplitude $u_{sq_1}(x)$ (A.2) within the s -th band and

$$E_n = -E_0 \frac{\pi r_0^2}{ad} nQ d e^{-nQd}. \quad (4.3)$$

The excited eigenfrequency $\omega_n = \omega_{[s/2]}$ belongs simultaneously to the top of the lower even band with number $s = 2n$ and to the bottom of the upper odd band with number $s = 2n + 1$ (this is the result of $\mathbf{E}(x) = \mathbf{E}(-x)$ parity). The incident field cannot excite plasmons at all and we do not take it into account.

Turning to the (\mathbf{q}, s) representation with the help of the expansion

$$\theta_1(x_1, n_2 a) = \frac{\sqrt{a}}{L} \sum_{\mathbf{sq}} \theta_{1s\mathbf{q}} e^{i(q_1 x_1 + q_2 n_2 a)} u_{sq_1}(x), \quad (4.4)$$

and similarly for θ_2 and $\pi_{1,2}$, one easily sees that only the $\mathbf{q} = \mathbf{0}$ components are involved in the interaction of plasmons with the incident radiation.

Consider an initial frequency ω close to ω_n . In a resonant approximation, only four equations of motion for the “coordinate” operators θ_s with $s = 2n, 2n + 1$ are relevant

$$\begin{aligned}
\ddot{\theta}_{1,2n} + \omega_n^2 \theta_{1,2n} + \phi \omega_n^2 (\theta_{2,2n} - \theta_{2,2n+1}) &= L f_n \cos \omega t, \\
\ddot{\theta}_{1,2n+1} + \omega_n^2 \theta_{1,2n+1} - \phi \omega_n^2 (\theta_{2,2n} - \theta_{2,2n+1}) &= L f_n \cos \omega t, \\
\ddot{\theta}_{2,2n} + \omega_n^2 \theta_{2,2n} + \phi \omega_n^2 (\theta_{1,2n} - \theta_{1,2n+1}) &= 0, \\
\ddot{\theta}_{2,2n+1} + \omega_n^2 \theta_{2,2n+1} - \phi \omega_n^2 (\theta_{1,2n} - \theta_{1,2n+1}) &= 0,
\end{aligned} \tag{4.5}$$

where

$$f_n = \frac{\sqrt{2} v g e}{\hbar \sqrt{a}} E_n,$$

and we assume that $\zeta_s(q_{1,2})$ (3.12) is equal to 1 for the first few bands.

The homogeneous part of this system defines four eigenfrequencies: $\omega_{g,g} = \omega_{u,g} = \omega_n$, $\omega_{g/u,u} \approx \omega_n(1 \pm \phi)$. The corresponding eigenvectors are symmetrized combinations of the four operators which enter Eq.(4.5). They have a fixed parity with respect to permutation of arrays (the first index) and neighboring bands (the second index). Only two modes (even with respect to band index)

$$\theta_{g/u,g} = \frac{1}{2} (\theta_{1,2n} + \theta_{1,2n+1} \pm \theta_{2,2n} \pm \theta_{2,2n+1}),$$

interact with an external field. Therefore only the unperturbed frequency $\omega_n = \omega_{gg} = \omega_{ug}$ will be absorbed. The two equations of motion for the operators $\theta_{gg,ug}$ have the same form

$$\ddot{\theta}_\alpha + 2\gamma \dot{\theta}_\alpha + \omega_n^2 \theta_\alpha = L f_n \cos \omega t,$$

where $\alpha = gg, ug$. Employing standard procedure in the vicinity of the resonance $|\omega - \omega_n| \ll \omega_n$ immediately yields the relative absorption of the Lorentz type

$$\frac{\Delta I_n}{I_0} = 2g \frac{e^2}{\hbar c} \left(\frac{\pi r_0^2}{ad} \right)^2 \frac{\gamma v Q}{(\omega - \omega_n)^2 + \gamma^2} [n Q d e^{-n Q d}]^2, \tag{4.6}$$

where

$$I_0 = \frac{c L^2}{4\pi} E_0^2$$

is the intensity of light that falls on the QCB.

Due to the exponential term in the r.h.s of Eq.(4.3), E_n decreases fast with n and only the first few terms contribute to absorption. The characteristic dimensionless scale of the induced field $r_0^2/(ad)$ for typical values of QCB parameters equals 0.004. We tabulate below the lowest dimensionless Fourier components of the induced field.

n	1	2	3	4	5
$-\frac{ad E_n}{r_0^2 E_0}$	1.05306	1.12359	0.89914	0.63957	0.42650

The results show that one can hope to probe at least the first five spectral lines corresponding to ω_n with $n = 1, 2, \dots, 5$.

The width of the absorption line (4.6) is governed by an attenuation coefficient γ . We introduce it phenomenologically, but one can (at least qualitatively) estimate its value. The attenuation is caused by decay of plasmon into phonons. The one phonon decay of the plasmon with wave number k and frequency $\omega = v|k|$ into a single phonon with the same ω and k occurs at a single point in $1D$ and does not yield finite attenuation at all. Multi-phonon decay is weak because of the small anharmonic coupling within the wire. As a result, the form of the absorption lines should be determined mainly by the instrumental line-width.

4.3 Scanning of the QCB Spectrum within the BZ

Within a geometry considered in the previous subsection, one can probe plasmon spectrum only at the BZ center. To study plasmons with nonzero wave vectors one should add to the system an external diffraction lattice (DL), namely, a periodic array of metallic stripes parallel to the Y axis (see Fig. 4.2). The DL plane $Z = 0$ is parallel to the QCB planes $Z = -D$ for the upper second array and $Z = -(D + d)$ for the lower first array (the Z axis is parallel to the x_3 axis). The distance D between DL and second array is of the same order as the inter-array distance $d = 2$ nm. The angle between the DL wires and the *second* array is φ ($0 < \varphi < \pi/2$). To get a wave number K of a diffraction field much smaller than Q one needs a DL with a period A much larger than the QCB period a . In the following numerical estimations we choose $A \approx 200$ nm.

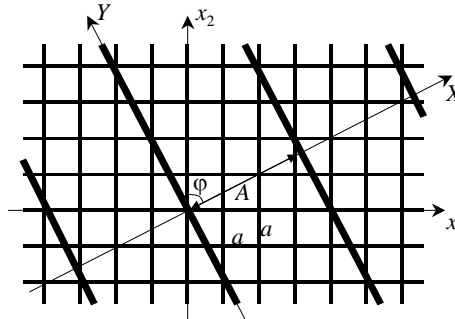


Figure 4.2: QCB and DL. The X, Y axes are oriented along the DL stripes and the wave vector \mathbf{K} of the diffraction field respectively. The DL (QCB) period is A (a).

Consider an incident field with electric vector $\mathbf{E} = E_0 \mathbf{e}_X \cos(\mathbf{k}\mathbf{r} - \omega t)$ oriented along the X axis (perpendicular to the DL wires). The radius R_0 of a DL wire is assumed to be not much larger than the nanotube radius r_0 . In this case, light scattering on the DL is similar to that considered in subsection 4.2. Then the diffraction field is concentrated along the X

direction and has the form (compare with Eq.(4.2))

$$E_X(X, Z, t) = -E_0 \cos \omega t \sum_N \frac{R_0^2(Z^2 - (X - NA)^2)}{(Z^2 + (X - NA)^2)^2}.$$

The Fourier transform of the diffraction field is

$$E_X(\mathbf{K}, Z) = -E_0 \frac{\pi R_0^2}{A|Z|} |KZ| e^{-|KZ|},$$

where $\mathbf{K}(M) = K \mathbf{e}_X = K(\sin \varphi, \cos \varphi) = (K_1, K_2)$, with $K = 2\pi M/A$, M being a positive integer. This means that all the points \mathbf{K} lie on the same ray oriented along the positive direction of the X axis. The vector $\mathbf{K}(M)$ for a fixed M can be uniquely represented as a sum of quasimomenta lying in the first BZ and two reciprocal lattice vectors

$$\mathbf{K}(M) = \mathbf{q}(M) + \mathbf{m}_1(M) + \mathbf{m}_2(M).$$

The field components

$$E_{1\mathbf{K}} = E_X(\mathbf{K}, D + d) \sin \varphi, \quad E_{2\mathbf{K}} = E_X(\mathbf{K}, D) \cos \varphi \quad (4.7)$$

parallel to the quantum wires, can excite plasmons and contribute to the absorption process.

The Hamiltonian describing the interaction of QCB with an external field reads,

$$H_E = \frac{\hbar L}{2vg} \sum_{\mathbf{K}} \left[f_{1,\mathbf{K}} \left(\theta_{1,\mathbf{K}} + \theta_{1,\mathbf{K}}^\dagger \right) + f_{2,\mathbf{K}} \left(\theta_{2,\mathbf{K}} + \theta_{2,\mathbf{K}}^\dagger \right) \right], \quad (4.8)$$

where

$$f_{j,\mathbf{K}} = \frac{\sqrt{2}vge}{\hbar\sqrt{a}} E_{j,\mathbf{K}}, \quad \mathbf{m} = \mathbf{m}_1 + \mathbf{m}_2. \quad (4.9)$$

In this Section we are interested not in the form of the absorption line but only in the resonant frequencies. Therefore, we do not introduce any phenomenological attenuation. The equations of motion for boson fields have the form

$$\begin{aligned} \ddot{\theta}_{1,\mathbf{q}+\mathbf{m}_1} + \omega_{q_1+m_1Q}^2 \theta_{1,\mathbf{q}+\mathbf{m}_1} + \phi \sum_{m_2} \Phi_{\mathbf{q}+\mathbf{m}} \theta_{2,\mathbf{q}+\mathbf{m}_2} &= L \sum_{M,m_2} f_{1,\mathbf{K}} \delta_{\mathbf{K},\mathbf{q}+\mathbf{m}}, \\ \ddot{\theta}_{2,\mathbf{q}+\mathbf{m}_2} + \omega_{q_2+m_2Q}^2 \theta_{2,\mathbf{q}+\mathbf{m}_2} + \phi \sum_{m_1} \Phi_{\mathbf{q}+\mathbf{m}} \theta_{1,\mathbf{q}+\mathbf{m}_1} &= L \sum_{M,m_1} f_{2,\mathbf{K}} \delta_{\mathbf{K},\mathbf{q}+\mathbf{m}}, \end{aligned} \quad (4.10)$$

where ϕ is the dimensionless coupling strength (3.8), $\Phi_{\mathbf{k}}$ is given by Eq. (3.9).

Only the first few terms in the sum over K in the r.h.s. of Eq. (4.10) really excite the QCB plasmons. Indeed, the diffraction field (4.4) is proportional to the same dimensionless function of the type te^{-t} ($t = |KZ_j|$) as in the previous subsection (see Eq.(4.3)). This function has its maximum at $t = 1$ and differs significantly from zero for $0.2 < t < 2.7$. For $a = 20$ nm, $D = 2$ nm, it is of order unity within the interval $0.18Q < |K| < 2.13Q$ for the

first array ($Z_1 = D + d$), and within the interval $0.36Q < |K| < 4.26Q$ for the second array ($Z_1 = D$). This means that one can excite the modes of the four lower bands ($K < 2Q$) of the first array and the modes of eighth lower bands ($K < 4Q$) of the second array.

According to Eqs. (4.7) the field $E_{j\mathbf{K}(M)}$ is coupled with plasmons of wave vectors $\mathbf{q} + \mathbf{m}_j = \mathbf{q}(M) + \mathbf{m}_j(M)$ within the j -th array. The nature of the excited plasmons as well as their frequencies depend on the direction of the vector $\mathbf{K}(M)$. For simplicity we restrict ourselves by acute angles $0 < \varphi < \pi/2$ describing orientation of both the DL and the vector $\mathbf{K}(M)$. There are four kinds of dimensional crossover events depending on the specific directions in the BZ. Each type of crossover is characterized by its own set of absorption lines. The first one takes place in a common case when $\mathbf{K}(M)$ for any M never reaches neither a resonant direction nor the BZ boundary. The second case corresponds to the bisectorial direction $\varphi = \pi/4$ where the main resonant condition $\omega(K_1) = \omega(K_2)$ is fulfilled. The third set of directions is determined by another resonant condition $\omega(K_1) = \omega(nQ \mp K_2)$. Finally, the fourth set is formed by directions intersecting with the BZ boundaries for some values of M . In what follows we consider these four cases separately.

1. In the general case, the points $\mathbf{K}(M)$ for all M are far from the BZ diagonals and boundaries. Therefore each of them corresponds to a couple of plasmons mostly propagating along the j -th array, $j = 1, 2$, with unperturbed frequencies $\omega_{K_j(M)} = vK_j(M)$. The inter-array interaction slightly renormalizes the eigenfrequencies

$$\omega_{1\mathbf{K}}^2 = \omega_{K_1}^2 + \phi^2 \sum_{m_2} \frac{\omega_{K_1}^2 \omega_{K_2+m_2Q}^2}{\omega_{K_1}^2 - \omega_{K_2+m_2Q}^2}, \quad \omega_{2\mathbf{K}}^2 = \omega_{K_2}^2 + \phi^2 \sum_{m_1} \frac{\omega_{K_2}^2 \omega_{K_1+m_1Q}^2}{\omega_{K_2}^2 - \omega_{K_1+m_1Q}^2}.$$

Thus, increasing the frequency of an incident light one observes a set of single absorption lines that consists of two almost equidistant subsets with frequencies corresponding to excitation of plasmons in the first or second arrays. The frequency spacing between adjacent lines within each subset are

$$\Delta\omega_1 = v\Delta K_1 = 2\pi v \sin \varphi / A, \quad \Delta\omega_2 = v\Delta K_2 = 2\pi v \cos \varphi / A,$$

and their ratio depends only on the DL orientation φ

$$\frac{\Delta\omega_1}{\Delta\omega_2} = \tan \varphi.$$

2. In the resonant case $\varphi = \pi/4$, the relation $K_1(M) = K_2(M)$ is satisfied for all M . Therefore modes propagating along the two arrays are always degenerate. Inter-array interaction lifts the degeneracy. Indeed, in the resonant approximation, the coupled equations of motion for the field operators read

$$\ddot{\theta}_{1\mathbf{K}} + \omega_{K_1}^2 \theta_{1\mathbf{K}} + \phi \omega_{K_1}^2 \theta_{2\mathbf{K}} = f_{1\mathbf{K}}, \quad \ddot{\theta}_{2\mathbf{K}} + \omega_{K_1}^2 \theta_{2\mathbf{K}} + \phi \omega_{K_1}^2 \theta_{1\mathbf{K}} = f_{2\mathbf{K}}.$$

After symmetrization $\theta_{g,u} = (\theta_{1\mathbf{K}} \pm \theta_{2\mathbf{K}})/\sqrt{2}$, they have the same form

$$\ddot{\theta}_\alpha + \omega_\alpha^2 \theta_\alpha = f_\alpha,$$

where $\omega_{g/u} = \omega_K \sqrt{1 \pm \phi}$ are the renormalized frequencies, $f_{g/u} = (f_{1\mathbf{K}} \pm f_{2\mathbf{K}})/\sqrt{2}$, and $\alpha = g, u$. The amplitudes $f_{g,u}$ are of the same order of magnitude because the distances D and d are different but have the same order of magnitude. As a result, increasing the frequency of an incident light one observes an equidistant set of absorption doublets with distance $\pi\sqrt{2}v/A$ between adjacent doublets.

3. Consider now the directions φ determined by the equation

$$\sin\left(\varphi \pm \frac{\pi}{4}\right) = \frac{nA}{\sqrt{2}M_0a},$$

where n and M_0 are mutually prime integers. For this direction, two components of the first $M_0 - 1$ points $\mathbf{K}(M)$ do not satisfy any resonant condition while the M_0 -th one does

$$K_1(M_0) \pm K_2(M_0) = nQ. \quad (4.11)$$

With increasing M this situation is reproduced periodically so that all the points $\mathbf{K}(pM_0)$ with p integer satisfy a similar condition with pn standing instead of n , while all intermediate points are out of resonance.

In zero order approximation with respect to the inter-array interaction we expect to observe two set of absorption lines with frequencies $p\omega_j = vK_j(pM_0)$, $j = 1, 2$, corresponding to excitation of plasmons within the $pm_j(M_0)$ -th band of the j -th array. The ratio of the frequencies ω_j is defined by the DL orientation

$$\frac{\omega_1}{\omega_2} = \tan \varphi.$$

However, due to the resonance condition (4.11), a plasmon in the first array with wave vector $K_1(pM_0)$ and frequency $\omega_1 = vK_1(pM_0)$ is coupled with a plasmon in the second array with the same frequency and wave vector $K'_2 = \mp(npQ - K_1(pM_0))$ (inter-array degeneracy). Similarly, a plasmon in the second array with wave vector $K_2(pM_0)$ and frequency $\omega_2 = vK_2(pM_0)$ is coupled with a plasmon in the first array with the same frequency and wave vector $K'_1 = npQ \mp K_2(pM_0)$. This degeneracy of two modes corresponding to the same band but to different arrays is lifted by the inter-array interaction. As a result one has two sets of doublets instead of two sets of single lines.

Thus, for such orientation of the DL, increasing the frequency of an incident wave one should observe two equidistant sets of single absorption lines with two sets of equidistant doublets built in these series

$$\omega_{1\mathbf{K}} = \omega_{K_1(pM_0)} \left(1 \pm \frac{1}{2}\phi\right), \quad \omega_{2\mathbf{K}} = \omega_{K_2(pM_0)} \left(1 \pm \frac{1}{2}\phi\right).$$

In the case $n = 1$ the lower doublet lies in the first energy band, whereas the upper one lies in the second band. For $A/a = 10$ (that corresponds to the realistic values of the parameters $a = 20$ nm and $A = 200$ nm) the lowest doublet ($p = 1$) will be observed for

example for integer $M_0 = 8$, at the angle $\varphi(8) \approx 17^\circ$, around frequencies $\omega_1(8) = 0.76vQ$, $\omega_2(8) = 0.24vQ$.

4. A similar behavior will be manifested in the case when the points \mathbf{K}_{pM} lie at one of the BZ boundaries, i.e., they satisfy the relation

$$K_j(pM_j) = \frac{npQ}{2}$$

with some specific values j , M_j and n . Such situation is realized at specific angles that depend on the integers j, n, M_j . In the vicinity of the points $\mathbf{K}(pM_j)$ two frequencies corresponding to the unperturbed modes of the j -th array from the np -th and $(np + 1)$ -th bands coincide. This is the case of inter-band degeneracy that is also lifted by inter-array interaction. Due to the square symmetry (invariance with respect to $x_j \rightarrow -x_j$ inversion), only one of the two components with frequency $\omega = v|K_j(pM_j)|$ may be excited by a diffraction field. Therefore, this case is not distinct from case **1** considered above and two sets of equidistant single lines can be observed.

We emphasize that by studying absorption of light by QCB one can expose, beyond the studied above [58] dimensional crossover with respect to an angle (direction), also the occurrence of a new type of crossover with *an external frequency* as a control parameter. This occurs for special directions of type **3** where, with increasing frequency, the set of single lines is periodically intermitted by doublets.

4.4 Conclusions

In conclusion, we investigated the possibility of spectroscopic studies of the excitation spectrum of quantum crossbars, which possesses unique property of dimensional crossover both in spatial coordinates and in (\mathbf{q}, ω) coordinates. It follows from our studies that the plasmon excitations in QCB may be involved in resonance diffraction of incident electromagnetic waves and in optical absorption in the IR part of spectrum.

In the case of direct interaction of external electric field with QCB, infrared absorption strongly depends on the direction of the wave vector \mathbf{q} . One can observe dimensional crossover from $1D \rightarrow 2D$ behavior of QCB by scanning an incident angle. The crossover manifests itself in the appearance of a set of absorption doublets instead of the set of single lines. At special directions, one can observe new type of crossover where doublets replace the single lines with changing frequency at a fixed \mathbf{q} direction.

Dimensional crossover in QCB plays a significant role in all the above phenomena.

Chapter 5

Landau Damping in a $2D$ Electron Gas with Imposed Quantum Grid

5.1 Introduction

In this Chapter, QCB interaction with semiconductor substrate is studied. Any surface wave excited in the substrate is coupled with QCB-plasmon modes due to the substrate-QCB interaction. This interaction might be strong enough compared with the frequency spacing of surface waves and QCB plasmons because surface plasmon waves exist in the same frequency and wave vector area as plasmons in QCB (see subsection 5.2.2 for details). Therefore by exciting the substrate plasmons one can probe the QCB characteristics [61, 62, 63]. Indeed, substrate-QCB interaction substantially changes the conventional picture of substrate dielectric losses. Due to such interaction, new regions of Landau damping appear. The existence of these regions themselves, as well as their structure and the density of losses are sensitive both to the QCB period a and the direction of the wave vector \mathbf{k} of the initial wave. Thus, dielectric losses in QCB-substrate system serve as a good tool for studying QCB spectral properties.

The structure of this Chapter is as follows. In Section 5.2, we briefly describe double square QCB interacting with the dielectric substrate and introduce the necessary definitions. Dielectric properties of the system considered are studied in Section 5.3, where Dyson-type equations for the polarization operator are obtained and analyzed. The detailed description of new regions of Landau damping is presented in Section 5.4. In the Conclusion Section we summarize the results obtained.

5.2 Quantum Crossbars on Semiconductor Substrate

Let us consider a square QCB on a semiconductor substrate (see Fig. 5.1). We choose coordinate system so that **1**) the axes x_j and the corresponding basic unit vectors \mathbf{e}_j are oriented along the j -th array ($j = 1, 2$); **2**) the x_3 axis is perpendicular to the QCB plane; **3**) the x_3 coordinate is zero for the second array, $-d$ for the first one, and $-(d + D)$ for the substrate. The basic vectors of the reciprocal superlattice for a square QCB are $Q\mathbf{e}_{1,2}$, $Q = 2\pi/a$ so that an arbitrary reciprocal superlattice vector \mathbf{m} is a sum $\mathbf{m} = \mathbf{m}_1 + \mathbf{m}_2$, where $\mathbf{m}_j = m_j Q\mathbf{e}_j$ (m_j integer). An arbitrary vector $\mathbf{k} = k_1\mathbf{e}_1 + k_2\mathbf{e}_2$ of reciprocal space can be written as $\mathbf{q} + \mathbf{m}$ where \mathbf{q} belongs to the first BZ $|q_{1,2}| \leq Q/2$.

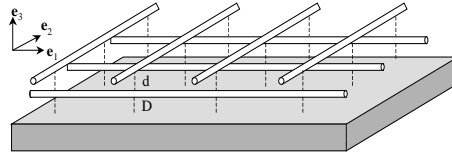


Figure 5.1: QCB on a substrate. \mathbf{e}_μ ($\mu = 1, 2, 3$) are basic vectors of the coordinate system. The vector \mathbf{e}_1 (\mathbf{e}_2) is oriented along the first (second) array. The inter-array distance is d and the distance between the substrate and the first (lower) array is D .

5.2.1 Substrate Characteristics

The substrate is described by the Hamiltonian

$$H_s = H_K + H_C, \quad (5.1)$$

where

$$H_K = \sum_{\mathbf{q}\mathbf{m}} \varepsilon_{\mathbf{q}+\mathbf{m}} c_{\mathbf{q}+\mathbf{m}}^\dagger c_{\mathbf{q}+\mathbf{m}}, \quad \varepsilon_{\mathbf{k}} = \frac{\hbar^2 k^2}{2m},$$

is a kinetic energy of the substrate electrons with effective mass m and quadratic dispersion law (we omit the irrelevant spin variables), and

$$H_C = \frac{1}{2} \sum_{\mathbf{q}\mathbf{m}} U_{\mathbf{q}+\mathbf{m}} \rho_{\mathbf{q}+\mathbf{m}}^\dagger \rho_{\mathbf{q}+\mathbf{m}}, \quad \rho_{\mathbf{k}} = \frac{1}{L} \sum_{\mathbf{k}'} c_{\mathbf{k}'}^\dagger c_{\mathbf{k}+\mathbf{k}'}, \quad U_{\mathbf{k}} = \frac{2\pi e^2}{k}, \quad \mathbf{k} = \mathbf{q} + \mathbf{m},$$

is Coulomb interaction within the substrate.

Dielectric properties of the substrate *per se* are described by its dielectric function $\varepsilon_s(\mathbf{k}, \omega)$,

$$\frac{1}{\varepsilon_s(\mathbf{k}, \omega)} = 1 + U_{\mathbf{k}} \Pi_s(\mathbf{k}, \omega). \quad (5.2)$$

Within the RPA approach, the polarization operator $\Pi_s(\mathbf{k}, \omega)$ is approximated by the Lindhard expression

$$(\Pi_s(\mathbf{k}, \omega))^{-1} = (\Pi_0(\mathbf{k}, \omega))^{-1} - U_{\mathbf{k}}, \quad (5.3)$$

with

$$\Pi_0(\mathbf{k}, \omega) = \frac{1}{L^2} \sum_{\mathbf{k}'} \frac{\vartheta(\varepsilon_F - \varepsilon_{\mathbf{k}'}) - \vartheta(\varepsilon_F - \varepsilon_{\mathbf{k}+\mathbf{k}'})}{\hbar\omega - (\varepsilon_{\mathbf{k}+\mathbf{k}'} - \varepsilon_{\mathbf{k}'}) + i0} \quad (5.4)$$

at $T = 0$.

Active branches of substrate excitations are the surface density fluctuations which consist of 2D electron-hole pair continuum and surface plasmon mode with dispersion law [64]

$$\omega_s(\mathbf{k}) = v_F k \sqrt{1 + \frac{1}{2kr_B}}, \quad r_B = \frac{\hbar^2}{me^2}, \quad k = |\mathbf{k}|.$$

The RPA spectrum of surface excitations is shown in Fig. 5.2.

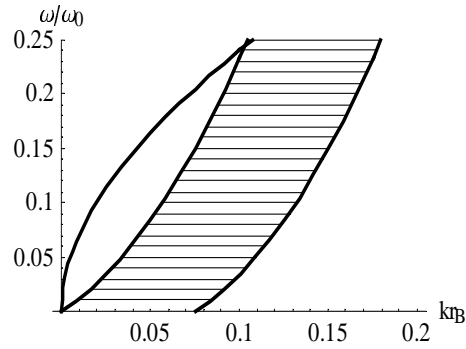


Figure 5.2: Dispersion of the substrate plasmons (upper line) and quasi-continuum spectrum of electron-hole excitations, (dashed area). Frequency is measured in $\omega_0 = v_F/r_B$ units.

In the case of GaAs, the substrate parameters are $m = 0.068m_0$, m_0 is the free electron mass, $v_F = 8.2 \cdot 10^6$ cm/sec, $r_B = 0.78$ nm, $\omega_0 = v_F/r_B = 1.05 \times 10^{14}$ sec $^{-1}$. For $k < k^* \approx 0.104r_B^{-1}$, the plasmon frequency lies above the continuum spectrum of electron-hole pairs and the substrate plasmons are stable. Besides, one may easily satisfy the resonance condition for the collective plasmon mode near the stability threshold $k \sim k^*$ and QCB excitations with frequency $\omega \sim \omega^* = 2.6 \cdot 10^{13}$ sec $^{-1}$. For large enough $k > k^*$ the plasmon dispersion curve lies within the quasi-continuum spectrum and plasmons become unstable with respect to decay into electron-hole pairs (Landau damping of the substrate plasmons). Dielectric losses of an isolated substrate are described by an imaginary part $\Im\epsilon_s(\mathbf{k}, \omega)$ of its dielectric function (5.2). This imaginary part is non-zero within the dashed region in Fig. 5.2 due to the appearance of an imaginary part

$$\Im\Pi_0(\mathbf{k}, \omega) = \frac{m}{2\pi\hbar^2} \frac{1}{\kappa^2} \left[\vartheta(\kappa^2 - \nu_+^2) \sqrt{\kappa^2 - \nu_+^2} - \vartheta(\kappa^2 - \nu_-^2) \sqrt{\kappa^2 - \nu_-^2} \right],$$

$$\kappa = \frac{k}{k_F}, \quad \nu_{\pm} = \nu \pm \kappa^2/2, \quad \nu = \frac{\omega}{v_F k_F}$$

of the bare polarization operator $\Pi_0(\mathbf{k}, \omega)$ (5.4).

5.2.2 Interaction

Interaction between QCB and the substrate is a capacitive coupling of charge fluctuations in the substrate with collective modes in the quantum wires. Assuming the distance D between the first array and the substrate to be much smaller than the distance d between arrays, one can keep only the interaction H_{s1} between the substrate and the first array. The interaction between the substrate density fluctuation at the point $\mathbf{r} \equiv (x_1, x_2)$ and the density fluctuations located in the vicinity of the point x'_1 which belongs to the n_2 -th wire of the first array is described by its amplitude $W(x_1 - x'_1, x_2 - n_2a)$, where

$$W(\mathbf{r}) = \frac{\sqrt{2}e^2\zeta(x_1/r_0)}{\sqrt{|\mathbf{r}|^2 + D^2}}.$$

The function $\zeta(x_1/r_0)$ in the numerator describes the screening of Coulomb interaction within a wire or nanotube [46]. In the momentum representation the interaction Hamiltonian between substrate and array has the form:

$$H_{s1} = \sqrt{\frac{\hbar}{vg}} \sum_{\mathbf{m}\mathbf{q}} W_{\mathbf{q}+\mathbf{m}} \rho_{\mathbf{q}+\mathbf{m}} \theta_{1,\mathbf{q}+\mathbf{m}}^\dagger, \quad (5.5)$$

where

$$W_{\mathbf{k}} = ik_1 \sqrt{\frac{vg}{\hbar a}} \int d\mathbf{r} W(\mathbf{r}) e^{i\mathbf{k}\mathbf{r}} \quad (5.6)$$

is proportional to the Fourier component of the interaction amplitude $W(\mathbf{r})$.

Finally, the Hamiltonian of QCB interacting with a semiconductor substrate is the sum of Hamiltonians (3.7), (5.1) and (5.5),

$$H = H_{QCB} + H_s + H_{s1}. \quad (5.7)$$

5.3 Dielectric Function

High frequency properties of the system at zero temperature are determined by zeroes of its dielectric function

$$\frac{1}{\epsilon(\mathbf{k}, \omega)} = 1 + U_{\mathbf{k}} \Pi(\mathbf{k}, \omega). \quad (5.8)$$

Here

$$\Pi(\mathbf{k}, \omega) = -\frac{i}{\hbar} \int_0^\infty dt e^{i\omega t} \left\langle \left[\rho_{\mathbf{k}}(t), \rho_{\mathbf{k}}^\dagger(0) \right] \right\rangle,$$

is the polarization of the *substrate interacting with QCB*, $\rho_{\mathbf{k}}(t) = e^{iHt/\hbar} \rho_{\mathbf{k}} e^{-iHt/\hbar}$ is the density of the *substrate* electrons in the Heisenberg representation, and averaging is performed over the ground state of the Hamiltonian (5.7).

The Umklapp processes stimulated by the interaction between the substrate and the first array (5.5) as well as the interaction between arrays (2.27), produce modes with wave vectors $\mathbf{q} + \mathbf{m}$ with various inverse lattice vectors \mathbf{m} . This necessarily leads to appearance of non-diagonal polarization operators

$$\Pi(\mathbf{q} + \mathbf{m}, \mathbf{q} + \mathbf{m}'; \omega) = -\frac{i}{\hbar} \int_0^{\infty} dt e^{i\omega t} \langle [\rho_{\mathbf{q}+\mathbf{m}}(t) \rho_{\mathbf{q}+\mathbf{m}'}^{\dagger}(0)] \rangle.$$

In what follows we always consider a fixed frequency ω and a fixed wave vector \mathbf{q} from the BZ. So the variables \mathbf{q} and ω are omitted below for simplicity. In the framework of RPA approach, $\Pi(\mathbf{m}, \mathbf{m}')$ satisfies the Dyson-type equation

$$\Pi(\mathbf{m}, \mathbf{m}') = \Pi_s(\mathbf{m}) \delta_{\mathbf{m}, \mathbf{m}'} + \Pi_s(\mathbf{m}) W_{\mathbf{m}} \Xi_1(m_1, \mathbf{m}'). \quad (5.9)$$

The first term $\Pi_s(\mathbf{m})$ in the right hand side is the substrate polarization (5.3) of the isolated substrate itself, $W_{\mathbf{m}} \equiv W_{\mathbf{q}+\mathbf{m}}$ is a bare vertex (5.6) which describes substrate - (first) array interaction, and

$$\Xi_j(m_j, \mathbf{m}') = -\frac{i}{\hbar} \int_0^{\infty} dt e^{i\omega t} \langle [\theta_{j, \mathbf{q}+\mathbf{m}_j}(t), \rho_{\mathbf{q}+\mathbf{m}'}^{\dagger}(0)] \rangle \quad (5.10)$$

is the correlation function of the j -th array mode and the substrate plasmon.

The Dyson equation (5.9) should be completed by two equations for the correlation functions (5.10) ($j = 1, 2$)

$$\Xi_1(m_1, \mathbf{m}') = D_1^0(m_1) \sum_{m_2} W_{\mathbf{m}} \Pi(\mathbf{m}, \mathbf{m}') + D_1^0(m_1) \sum_{m_2} \Phi_{\mathbf{m}} \Xi_2(m_2, \mathbf{m}'), \quad (5.11)$$

$$\Xi_2(m_2, \mathbf{m}') = D_2^0(m_2) \sum_{m_1} \Phi_{\mathbf{m}} \Xi_1(m_1, \mathbf{m}'). \quad (5.12)$$

Here $D_j^0(m_j)$ ($j = 1, 2$) is the bare correlation function of the j -th array modes

$$D_j^0(m_j) = -\frac{i}{vg} \int_0^{\infty} dt e^{i\omega t} \langle [\theta_{j, \mathbf{q}+\mathbf{m}_j}(t), \theta_{j, \mathbf{q}+\mathbf{m}_j}^{\dagger}(0)] \rangle_0 = \frac{1}{\omega^2 - v^2(q_j + m_j)^2},$$

and another bare vertex $\Phi_{\mathbf{m}}$ describes the separable inter-array interaction (3.9).

Solving the system of equations (5.9), (5.11) and (5.12) one obtains the diagonal element $\Pi(\mathbf{m}) \equiv \Pi(\mathbf{m}, \mathbf{m})$ of the polarization operator

$$[\Pi(\mathbf{m})]^{-1} = [\Pi_s(\mathbf{m})]^{-1} - |W_{\mathbf{m}}|^2 D(\mathbf{m}). \quad (5.13)$$

The second term on the right-hand side of this equation describes renormalization of the substrate polarization operator $\Pi_s(\mathbf{m})$ by interaction between the substrate and QCB. The factor $D(\mathbf{m})$ is a renormalized correlation function of modes of the first array

$$[D(\mathbf{m})]^{-1} = [D_1^0(m_1)]^{-1} - (w(\mathbf{m}) + \varphi(m_1)). \quad (5.14)$$

The first term $w(\mathbf{m})$ describes the effective interaction between the first array and the substrate

$$w(\mathbf{m}) = F(m_1) - |W_{\mathbf{m}}|^2 \Pi_s(\mathbf{m}), \quad F(m_1) = \sum_{m_2} |W_{\mathbf{m}}|^2 \Pi_s(\mathbf{m}). \quad (5.15)$$

The second one $\varphi(m_1)$ is the effective interaction between arrays

$$\frac{\omega_{m_1}^2}{\varphi(m_1)} = \left[\phi^2 \sum_{m_2} \omega_{m_2}^2 D_2^0(m_2) \right]^{-1} - \Psi_{m_1}, \quad \omega_{m_j} = v|q_j + m_j Q|, \quad (5.16)$$

renormalized by Coulomb interaction of array modes with the substrate plasmons,

$$\Psi_{m_1} = \sum_{m'_1 \neq m_1} \frac{\omega_{m'_1}^2}{(D_1^0(m'_1))^{-1} - F(m'_1)}. \quad (5.17)$$

Equations (5.13) - (5.17) together with definition (5.8) solve the problem of elucidation of the dielectric properties of the combined system QCB-substrate.

The spectrum of collective excitations in QCB-substrate system is determined by zeros of the dielectric function $\epsilon(\mathbf{q}, \omega) = 0$. The key question here is the robustness of the QCB spectrum against interaction with $2D$ substrate excitations. Detailed analysis shows that in the long wave limit $q \ll Q$ the interaction just renormalizes the bare dispersion laws of the arrays, conserving its LL linearity. This result verifies stability of QCB plasmons with respect to substrate-QCB interaction.

The QCB-substrate interaction also results in occurrence of some special lines in the BZ. These lines correspond to resonant interaction of the substrate with the first or the second array. The resonance condition $\omega_s(\mathbf{k}) = \omega_j(\mathbf{k})$ is fulfilled along the line $LJIN$ for $j = 1$ and along the line KBM for $j = 2$ in Fig. 5.4, right panel, below.

5.4 Landau Damping

As was mentioned in subsection 5.2.1 above, dielectric losses of an isolated substrate are related to the Landau damping due to decay of substrate plasmons with momentum $k > k^* \approx 0.104r_B^{-1}$ into electron-hole pairs. The substrate-QCB interaction remarkably modifies the conventional picture of substrate plasmon dielectric losses. Due to QCB-substrate interaction, new domains of Landau damping appear in addition to the dashed region in Fig. 5.2. Indeed, outside the initial instability region where $\Im \epsilon_s(\mathbf{k}, \omega) = 0$, nonzero imaginary part $\Im \epsilon(\mathbf{k}, \omega)$ (5.8) exists if the imaginary part of the bare polarization operator $\Im \Pi_0(\mathbf{k} + \mathbf{m}, \omega)$ differs from zero at least for one of the reciprocal lattice vectors \mathbf{m} . The main contribution to $\Im \epsilon(\mathbf{k}, \omega)$ is related to the renormalization term $w(\mathbf{m})$ in Eq.(5.15) due to Umklapp processes along the x_2 axis (summation over m_2 in the expression for the function $F(m_1)$ is implied).

It is proportional to the fourth power of QCB - substrate interaction W^4 . The Umklapp processes along both directions $x_{1,2}$ contribute also to the renormalization term $\varphi(m_1)$ in Eq.(5.16). However, they contain an additional small parameter ϕ^4 related to inter-array interaction within QCB. These terms are not taken into account. Thus, the possible Umklapp vectors have the form $\mathbf{m}_2 = m_2 Q \mathbf{e}_2$, $m_2 = \pm 1, \pm 2, \dots$ and in what follows we will label them by an integer number m_2 .

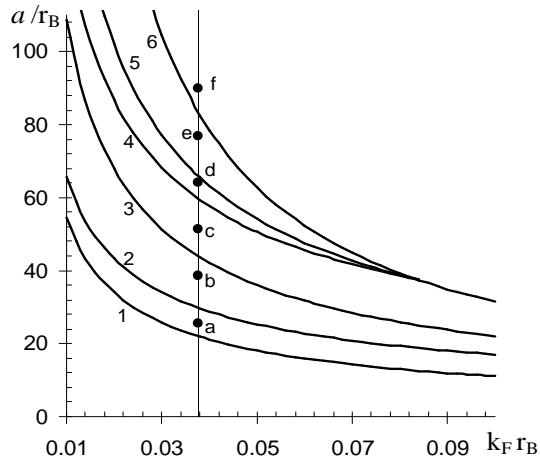


Figure 5.3: Phase diagram describing appearance and structure of new regions of Landau damping. Lines 1–6 separate different types of new damping regions. Points a – f correspond to the structures displayed below in Figs. 5.4-5.6.

The structure of the new Landau damping regions and their existence themselves is governed by interplay between the Fermi momentum of the substrate k_F and the QCB period a . The first of these parameters defines the width of the two-particle excitation band (dashed region in Fig. 5.2) while the second determines the minimal reciprocal vector Q . In the case of sufficiently thick QCB superlattice (small a) and sufficiently low electron density within the substrate (small k_F), Umklapp processes are always ineffective because they change an initial plasmon wave-vector into the outer part of the instability region. This means that only plasmons with momenta $|k| > k^*$ decay into electron-hole pairs.

Increasing the QCB period or the Fermi momentum turn the Umklapp processes effective, and additional Landau damping regions appear within the circle $|k| \leq k^*$. The first factors involved are the smallest Umklapp vectors ± 1 , then new damping regions appear corresponding to the Umklapp vectors ± 2 and so on. As a result one gets a rich variety of possible damping scenarios. We describe them with the help of a “phase diagram” in the $a - k_F$ plane displayed in Fig. 5.3 (actually dimensionless coordinates a/r_B and $k_F r_B$ are used). Here the set of curves labelled by numbers 1 – 6 separate the regions of parameters corresponding to the different Umklapp vectors and different structures of the new damping regions. There is no additional Landau damping regions below the first line. Above the sixth line Landau damping takes place within the whole circle $k \leq k^*$. Above lines with numbers $2n - 1$, the Umklapp vector $\pm n$ becomes effective. The corresponding additional

damping region has the form of a tail touching the initial Landau damping region $|k| \geq k^*$. This tail turns to the additional damping band well separated from the initial one above the line number $2n$ ($n < 3$) within some sector of directions in k -space (in what follows, these directions will be labelled by corresponding arcs of the circle).

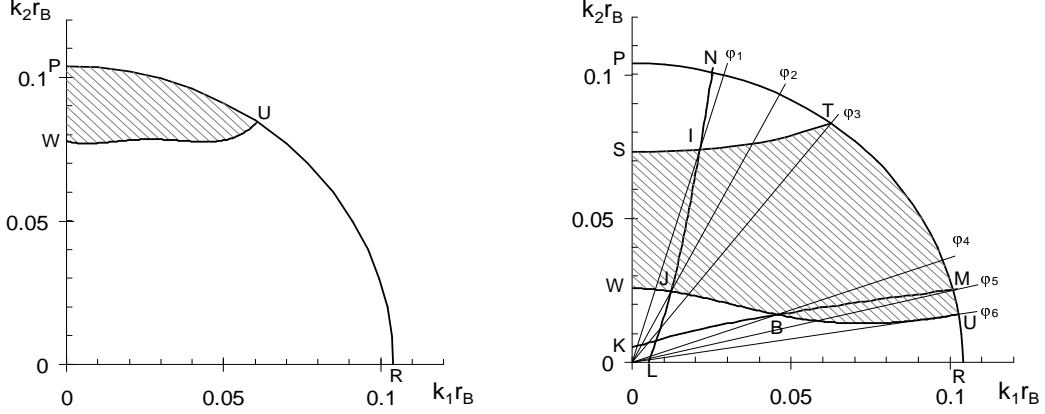


Figure 5.4: **Left panel:** New Landau damping region PUW for QCB with period $a = 20$ nm (point a in Fig. 5.3) corresponds to the Umklapp vector -1 . **Right panel:** New damping region $STUW$ for $a = 30$ nm (point b in Fig. 5.3) corresponds to the Umklapp vector -1 and describes Landau damping tail (within the arc TU) or separate landau band (within the arc TP). Other details of this figure are explained in the text.

Possible structures of new damping regions corresponding to some representative points $a - f$ in the $a - k_F$ plane (see Fig. 5.3) are displayed in detail in Figs. 5.4-5.6. All these figures correspond to the GaAs value of $k_F r_B \approx 0.038$. Generally speaking we should display new damping region within the whole circle $|k| \leq k^*$ in the plane k_1, k_2 . The circle center Γ is placed at the origin (we did not put the letter Γ in Figs. 5.4-5.6). But this region is always symmetric with respect to reflection $k_1 \rightarrow -k_1$ and with respect to the combined reflection $k_2 \rightarrow -k_2, m_2 \rightarrow -m_2$. This enables us to describe the damping scenarios only within the quarter $k_{1,2} \geq 0$ (complete picture of the new damping region can be easily obtained from the displayed one with the help of the reflection symmetries mentioned above).

Damping of the substrate plasmon occurs inside the arc PR in Figs. 5.4-5.6 when at least one of the points in the phase space with coordinates $(\mathbf{k} + \mathbf{m}_2, \omega_s(k))$ lies within the quasi-continuum spectrum of the electron-hole excitations, whereas the “mother” point $(\mathbf{k}, \omega_s(k))$ lies above the continuum (above the dashed area in Fig. 5.2). As was mentioned above, for small enough QCB period $a < a_1 = 17.3$ nm, the basic reciprocal lattice vector $Q\mathbf{e}_2$ is too large, the points $(\mathbf{k} + \mathbf{m}_2, \omega_s(k))$ lie outside the quasi-continuum for all m_2 and additional Landau damping region does not exist. It appears only for $a > a_1$ ($Q < 2k^* + 2k_F$). For $a_1 < a < a_2 = 23.6$ nm ($2k^* + 2k_F > Q > 2k^*$), this is the region PUW (see Fig. 5.4, left panel) corresponding to the $m_2 = -1$ (in all Figs. 5.4-5.6, the regions related to this Umklapp vector are always hatched by the hatching tilted to left). As a result, the damping tails touching the initial Landau damping region appear in certain directions of the \mathbf{k} plane.

For $a_2 < a < a_3 = 34.6$ nm ($2k^* > Q > k^* + k_F$), the new damping region is related to the same Umklapp vector -1 , but now it has a strip-like structure bounded by the line $STUW$ in Fig. 5.4, right panel. Note that the damping is absent within the region PTS . As a result, it is possible to divide the angular region $0 \leq \varphi \leq \pi/2$ into three sectors. Within the first one PT , $0 \leq \varphi \leq \varphi_3$, a new damping region is separated from the initial one. The second sector TU , $\varphi_3 \leq \varphi \leq \varphi_6$, corresponds to a new damping tail. Finally, within the third sector UR , $\varphi_6 \leq \varphi \leq \pi/2$, new damping region does not exist at all.

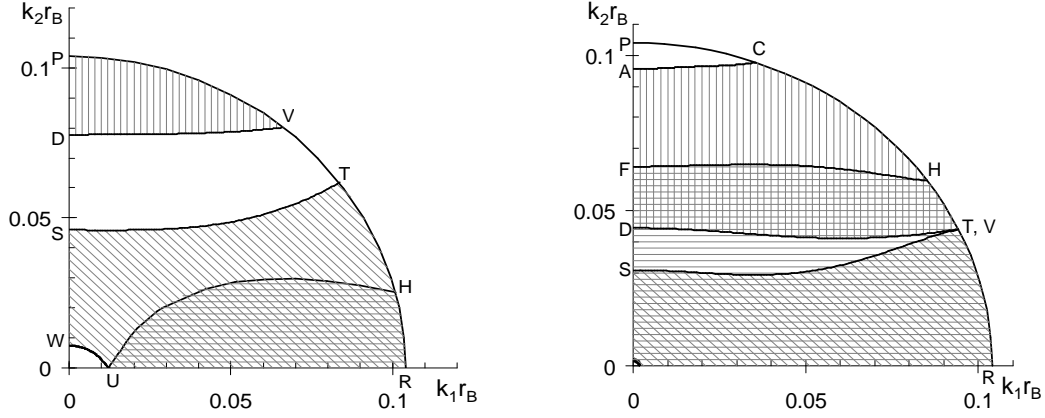


Figure 5.5: **Left panel:** In the case $a = 40$ nm (point c in Fig. 5.3), new Landau damping regions PVD , $STRUW$, and UHR correspond to the Umklapp vectors -2 , -1 , and $+1$. **Right panel:** New regions of Landau damping for $a = 50$ nm (point d in Fig. 5.3). Regions $ACVD$, STR , and FHR correspond to the Umklapp vectors -2 , -1 , and $+1$

For larger QCB period, $a_3 < a < a_4 = 47.1$ nm ($k^* + k_F > Q > k^*$), the new damping regions have a more complicated structure. In fact the damping area consists of three parts (see Fig. 5.5, left panel). The first one, $STRUW$ corresponds to the Umklapp vector -1 . Note that it is shifted to the bottom with respect to the previous case $a = 30$ nm. This part overlaps with the second part HUR . The latter corresponds to the Umklapp vector $+1$ and is hatched in Figs. 5.5-5.6 by horizontal hatching. The second region PVD corresponds to the Umklapp vector -2 (in Figs. 5.5-5.6 such a regions are always hatched by vertical hatching). As a result in the direction close enough to the k_2 axis, one gets a new damping tail with $m_2 = -2$) and well separated new damping band with Umklapp vector -1 .

Further increase of QCB period $a_4 < a < a_5 = 52.3$ nm, $k^* > Q > 2(k^* + k_F)/3$ ($k^* \approx 2.8k_F$ for GaAs) leads to further extension of new damping regions. The region $ADVC$ corresponding to the Umklapp vector -2 is partially separated from the initial damping region. It overlaps with the region $FHR\Gamma$ ($m_2 = +1$) which in its turn overlaps with the region $STR\Gamma$ ($m_2 = -1$). Actually the two latter regions do not include an extremely small vicinity of the origin Γ which is not shown in Fig. 5.5, right panel. Visible coincidence of the points V and T in Fig. 5.5, right panel is an artefact of the accuracy of the figure.

Within the next interval of QCB periods $a_5 < a < a_6 = 65.2$ nm ($2(k^* + k_F)/3 > Q > 2k_F$) new damping region GPE corresponding to the Umklapp vector -3 appears. This

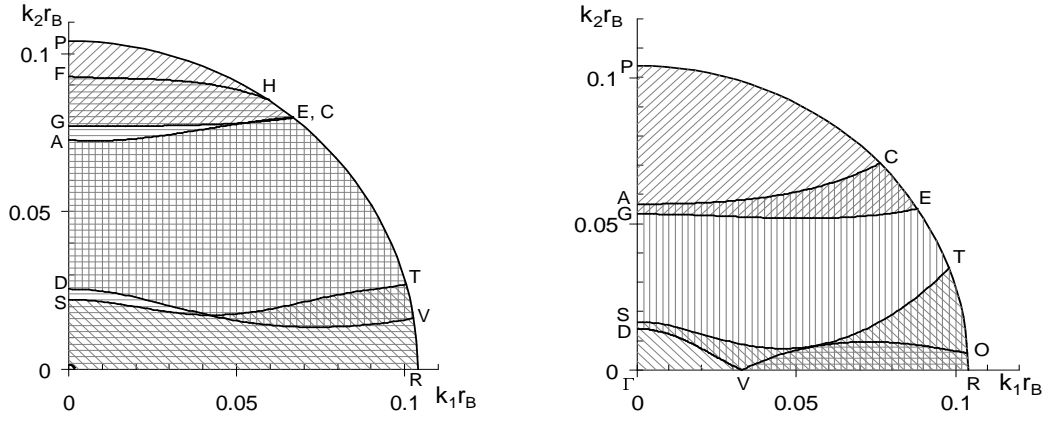


Figure 5.6: **Left panel:** New regions of Landau damping for $a = 60$ nm (point e in Fig. 5.3). Besides the regions $ACVD$, STR , and FHR corresponding, as in the case $a = 50$ nm, to the Umklapp vectors -2 , -1 , and $+1$, new Umklapp vector -3 appears (region PEG). **Right panel:** The case $a = 70$ nm (point f in Fig. 5.3). New regions of Landau damping PEG , $ACVD$, STR , whole sector ΓPR , and VOR correspond to the Umklapp vectors -3 , -2 , -1 , $+1$, and $+2$.

region is hatched in Figs. 5.6 by the hatching tilted to the right. Beside that, the regions $ADVC$ ($m_2 = -2$), $FHR\Gamma$ ($+1$), and $STR\Gamma$ (-1) are present. As in the previous figure, visible coincidence of the points E and C in Fig. 5.6, left panel is an artefact of the accuracy of the figure.

Finally for $a > a_6$ ($Q < 2k_F$), Landau damping emerges in the whole circle $|k| \leq k^*$. This occurs due to processes with Umklapp vector $+1$. The corresponding damping region covers the whole quarter. Therefore we did not hatch it at all, and used the same horizontal hatching for the new region VOR corresponding to the Umklapp vector $+2$. The region $DACRV$ is related to the Umklapp vector -2 . We emphasize that at the same time the vertex V of this region is the vertex of the region VOR . This is not an accidental approximate coincidence as in the two previous figures. The regions GPE and ΓSTR are related to the Umklapp vectors -3 and -1 respectively.

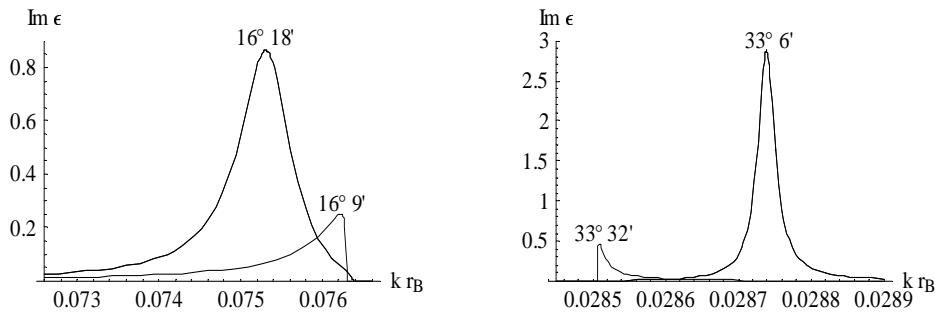


Figure 5.7: Damping tail for $\varphi \approx 16^\circ$ (left panel) and $\varphi \approx 33^\circ$ (right panel). Precursor of the resonant peak and the resonant peak are resolved quite well.

Thus, the general structure of the additional damping regions is described in Figs. 5.4-5.6. However, there is an additional structure of these regions. This fine structure is related

to possible resonance interaction between the substrate plasmons and the QCB plasmons of the first or second array. The resonance condition for the first (second) array is written as $\omega_s(\mathbf{k}) = \omega_1(\mathbf{k})$ ($\omega_s(\mathbf{k}) = \omega_2(\mathbf{k})$).

Consider such fine structure of new Landau damping region in details for QCB with period $a = 30$ nm. Here the resonance conditions are satisfied along the lines *LJIN* and *KBM* (see Fig. 5.4, right panel). These lines intersect with the damping region boundaries at the points *J, I, B* and *MB* which define four rays *OI, OJ, OB,* and *OU* and four corresponding angles $\varphi_1 \approx 16^\circ 11'$, $\varphi_2 \approx 33^\circ 19'$, $\varphi_4 \approx 69^\circ$, $\varphi_5 \approx 76^\circ$. The resonance interaction takes place within two sectors $\varphi_1 < \varphi < \varphi_2$ and $\varphi_4 < \varphi < \varphi_5$.

For each $\varphi < \varphi_1$ the new damping region is a well separated damping band. The damping amplitude is small because of the small factor of order W^4 mentioned above. When $\varphi \rightarrow \varphi_1 - 0$, small peak appears near the “blue” boundary of this damping region. This peak is a precursor of the resonance between the substrate plasmon and the first array QCB plasmon (Fig. 5.7, left panel). The same happens from the opposite side of the sector (φ_1, φ_2 when $\varphi \rightarrow \varphi_2 + 0$ (Fig. 5.7, right panel).

Within the sector $\varphi_1 < \varphi < \varphi_2$, the damping band contains a well pronounced peak corresponding to resonant interaction between the substrate plasmon and the first array plasmons (see Figs. 5.7). The peak amplitude is of order of the damping amplitude within the initial damping region. It has a Lorentz form placed on a wide and low pedestal. The peak is especially sensitive to the strength of the QCB-substrate interaction which is governed by the distance D between QCB and substrate.

To study this D dependence, let us consider the imaginary part $\Im\epsilon(\mathbf{k}, \omega)$ of the dielectric function within the considered sector $\varphi_1 < \varphi < \varphi_2$. In the vicinity of the plasmon frequency $\omega \approx \omega_s(k)$ this imaginary part is written as

$$\Im\epsilon(\mathbf{k}, \omega) = \frac{|W_{\mathbf{k}}|^2}{U_{\mathbf{k}}} \frac{-\Im w(\mathbf{k}, \omega_s(k))}{(\omega^2 - v^2 k_1^2)^2 + (\Im w(\mathbf{k}, \omega_s(k)))^2},$$

with $w(\mathbf{k}, \omega_s(k))$ being of order $|W_{\mathbf{k}}|^2$. So the resonance peak indeed has the Lorentz like shape with height of order unity,

$$\Im\epsilon_{max} \sim \frac{|W_{\mathbf{k}}|^2}{|W_{\mathbf{k}-Q\mathbf{e}_2}|^2} \sim 1,$$

whereas its half-width

$$\Gamma = \Im w(\mathbf{k}, v|k_1|) \sim |W_{\mathbf{k}-Q\mathbf{e}_2}|^2,$$

is of order W^2 . The peak is displayed in Fig. 5.8 for different values of the distance D between the substrate and the nearest (first) array. It is seen that the amplitude changes slowly with increasing distance D while its width squeezes sharply, $W^2 \sim 1/D^2$.

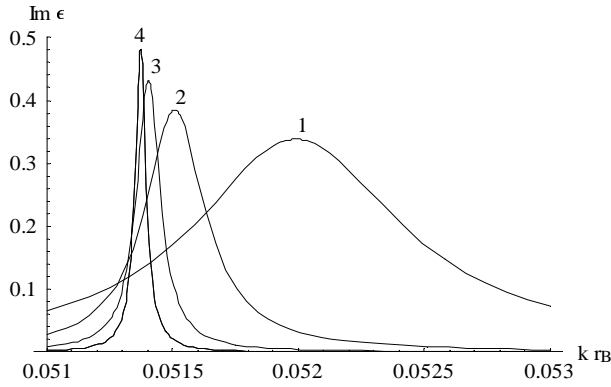


Figure 5.8: Damping tail for $\varphi = 20^\circ$ for different distances D between QCB and substrate. The curves **1**, **2**, **3**, and **4** correspond to $D = 1$ nm, 1.5 nm, 2 nm, and 2.5 nm, respectively. With increasing D , the resonant peak narrows and slowly increases, whereas the area under the curve decreases.

There is no resonance interaction within the sector $\varphi_2 < \varphi < \varphi_4$ but further increase of the angle $\varphi_4 < \varphi < \varphi_5$ leads to re-appearance of the resonant peak within the damping tail. In this case one deals with a resonance between the substrate plasmon and the QCB plasmon in the second array. Existence of this resonance is caused by inter-array interaction that brings additional small parameter to the imaginary part of the dielectric function. As a result, the width of the peak is much smaller in the second sector while surprisingly, the peak amplitude has the same order of magnitude as in the case of resonance with the first array (closest to the substrate).

Existence of the additional QCB bands (tails) of Landau damping and appearance of the resonant peaks within the bands (tails) is a clear manifestation of interplay between real $2D$ surface plasmons and quasi- $2D$ QCB plasmons.

5.5 Conclusions

In conclusion, the possibility of spectroscopic studies of the excitation spectrum of quantum crossbars interacting with semiconductor substrate is investigated. A capacitive contact between QCB and substrate does not destroy the LL character of the long wave excitations. However, the interaction between the surface plasmons and plasmon-like excitations of QCB essentially influences the dielectric properties of the substrate. The QCB may be treated as a diffraction grid for the substrate surface, and Umklapp diffraction processes radically change the plasmon dielectric losses. Due to QCB-substrate interaction, additional Landau damping regions of the substrate plasmons appear. The structure of these regions and the spectral density of dielectric losses are strongly sensitive to the QCB period. The surface plasmons are more fragile against interaction with superlattice of quantum wires than the LL plasmons against interaction with $2D$ electron gas in a substrate.

Chapter 6

Ultraviolet Probing of Quantum Crossbars

6.1 Introduction

The IR based methods mentioned above are not very convenient from two points of view. First, as it was mentioned, one needs an additional diffraction lattice to tune the light wave vector and that of the QCB plasmon. Second, they probe QCB spectrum only in some discrete points. The alternative method of studying QCB spectrum by *ultraviolet (UV) light scattering* is the subject of the present Chapter. The advantages of this method are evident. It does not require any additional diffraction lattice. It probes QCB spectrum in a continuous region of wave vectors. Finally, its selection rules differ from those for IR absorption. This gives rise to the observation of additional spectral lines not visible in IR experiments [65, 66].

In this Chapter we formulate the principles of UV spectroscopy for QCB and study the main characteristics of scattering spectra. The Chapter is organized as follows. In Section 6.2, we discuss light scattering on QCB and present basic equations describing this process. The main results of the Chapter are contained in subsection 6.2 where we classify the basic types of the scattering indicatrices (angular diagrams of differential cross section) corresponding to various detector orientations. The results obtained are summarized in the Conclusion Section. Technical details are concentrated in Appendix E. This Appendix is devoted derivations of an effective QCB-light interaction and the basic formula for differential cross section of light scattering.

6.2 Light Scattering on QCB

The simplest process contributing to the Raman-like light scattering is an annihilation of an incident photon and creation of a scattered photon together with a QCB plasmon (Fig.

6.1b). In terms of initial electrons, this is in fact the second order process. Since the energies of incident and scattered photons significantly exceed the electron excitation energy in nanotube, one may consider the emission/absorption process as an instantaneous act (see Appendix E). This process may be treated as the inelastic photon scattering accompanied by emission or absorption of a plasmon (Fig. 6.1c).

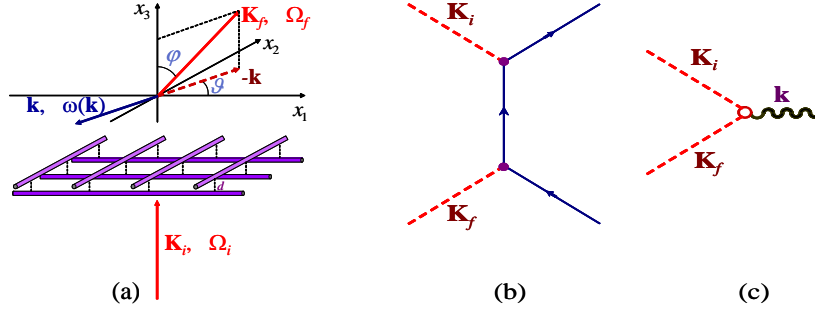


Figure 6.1: (a) The scattering process geometry (all notations are explained in the text). (b) Second order diagram describing light scattering on QCB. Solid lines correspond to fermions, whereas dashed lines are related to photons. The vertices are described by the interaction Hamiltonian (6.1). (c) Effective photon-plasmon vertex. QCB excitation is denoted by wavy line.

Let \mathbf{K}_i (\mathbf{K}_f) and $\Omega_i = cK_i \equiv c|\mathbf{K}_i|$, ($\Omega_f = cK_f$) be momentum and frequency of the incident (scattered) photon. For simplicity we restrict ourselves by the case of normal incidence $\mathbf{K}_i = (0, 0, K_i)$. Direction of the scattered wave vector is characterized by the unit vector $\mathbf{n}(\varphi, \vartheta)$, where φ and ϑ are polar and azimuthal angles of the spherical coordinate system with polar axis oriented in the \mathbf{e}_3 direction. The momentum of the excited QCB plasmon is \mathbf{k} , the projection of the scattered photon momentum onto QCB plane is $-\mathbf{k}$. This process is displayed in Fig. 6.1a. If the QCB plasmon frequency $\omega(\mathbf{Q})$ coincides with the photon frequency loss $\omega = \Omega_i - \Omega_f$, then a detector oriented in a scattered direction \mathbf{n} will register a sharp well pronounced peak at the frequency loss $\omega = \omega(\mathbf{k})$. The frequency loss is much smaller than the incident and scattered photon frequencies. Therefore in what follows we use the same notation K for both K_i and K_f where it is possible. Scanning the frequency loss ω , (or, that is the same, modulus of the scattered wave vector K_f) for a fixed detector orientation \mathbf{n} , two or more (up to six for a square QCB) such peaks can be observed. The number of peaks and their location strongly depend on the azimuthal angle ϑ in the QCB plane. Scanning this angle, one can change the number of observable peaks. This is yet another manifestation of dimensional crossover mentioned above.

An arbitrary vector $\mathbf{k} = (k_1, k_2)$ of reciprocal space can be written as $\mathbf{k} = \mathbf{q} + \mathbf{m}$, where $\mathbf{q} = (q_1, q_2)$ belongs to the first BZ. QCB eigenstates are classified by quasi-momentum \mathbf{q} and $2D$ band number. However, the specific QCB geometry makes its spectral properties rather unusual. Consider an *isolated* array 1. As was mentioned in Section 3.2, within the (x_1, x_2)

plane, its excitations are characterized by a pair of $2D$ coordinates (x_1, n_2a) , i.e. a continuous longitudinal coordinate x_1 parallel to \mathbf{e}_1 direction, and its discrete transverse partner n_2a parallel to \mathbf{e}_2 . As a result, the longitudinal component $k_1 = q_1 + m_1Q$ of the excitation momentum changes on the entire axis $-\infty < k_1 < \infty$ while its transverse momentum q_2 is restricted to the region $|q_2| < Q/2$. Thus an eigenstate (plasmon) of the first array is characterized by the vector $\mathbf{k}_1 = \mathbf{q} + \mathbf{m}_1 = (k_1, q_2)$ and the frequency $\omega(\mathbf{k}_1) = v|k_1|$ which depends only on the longitudinal component k_1 of the momentum \mathbf{k}_1 . Similar description of the second array is obtained by replacing $1 \leftrightarrow 2$.

The exact differential cross section of the scattering in a given direction, considered as a function of the scattered frequency, has almost equidistant sets of peaks. However, because of weak inter-array interaction (3.6), only few peaks are well pronounced, whereas other peaks are very low and will be omitted below. Therefore in the approximation adopted here the scattering cross section is characterized by a number of peaks, their positions and intensities. Calculation of these quantities as functions of the frequency loss ω and azimuthal angle ϑ for various fixed values of the polar angle φ , is the goal of our study.

To perform quantitative analysis, we should derive an expression for the scattering cross section. All the details of our calculations are contained in Appendix E. Here we present only the main steps of the derivation. We start with the Hamiltonian

$$h_{nl} = \frac{ev_F}{c} \int \frac{dx_1 d\gamma}{2\pi} \psi_\alpha^\dagger \mathbf{A} \cdot \boldsymbol{\sigma}_{\alpha, \alpha'} \psi_{\alpha'}, \quad (6.1)$$

which describes interaction between a single nanotube oriented, e.g., along the \mathbf{e}_1 direction (the first array nanotube) and an external electromagnetic field. The field is described by its vector potential in the Landau gauge

$$\mathbf{A} = A_1 \mathbf{e}_1 + A_2 \mathbf{e}_2 + A_3 \mathbf{e}_3. \quad (6.2)$$

The indices $\alpha = A, B$ enumerate sublattices in a honeycomb carbon sheet, (r, γ) are polar coordinates in the (x_2, x_3) plane, $\psi_\alpha(x_1, \gamma) \equiv \psi_\alpha(x_1, r_0, \gamma)$ and ψ_α^\dagger are slowly varying electron field operators at the nanotube surface $r = r_0$, and the vector of Pauli matrices $\boldsymbol{\sigma}$ is $\boldsymbol{\sigma} = \mathbf{e}_1 \sigma_x + \mathbf{e}_\gamma \sigma_y$, $\mathbf{e}_\gamma = -\mathbf{e}_2 \sin \gamma + \mathbf{e}_3 \cos \gamma$. The light wavelength is much longer than the nanotube radius, so the vector potential can be taken at its axis, $\mathbf{A}(x_1, 0, 0)$.

Such form of a nanotube-light interaction leads to the following expression for an effective QCB-light interaction Hamiltonian

$$\begin{aligned} H_{int} &= \frac{\sqrt{2}}{4k} \frac{e^2}{\hbar c} \left(\frac{v_F}{c} \right)^2 \sum_{n_2} \int dx_1 \partial_{x_1} \theta_1(x_1, n_2a) \mathbf{A}_1^2(x_1, n_2a, 0) + \\ &+ \frac{\sqrt{2}}{4k} \frac{e^2}{\hbar c} \left(\frac{v_F}{c} \right)^2 \sum_{n_1} \int dx_2 \partial_{x_2} \theta_2(n_1a, x_2) \mathbf{A}_2^2(n_1a, x_2, d). \end{aligned} \quad (6.3)$$

Here $\mathbf{A}_j(\mathbf{r}) = \mathbf{A}(\mathbf{r}) + (\sqrt{2} - 1) A_j(\mathbf{r}) \mathbf{e}_j$ ($j = 1, 2$) are two effective vector potentials affecting two arrays and $A_j(\mathbf{r})$ are two (of three) cartesian components of the full vector potential

(6.2). The main subject of our interest is the scaled scattering differential cross-section $\sigma(\omega, \mathbf{n})$ defined by equation

$$d\sigma = \lambda L^2 \sigma(\omega, \mathbf{n}) d\omega do, \quad \lambda = \frac{g}{4\pi k a} \left(\frac{e^2}{\hbar c} \right)^2 \left(\frac{v_F}{c} \right)^4, \quad (6.4)$$

where L^2 is the QCB area and $do = \sin \varphi d\varphi d\vartheta$. A standard procedure applied to the Hamiltonian (6.3), leads to the following form of the scaled cross section

$$\sigma(\omega, \mathbf{n}) = \frac{1}{4k} \sum_P \overline{|\langle P | \mathbf{h} | 0 \rangle_p|^2} \delta(\omega - \omega_P). \quad (6.5)$$

Here $\omega = \Omega_i - \Omega_f$ is the frequency loss and

$$\mathbf{h} = - \sum_j \frac{k_j}{\sqrt{|k_j|}} P_{j;\lambda_f, \lambda_i}(\varphi, \vartheta) \left(a_{j, \mathbf{k}_j} + a_{j, -\mathbf{k}_j}^\dagger \right) \quad (6.6)$$

is the interaction Hamiltonian reduced to the subspace of QCB states and summation is performed over all one-plasmon states $|P\rangle$. $P_{j;\lambda_f, \lambda_i}(\varphi, \vartheta)$, $j = 1, 2$, are polarization matrices. In the basis (\parallel, \perp) they are given by

$$P_1(\varphi, \vartheta) = - \begin{pmatrix} 2 \sin \vartheta & i \cos \vartheta \\ 2i \cos \vartheta \cos \varphi & \sin \vartheta \cos \varphi \end{pmatrix}, \quad P_2(\varphi, \vartheta) = P_1\left(\frac{\pi}{2} + \vartheta, \varphi\right). \quad (6.7)$$

Equations (6.5) - (6.7) serve as a basis for the subsequent analysis.

6.3 Scattering Cross Section

6.3.1 Cross Section: Basic Types

According to Eqs. (6.5), (6.6), in order to contribute to the cross-section (6.5) for a fixed detector orientation at \mathbf{n} , an excited QCB plasmon $|P\rangle$ must contain at least one of two single-array states $|1, -\mathbf{k}_1\rangle$ or $|2, -\mathbf{k}_2\rangle$. Analysis shows that there are five basic types of excited QCB plasmons depending on the location of the point \mathbf{k} . Here we describe these types of plasmons and the corresponding structure of the differential scattering cross section. In this description beside the polar angle φ of the scattered photon wave vector \mathbf{K}_f , we use in a sense a mixed representation. It is based on the excited plasmon momentum \mathbf{k} and the azimuthal angle ϑ of the transverse component of the scattered photon wave vector \mathbf{K}_f .

i. The general case: The point \mathbf{k} lies away from both the high symmetry lines and the resonant lines. This case is illustrated by the point A in Fig. 6.2. There are two QCB plasmons $|P\rangle$, mostly propagating along the first or second array with the frequencies (B.2), which contribute to the scattering. The differential cross-section is a sum of two peaks centered at these frequencies. After averaging over initial polarizations and summing over

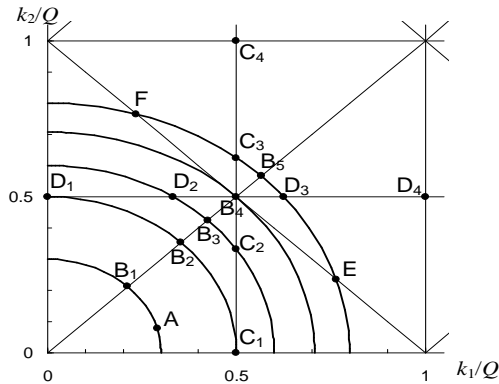


Figure 6.2: Part of inverse space. The small square $k_j/Q \leq 0.5$ is the quarter of the first QCB BZ. High symmetry lines are parallel to the coordinate axes. Resonant lines are parallel to BZ diagonals. The arcs coming over the point B_1, B_2, B_3, B_4, B_5 , correspond to different wave numbers of excited plasmons: $|k/Q| = 0.3; 0.5; 0.6; 0.7; 0.8$.

final polarizations, it has the form $\sigma(\omega, \mathbf{n}) = F_1(\mathbf{n})\delta(\omega - \omega_1) + F_2(\mathbf{n})\delta(\omega - \omega_2)$, where the functions $F_1(\mathbf{n}) \equiv F(\varphi, \vartheta)$ and $F_2(\mathbf{n}) = F(\varphi, \vartheta + \pi/2)$ describe universal angle dependence of the peak amplitudes,

$$F(\varphi, \vartheta) = |\sin \varphi \cos \vartheta| \left[1 - \frac{3}{4} \sin^2 \varphi \cos^2 \vartheta + \frac{1}{4} \cos^2 \varphi \right].$$

The functions $F_{1,2}$ are related to the corresponding array plasmons. Each one of them vanishes when the scattered photon is perpendicular to the corresponding array. However, these functions describe the scaled cross section. The absolute value amplitude of each peak has an additional factor λ (see Eq. (6.4)). Strong electron-electron interaction in a nanotube corresponds to small values of the Luttinger parameter g and therefore suppresses the scattering cross-section.

ii. Inter-band resonance in one of the arrays: the point \mathbf{k} lies on a high symmetry line of only one array. This case is illustrated by the points $C_{2,3}$ (1-st array) and $D_{2,3}$ (2-d array) in Fig. 6.2. Consider for example point C_2 where $k_1 = Q/2, k_2 \neq nQ/2$. Here *three* QCB plasmons contribute to the scattering. The first one is $|2, k_2\rangle$ plasmon propagating along the second array with quasimomentum k_2 and frequency ω_2 , Eq. (B.2). The two others are even or odd superpositions of the 1-st array states (Eq. (B.10) with $j = 1$) of the two first zones with eigenfrequencies (B.11). Due to weakness of the inter-array interaction, three peaks of the scattering cross section form a singlet ω_2 and doublet ω_{1g}, ω_{1u} . After averaging over initial and final polarizations, the cross section has the form $\sigma(\omega, \mathbf{n}) = 2^{-1} \sum_j F_j(\mathbf{n})[\delta(\omega - \omega_{jg}) + \delta(\omega - \omega_{ju})]$.

iii. Inter-band resonance in both arrays: The point \mathbf{k} is a crossing point of two high symmetry lines away from all resonant lines. This case is illustrated by the points C_4 and D_4 in Fig. 6.2. Consider for example point C_4 . Here $k_1 = Q/2, k_2 = 2Q/2$,

and *four* QCB plasmons contribute to the scattering. The first pair consists of even and odd superpositions of the 1-st array states of the first and the second bands. These states and their frequencies are described by Eqs. (B.14), (B.15) with $j = 1$. The second pair consists of the same superpositions of the 2-d array states from the second and third bands and is described by the same equations with $j = 2$. As a result, *four* peaks, which form two doublets (B.15), $j = 1, 2$, can be observed. After averaging over initial and final polarizations the cross section is $\sigma(\omega, \mathbf{n}) = 2^{-1} \sum_j F_j(\mathbf{n}) [\delta(\omega - \omega_{jg}) + \delta(\omega - \omega_{ju})]$.

iv. Inter-array resonance: The point \mathbf{k} lies only on one of the resonant lines away from the high symmetry lines. This case is illustrated by the points $B_{1-3,5}$, E , and F in Fig. 6.2. Here the QCB plasmons which contribute to the scattering are two even and two odd superpositions of the first and second array states (B.12) whose eigenfrequencies form two doublets (B.13). As in the previous case, the scattering cross section contains *four* peaks which form two doublets. After averaging over initial and final polarizations the cross section is $\sigma(\omega, \mathbf{n}) = 2^{-1} \sum_j F_j(\mathbf{n}) [\delta(\omega - \omega_g(\mathbf{k}_j)) + \delta(\omega - \omega_u(\mathbf{k}_j))]$.

Thus, the inter-array splitting is proportional to the main small parameter (3.8) of the theory, $\phi \approx 0.007$ [58]. For the set of parameters described in the beginning of subsection 3.5, the inter-band splitting defined by Eq. (B.11), is five times smaller because it contains an additional factor $\phi a/r_0$.

v. Inter-array and inter-band resonance: The point \mathbf{k} lies at the intersection of two resonant lines. There is only one such point B_4 in Fig. 6.2. In the general case, where the parameter $n \neq 0$ for both crossing resonant lines (the point B_4 is *not* the case), the QCB plasmons involved in Raman scattering form two quartets. The first quartet consists of four symmetrized combinations (B.16) of the single-array states. QCB eigenstates for the second quartet are obtained from these equations by replacing $1 \leftrightarrow 2$. The corresponding eigen-frequencies are described by Eqs. (B.17), (B.18). The scattering cross section in this case contains six peaks, and two of them are two-fold degenerate

$$\sigma(\omega, \mathbf{n}) = \frac{1}{4} \sum_j F_j(\mathbf{n}) [2\delta(\omega - \omega_{g,u/g}(\mathbf{k}_j)) + \delta(\omega - \omega_{uu}(\mathbf{k}_j)) + \delta(\omega - \omega_{ug}(\mathbf{k}_j))].$$

The point B_4 in Fig. 6.2 lies on the main resonance line with $n = 0$. Here $|k_1| = |k_2|$, the frequencies of both quartets coincide, and the scattering cross section contains one four-fold degenerate peak and a symmetric pair of its two-fold degenerate satellites.

This classification of all types of excited plasmons enables us to describe completely the UV scattering on QCB.

6.3.2 Scattering Indicatrices

In this part we describe the results of the scattering process with the help of a family of scattering indicatrices.

To explain the indicatrix structure, we start with some preliminary arguments. Consider the case where the detector is tuned on the frequency Ω_f and is oriented in direction \mathbf{n} . These parameters determine a point \mathbf{k} by a unique way. There are two ways of scanning QCB plasmons. The first way is to scan the polar angle ϑ . The corresponding points \mathbf{k} in Fig. 6.2 form a circle with radius $k = (\Omega_f/c) \sin \varphi$. The second way is to tune the detector frequency as Ω_f . We are interested in frequency loss of order of the plasmon frequencies within the two - three lowest bands. This loss is of order of $\Omega_f(v/c) \ll \Omega_f$. Therefore in this case the point \mathbf{k} remains on its place with a very good accuracy.

Each scattering indicatrix corresponds to a circular arc in Fig. 6.2 and the structure of the indicatrix is completely determined by the arc radius k . The indicatrix represents a set of curves displayed in polar coordinates with polar angle, which coincides with the polar angle ϑ used above, and the (dimensionless) radius $\omega/(vQ)$, where ω is the frequency loss. Each point of the indicatrix corresponds to an excitation of a QCB plasmon and therefore to a sharp peak in the scattering cross section. The number of peaks depends on the polar angle. Scanning the polar angle ϑ results in changing the number of peaks. This is one more example of dimensional crossover in QCB (see Chapter 4 for similar effects in IR spectroscopy).

We start with the case of the smallest radius $K \sin \varphi = -0.3Q$ (arc AB_1 in Fig. 6.2). Here all points beside the point B_1 are points of general type (i). Each one of them, e.g., point A , corresponds to excitation of two plasmons in the two arrays and therefore leads to two separate peaks in the scattering spectrum (see Fig. 6.3, left panel). The peaks corresponding to the point A in Fig. 6.2 lie on the ray defined by the angle θ_A . The point B_1 corresponds to an inter-array resonance (iv) and in this direction a split doublet can be observed.

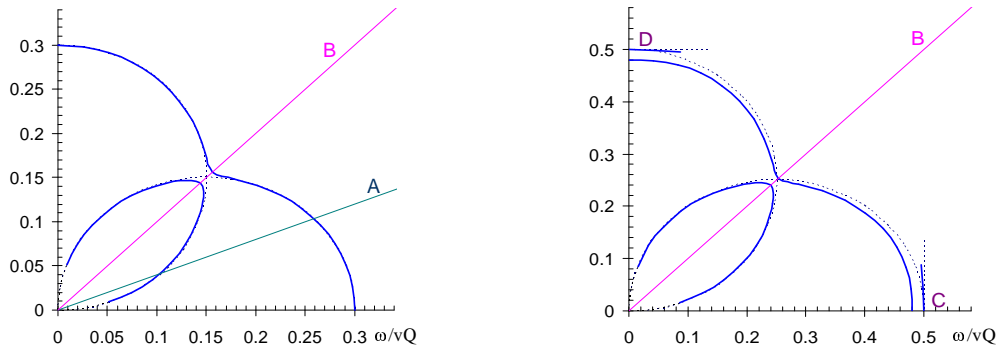


Figure 6.3: **Left panel:** Positions of the scattering peaks for $|k/Q| = 0.3$. The doublet in the resonance direction (point B_1 in Fig. 6.2) is well pronounced. **Right panel:** Positions of the scattering peaks for $|k/Q| = 0.5$. Two doublets appear at the BZ boundaries (points C_1 and D_1 in Fig. 6.2).

In the next case $K \sin \varphi = -0.5Q$ (arc $C_1B_2D_1$ in Fig. 6.2), as in the previous one, in the

general directions one can observe two single lines which form a split doublet in the resonant direction B_2 . However at the final points C_1 and D_1 the arc touches the high symmetry lines. Here the low frequency single line vanishes (there is no scattering at $k = 0$) while the high frequency line transforms into a doublet because of an inter-band resonance (ii) in one of the arrays (Fig. 6.3, right panel).

Further increase of the arc radius $K \sin \varphi = -0.6Q$ (arc $C_2B_3D_2$ in Fig. 6.2) leads to appearance of two points D_2 and C_2 where the arc intersects with high symmetry lines (BZ boundaries). Each of these points generates an inter-band resonance doublet, which coexists with the low frequency single peak (Fig.6.4, left panel).

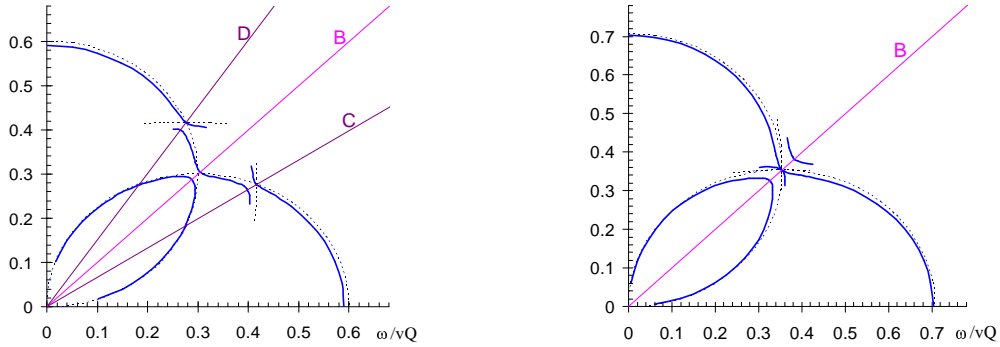


Figure 6.4: **Left panel:** Positions of the scattering peaks for $|k/Q| = 0.6$. Two doublets at the BZ boundaries (points C_2 and D_2) in Fig. 6.2) are shifted from the high symmetry directions. **Right panel:** Positions of the scattering peaks for $|k/Q| = \sqrt{2}/2$. Resonance triplet corresponding to point B_4 in Fig. 6.2 (two of four frequencies remain degenerate in our approximation). In IR experiments only one of the triplet components is seen.

In the case $K \sin \varphi = -\sqrt{2}Q/2$ the corresponding arc includes the BZ corner B_4 . This is the point of a double inter-array and inter-band resonance (v). Moreover, here, the two quartets described above coincide. Therefore, there are three lines in Fig. 6.4, right panel. The low-frequency line as its high-frequency partner is two-fold degenerate while the central line is four-fold degenerate. We emphasize that each quartet manifests itself in three lines, contrary to the IR absorption, where selection rules make two of them invisible.

The last case $K \sin \varphi = -0.8Q$ demonstrates one more possibility related to inter-band resonance simultaneously in two arrays (iii). Each point E and F generates (in the corresponding direction) two doublets describing the inter-band splitting in different arrays (see Fig. 6.5).

6.4 Conclusions

In conclusion, we studied inelastic UV Raman scattering on QCB. We derived an effective Hamiltonian for QCB-light interaction which is expressed via the same Bose variables that

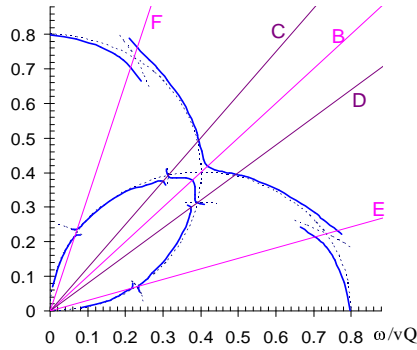


Figure 6.5: Positions of the scattering peaks for $|k/Q| = 0.8$. Two pairs of doublets appear corresponding to excitation of two pairs of plasmons in the two arrays (points E and F in Fig. 6.2).

the QCB itself. With the help of this Hamiltonian we calculated the differential scattering cross section as a function of detector orientation and scattered frequency. Scanning these parameters, one can observe a set of sharp peaks in the scattering spectrum. The number of peaks and their positions strongly depend on the direction of the scattered wave vector. This results in a dimensional crossover. It manifests itself in the splitting of the peak frequencies and therefore in appearance of multiplets (mostly doublets) instead of single lines in the scattering spectrum.

The sizes of peak splitting are determined by the nature of interaction which lifts the corresponding degeneracy. In the case of initial inter-array degeneracy, the splitting is proportional to the dimensionless interaction strength $\phi \approx 0.007$. The inter-band splitting is proportional to the square of this parameter. For chosen QCB parameters it is smaller than the inter-array interaction strength in spite of an additional large multiplier a/r_0 . In all cases, the splitting increases with increasing the interaction in QCB crosses. The peak amplitudes are proportional to the Luttinger parameter g in a single nanotube. Therefore strong electron-electron interaction suppresses the peaks.

The effectiveness of UV scattering is related to the possibility of changing continuously the excited plasmon frequency. Due to other selection rules, some lines which are invisible in the IR absorption spectrum, become observable in the UV scattering. UV scattering spectroscopy enables one to restore parameters describing both interaction in QCB crosses and electron-electron interaction in a single QCB constituents.

Our studies of optical properties of QCB (this Chapter and Chapters 4 and 5) show that these nanoobjects possess a unique combination of optical spectra. Firstly, they are active in IR and UV frequency range. Secondly, they may be observed in various kinds of optical processes, namely direct and indirect absorption, diffraction, energy loss transmission, and Raman-like spectroscopy.

Appendix A

Empty Super-Chain

Here we construct eigenfunctions, spectrum, and quasi-particle operators for an “empty super-chain” - quantum wire in an infinitely weak periodic potential with period a . Excitations in an initial wire are described as plane waves $L^{-1/2} \exp(ikx)$ with wave number $k = 2\pi n/L$, with integer n , and dispersion law $\omega(k) = v|k|$ (the array number is temporarily omitted). The following orthogonality relations are valid

$$\int_{-L/2}^{L/2} \psi_k^*(x) \psi_{k'}(x) dx = \delta_{k,k'}, \quad \sum_k \psi_k^*(x) \psi_k(x') = \delta_L(x - x'),$$

where δ_L stands for periodic delta-function

$$\delta_L(x - x') \equiv \sum_n \delta(x - x' - nL).$$

An “empty super-chain” is characterized by a space period a and a corresponding reciprocal lattice wave number $Q = 2\pi/a$. Each excitation in such a super-chain is described by its quasi-wavenumber q and a band number s ($s = 1, 2, \dots$) that are related to the corresponding wave number k by the following relation,

$$k = q + Q(-1)^{s-1} \left[\frac{s}{2} \right] \text{sign } q.$$

Here, square brackets denote an integral part of a number. The corresponding wave function $\psi_{s,q}(x)$ has the Bloch-type structure,

$$\psi_{s,q}(x) = \frac{1}{\sqrt{L}} e^{iqx} u_{s,q}(x), \quad (\text{A.1})$$

and satisfies the orthogonality relations

$$\int_{-L/2}^{L/2} \psi_{s,q}^*(x) \psi_{s',q'}(x) dx = \delta_{s,s'} \sum_m \delta_{q+mQ,q'}, \quad \sum_{s,q} \psi_{s,q}^*(x) \psi_{s,q}(x') = \delta_L(x - x'),$$

Within the first BZ, $-Q/2 \leq q < Q/2$, Bloch amplitude and dispersion law ω_s have the following form

$$u_{s,q}(x) = \exp \left\{ iQx(-1)^{s-1} \left[\frac{s}{2} \right] \text{sign } q \right\}, \quad \omega_s(q) = vQ \left(\left[\frac{s}{2} \right] + (-1)^{s-1} \frac{|q|}{Q} \right). \quad (\text{A.2})$$

Taking into account that both Bloch amplitude $u_{s,q}(x)$ and dispersion law $\omega_s(q)$ are periodic functions of q with period Q , one obtains general equations for the Bloch amplitude

$$u_{s,q}(x) = \sum_{n=-\infty}^{\infty} \frac{\sin \xi_n}{\xi_n} \cos[(2s-1)\xi_n] \exp\left(-4i\xi_n \frac{q}{Q}\right), \quad 4\xi_n = Q(x - na),$$

and dispersion law $\omega_s(q)$

$$\frac{\omega_s(q)}{vQ} = \frac{2s-1}{4} + \sum_{n=1}^{\infty} \frac{2(-1)^s}{\pi^2(2n+1)^2} \cos \frac{2\pi(2n+1)q}{Q}.$$

The relations between quasiparticle operators for a free wire, c_k , for momentum $k \neq nQ/2$ with n integer, and those for an empty super-chain, $C_{s,q}$, for quasimomentum q from the first BZ, $-Q/2 < q < Q/2$, look as

$$c_k = C_{s,q} \text{sign} k, \quad s = 1 + \left[\frac{2|k|}{Q} \right], \quad q = Q \left(\left\{ \frac{k}{Q} + \frac{1}{2} \right\} - \frac{1}{2} \right)$$

$$C_{s,q} = (-1)^\nu c_k, \quad k = q + (-1)^\nu Q \left[\frac{s}{2} \right], \quad \nu = s + 1 + \left[\frac{2q}{Q} \right],$$

where curly brackets denote a fractional part of a number. For obtaining these relations we used the following expression

$$\int_{-L/2}^{L/2} \psi_k^*(x) \psi_{s,q}(x) dx = \delta_{s,s(q)} \text{sign} k \sum_m \delta_{q+mQ,k}, \quad s(q) = 1 + \left[\frac{2|q|}{Q} \right],$$

for the transition amplitude $\langle k|s,q \rangle$. In case when $k = nQ/2$ with n integer, hybridization of the neighboring bands should be taken into account. This modifies the above relations by the following way

$$c_{nQ/2} = \theta(n) [\alpha_n C_{n,q_n} + \beta_n C_{n+1,q_n}] + \theta(-n) [\beta_{-n}^* C_{-n,q_n} - \alpha_{-n}^* C_{-n+1,q_n}],$$

$$q_n = Q \left(\left\{ \frac{n+1}{2} \right\} - \frac{1}{2} \right), \quad C_{s,q_s} = \alpha_s^* c_{sQ/2} + \beta_s c_{-sQ/2}, \quad C_{s+1,q_s} = \beta_s^* c_{sQ/2} - \alpha_s c_{-sQ/2},$$

where α, β are hybridization coefficients. Corresponding relations between wave functions follow immediately from these formulas.

Alternatively, each mode with the quasi-wavenumber q in the energy band s (reduced BZ description) can be described by the wave number $k = q + mQ$ (extended BZ description), where $m = (-1)^s \text{sign}(q) [s/2]$. Within this scheme, Bloch amplitude and dispersion law $\omega(k)$ have the following simple form $u_k(x) = e^{ikx}$, $\omega(k) = v|k|$.

To write down any of these formulas for a specific array, one should add the array index j to the wave function ψ , Bloch amplitude u , coordinate x , quasimomentum q , and to the periods a and Q of the super-chain in real and reciprocal space.

Appendix B

Spectrum and Correlators of Square QCB

B.1 Square QCB Spectrum

Here we obtain analytical expressions for dispersion laws and wave functions of QCB. For quasimomenta far from the BZ boundaries, the energy spectrum of the first band can be calculated explicitly. Assuming that $\omega^2 \ll \omega_s^2(q_j)$, $s = 2, 3, 4, \dots$, we omit ω^2 in all terms in the r.h.s. of Eq. (3.15) except the first one, $s = 1$. As a result the secular equation (3.15) reads

$$\prod_{j=1}^2 \left(\frac{R_0}{a} \frac{\zeta_1^2(q_j) \omega^2}{\omega^2(q_j) - \omega^2} + F_0 \right) = \frac{1}{\varepsilon},$$

where $\omega^2(q) = \omega_1^2(q)$. The solutions of this equation have the form:

$$\omega_{\nu 1 \mathbf{q}}^2 = \frac{\tilde{\omega}_1^2(\mathbf{q}) + \tilde{\omega}_2^2(\mathbf{q})}{2} \pm \left[\left(\frac{\tilde{\omega}_1^2(\mathbf{q}) - \tilde{\omega}_2^2(\mathbf{q})}{2} \right)^2 + \phi_{\mathbf{q}} \right]^{1/2}. \quad (\text{B.1})$$

Here $\phi_{\mathbf{q}} = \varphi^2 \zeta_1^2(q_1) \zeta_1^2(q_2) \omega^2(q_1) \omega^2(q_2)$, $\nu = +, -$ is the branch number, $\tilde{\omega}_j(\mathbf{q})$ is determined as

$$\tilde{\omega}_1^2(\mathbf{q}) = \omega^2(q_1) \frac{1 - \varepsilon F_0 (F_0 - \varphi^2(q_2))}{1 - \varepsilon (F_0 - \varphi^2(q_1)) (F_0 - \varphi^2(q_2))}, \quad \varphi^2(q_j) = \frac{R_0}{a} \zeta_1^2(q_j) \quad (\text{B.2})$$

for $j = 1$. Expression for $\tilde{\omega}_2^2(\mathbf{q})$ can be obtained by permutation $1 \leftrightarrow 2$. The expression inside the parentheses on the r.h.s. of Eq. (B.2) describes the contributions to F_0 from higher bands. Therefore $\tilde{\omega}_j^2(\mathbf{q})$ is the j -th array frequency renormalized by the interaction with higher bands. In principle, contribution of higher bands may turn the interaction to be strong. However, for the specific case of carbon nanotubes, one stays far from the critical value ε_c (see estimates at the end of subsection 3.4). Therefore the interaction with higher bands is weak in almost all the BZ except its boundaries.

The resonance line equation is $\omega(q_1) = \omega(q_2)$. Out of this line the branch number is in fact the array number and the renormalized frequencies are frequencies of a boson propagating

along one of the arrays slightly modified by interactions with the complementary array. In case when $\omega(q_1) > \omega(q_2)$, one obtains

$$\omega_{+,1\mathbf{q}}^2 \approx \omega^2(q_1) (1 - \varepsilon F_0 \varphi^2(q_1)), \quad \omega_{-,1\mathbf{q}}^2 \approx \omega^2(q_2) (1 - \varepsilon F_0 \varphi^2(q_2)). \quad (\text{B.3})$$

In the opposite case one should replace indices $+ \leftrightarrow -$.

Consider the frequency correction in the latter equation in more details. The correction term can be approximately estimated as $\omega^2(q_j)S(q_j)$ with

$$S(q) = \varepsilon F_0 \varphi^2(q) = \varepsilon \frac{R_0}{a} \zeta_1^2(q) \int d\xi \zeta^2(\xi). \quad (\text{B.4})$$

Due to the short-range character of the interaction, the matrix elements $\zeta_1(q) \sim 1$ vary slowly with the quasimomentum $q \leq Q$. Therefore, the r.h.s. in Eq.(B.4) can be roughly estimated as $S(q) \sim \varepsilon R_0/a = 0.1R_0/a \ll 1$. One should also remember that the energy spectrum of nanotube remains one-dimensional only for frequencies smaller than some ω_m . Therefore, an external cutoff arises at $s \sim ak_m$ where $k_m \sim \omega_m/v$. As a results one gets an estimate $S(q) \sim \varepsilon k_m R_0^2/a$. Hence, one could hope to gain additional power of the small interaction radius. However, for nanotubes, k_m is of the order of $1/R_0$ (see Refs. [49, 18]) and both estimates coincide. For quasimomenta close to the BZ center, the coefficient $S(q)$ can be calculated exactly. For exponential form of $\zeta(\xi) \propto \exp(-|\xi|)$, one obtains, $S(0) = 0.14R_0/a$. Thus, the correction term in Eq.(B.3) is really small.

The eigenstates of the system are described by renormalized field operators. Within the first band they have the form

$$\tilde{\theta}_{11\mathbf{q}} = \alpha_{1\mathbf{q}} (u_{\mathbf{q}} \theta_{11\mathbf{q}} - v_{\mathbf{q}} \theta_{21\mathbf{q}}) - \sum_{s=2}^{\infty} (\phi_{1s\mathbf{q}} u_{\mathbf{q}} \theta_{2s\mathbf{q}} + \phi_{2s\mathbf{q}} v_{\mathbf{q}} \theta_{1s\mathbf{q}}), \quad (\text{B.5})$$

$$\tilde{\theta}_{21\mathbf{q}} = \alpha_{2\mathbf{q}} (v_{\mathbf{q}} \theta_{11\mathbf{q}} + u_{\mathbf{q}} \theta_{21\mathbf{q}}) - \sum_{s=2}^{\infty} (\phi_{1s\mathbf{q}} v_{\mathbf{q}} \theta_{2s\mathbf{q}} + \phi_{2s\mathbf{q}} u_{\mathbf{q}} \theta_{1s\mathbf{q}}). \quad (\text{B.6})$$

Here the coefficients $u_{\mathbf{q}}$ and $v_{\mathbf{q}}$ describe mixing between the modes with different array indices, within the first band,

$$u_{\mathbf{q}} = \left(\frac{\sqrt{\Delta_{\mathbf{q}}^2 + \phi_{1\mathbf{q}}^2} + \Delta_{\mathbf{q}}}{2\sqrt{\Delta_{\mathbf{q}}^2 + \phi_{1\mathbf{q}}^2}} \right)^{1/2}, \quad v_{\mathbf{q}} = \left(\frac{\sqrt{\Delta_{\mathbf{q}}^2 + \phi_{1\mathbf{q}}^2} - \Delta_{\mathbf{q}}}{2\sqrt{\Delta_{\mathbf{q}}^2 + \phi_{1\mathbf{q}}^2}} \right)^{1/2}, \quad (\text{B.7})$$

and

$$\Delta_{\mathbf{q}} = (\omega^2(q_2) - \omega^2(q_1))/2, \quad \phi_{1\mathbf{q}} = \sqrt{\varepsilon} \zeta_1(q_1) \zeta_1(q_2) \omega_1(q_1) \omega_1(q_2),$$

$\varepsilon = \phi a/R_0$. The parameters $\phi_{js\mathbf{q}}$, $s = 2, 3, \dots$, in Eqs. (B.5), (B.6) correspond to inter-band mixing,

$$\phi_{1s\mathbf{q}} = \phi \zeta_1(q_1) \zeta_s(q_2) \omega_1(q_1) / \omega_s(q_2),$$

and the coefficients $\alpha_{1\mathbf{q}}$ take into account corrections from the higher bands

$$\alpha_{1\mathbf{q}}^2 = 1 - \sum_{s=2}^{\infty} (\phi_{1s\mathbf{q}}^2 u_{\mathbf{q}}^2 + \phi_{2s\mathbf{q}}^2 v_{\mathbf{q}}^2).$$

Expressions for $\phi_{2s\mathbf{q}}$ and $\alpha_{2\mathbf{q}}$ can be obtained by permutation $1 \leftrightarrow 2$.

Equations (B.1), (B.5) and (B.6) solve the problem of QCB energy spectrum within the first band and away from the BZ boundaries. However, due to smallness of the interaction, the general expressions for the eigenstates of QCB for arbitrary energy band can be obtained. For quasimomenta far from the high symmetry lines $k_j = \pm Q/2$, the energy spectrum can be calculated explicitly. Let us consider the s -th energy band and assume that

$$|\omega^2 - \omega_{s'}^2(q_j)| \ll \phi^2 \omega_{s'}^2(q_j), \quad s' \neq s.$$

Moreover, we consider the wave vector lying away from the resonant lines $k_1 = \pm k_2 + mQ$ with m integer. Then, in zeroth approximation, the QCB eigenstates coincide with ‘‘empty QCB’’ eigenstates $|1, s_1, q_1\rangle$ and $|2, s_2, q_2\rangle$, i.e., belong to a given array and energy band. (Here we represent the wave vector \mathbf{k} as $\mathbf{k} = \mathbf{q} + \mathbf{m}$, where the quasi-momentum \mathbf{q} belongs to the first BZ, whereas $\mathbf{m} = \mathbf{m}_1 + \mathbf{m}_2$ is reciprocal super-lattice vector, $\mathbf{m}_j = m_j Q \mathbf{e}_j$, $j = 1, 2$, m_j is integer. The band numbers s_j are $s_j = 1 + [2|k_j|/Q]$.) The inter-array interaction mixes the modes propagating along both arrays. The eigenstates of QCB are described by renormalized field operators

$$\tilde{\theta}_{1,s,\mathbf{q}} = \alpha_{1,s,\mathbf{q}} \theta_{1,s,\mathbf{q}} + \phi \sum_{s'=1}^{\infty} \frac{\zeta_{s'}(q_2) \omega_{s'}(q_2) \zeta_s(q_1) \omega_s(q_1)}{\omega_{s'}^2(q_2) - \omega_s^2(q_1)} \theta_{2,s',\mathbf{q}}, \quad (\text{B.8})$$

where

$$\alpha_{1,s,\mathbf{q}}^2 = 1 - \phi^2 \sum_{s'=1}^{\infty} \left(\frac{\zeta_{s'}(q_2) \omega_{s'}(q_2) \zeta_s(q_1) \omega_s(q_1)}{\omega_{s'}^2(q_2) - \omega_s^2(q_1)} \right)^2.$$

The corresponding eigenfrequency is a slightly modified frequency of bosons propagating along the first arrays,

$$\tilde{\omega}_{1,s,\mathbf{q}}^2 = \omega_s^2(q_1) - \phi^2 \sum_{s'=1}^{\infty} \frac{\zeta_{s'}^2(q_2) \omega_{s'}^2(q_2) \zeta_s^2(q_1) \omega_s^2(q_1)}{\omega_{s'}^2(q_2) - \omega_s^2(q_1)}, \quad (\text{B.9})$$

Expressions for $\tilde{\theta}_{2,s,\mathbf{q}}$, $\alpha_{2,s,\mathbf{q}}^2$, and $\tilde{\omega}_{2,s,\mathbf{q}}^2$ can be obtained by permutation $1 \leftrightarrow 2$.

As was mentioned in subsection 3.5, description of QCB plasmons in terms of array plasmons fails at the points lying at two specific groups of lines in reciprocal space. Nevertheless, QCB plasmons even at these lines can be considered as finite combinations of array plasmons generated by a more complicated way. Below we consider various types of the interference of array plasmons in QCB.

The first group of specific lines is formed by the high symmetry lines $k_j = p_j Q/2$ with p_j an integer (the corresponding quasi-momentum has a component $q_j = 0$ for p_j even or $Q/2$ for p_j odd, the reciprocal lattice vector is $\mathbf{m}_j = [|p_j|/2]$). In an “empty lattice” approximation, these lines are degeneracy lines which separate s_j -th and $(s_j + 1)$ -th bands of the j -th array ($s_j = |p_j|$). Inter-array interaction mixes the array states, lifts the (inter-band) degeneracy and splits the corresponding frequencies. As a result, the QCB plasmons related to a point \mathbf{k} lying at a high symmetry line (e.g. all C, D points in Fig. 6.2), are built from the array plasmons associated not only with the points $\mathbf{k}_{1,2}$ but also with the symmetric (with respect to coordinate axes of a reciprocal space) points $\mathbf{k}_{\bar{1}} = (-k_1, q_2)$ and $\mathbf{k}_{\bar{2}} = (q_1, -k_2)$. (Indeed, if the condition $k_j = p_j Q/2$ is fulfilled, $-k_j = k_j - p_j Q$, and then both these wave-numbers correspond to the same quasi-wave-number q_j in the first BZ.)

Consider for definiteness the case $j = 1$ and assume first that the ratio $2k_2/Q$ is non-integer. In this case, the point $\mathbf{k} = \mathbf{q} + \mathbf{m}$ generates three QCB plasmons. The first of them is plasmon $\tilde{\theta}_{2,s_2,\mathbf{q}}$ (B.8) propagating along the second array with quasimomentum q_2 and frequency $\omega_{2,s_2,\mathbf{q}}$ (B.9). The two others

$$\begin{aligned}\tilde{\theta}_{1,s_1,g,\mathbf{q}} &= \frac{1}{\sqrt{2}} (\theta_{1,s_1,\mathbf{q}} + \theta_{1,s_1+1,\mathbf{q}}), \\ \tilde{\theta}_{1,s_1,u,\mathbf{q}} &= \frac{1}{\sqrt{2}} (\theta_{1,s_1,\mathbf{q}} - \theta_{1,s_1+1,\mathbf{q}}) + \sqrt{2}\phi \sum_{s'=1}^{\infty} \frac{\zeta_{s'}(q_2)\omega_{s'}(q_2)\zeta_{s_1}(q_1)\omega_{s_1}(q_1)}{\omega_{s'}^2(q_2) - \omega_{s_1}^2(q_1)} \theta_{2,s',\mathbf{q}}\end{aligned}\quad (\text{B.10})$$

are even or odd superpositions of the 1-st array states from the two zones s_1 and $s_1 + 1$ with eigenfrequencies

$$\tilde{\omega}_{1,s_1,g,\mathbf{q}}^2 = \omega_{s_1}^2(q_1), \quad \tilde{\omega}_{1,s_1,u,\mathbf{q}}^2 = \omega_{s_1}^2(q_1) - 2\phi^2 \sum_{s'=1}^{\infty} \frac{\zeta_{s'}^2(q_2)\omega_{s'}^2(q_2)\zeta_{s_1}^2(q_1)\omega_{s_1}^2(q_1)}{\omega_{s'}^2(q_2) - \omega_{s_1}^2(q_1)}.\quad (\text{B.11})$$

The case $j = 2$ is described similarly after change $1 \leftrightarrow 2$.

The second set is formed by the resonant lines defined by the equation $k_1 + rk_2 = nQ$, where $r = \pm 1$ and n are two integer parameters determining the line. The corresponding quasi-momentum satisfy the equality $q_1 + rq_2 = 0$, then it lies on the diagonal of the first BZ (see Fig. 3.3). In an “empty lattice” approximation, these lines are also degeneracy lines. However this degeneracy has more complicated nature. Here there is a dual point $\bar{\mathbf{k}} = (-rk_2, -rk_1)$ which satisfies the equalities $-rk_2 = k_1 - nQ$ and $-rk_1 = -k_2 + rnQ$, and therefore this point corresponds to the *same* quasimomentum \mathbf{q} as the point \mathbf{k} . As a result, the array plasmons associated with the points \mathbf{k} and $\bar{\mathbf{k}}$ are involved in the resonance. Inter-array interaction mixes degenerate modes, lifts the degeneracy, and splits degenerate frequencies. As a result, the QCB plasmons related to a point \mathbf{k} at the resonant line (e.g. all B, F, E points in Fig. 6.2), are built from the array plasmons associated not only with the points $\mathbf{k}_{1,2}$ but also with the symmetric (with respect to one of the bisector lines of the coordinate system of a reciprocal space) points $\bar{\mathbf{k}}_1 = (-rk_1, -rq_2)$ and $\bar{\mathbf{k}}_2 = (-rq_1, -rk_2)$.

Moreover, if the point \mathbf{k} lies at an intersection of two resonant lines (the point W in Fig. 3.3), the QCB plasmons include also array states associated with the $\bar{\mathbf{k}}_j$ points.

In the general case, the point $\mathbf{k} = \mathbf{q} + \mathbf{m}$ lies only on one of the resonant lines $q_1 = \pm q_2$ away from the high symmetry lines. Here the point \mathbf{k} generates two pairs of even and odd superpositions of the first and the second array states (two doublets). The first of them, $\tilde{\theta}_{g/u,s_1,\mathbf{q}}$, lies in the energy band $s_1 = 1 + [2|k_1|/Q]$,

$$\begin{aligned}\tilde{\theta}_{g/u,s_1,\mathbf{q}} &= \theta_{g/u,s_1,\mathbf{q}} + \phi \sum_{s' \neq s_1} \frac{\zeta_{s'}(q_2)\omega_{s'}(q_2)\zeta_{s_1}(q_1)\omega_{s_1}(q_1)}{\omega_{s'}^2(q_2) - \omega_{s_1}^2(q_1)} \theta_{g/u,s',\mathbf{q}}, \\ \theta_{g/u,s_1,\mathbf{q}} &= \frac{1}{\sqrt{2}} (\theta_{1,s_1,\mathbf{q}} \pm \theta_{2,s_1,\mathbf{q}}), \quad j = 1, 2.\end{aligned}\tag{B.12}$$

The corresponding eigenfrequencies form two doublets

$$\omega_{g/u,s_1,\mathbf{q}}^2 = (1 \pm \phi) \omega_{s_1}^2(q_1) - \phi^2 \sum_{s' \neq s_1} \frac{\zeta_{s'}^2(q_2)\omega_{s'}^2(q_2)\zeta_{s_1}^2(q_1)\omega_{s_1}^2(q_1)}{\omega_{s'}^2(q_2) - \omega_{s_1}^2(q_1)}.\tag{B.13}$$

The eigenfunctions and eigenfrequencies of another doublet are obtained similarly by replacing the indices $1 \leftrightarrow 2$.

The crossing points of the resonant lines can also be divided into two groups. The first group is formed by the crossing points of only two high symmetry lines (points X_1 and X_2 in Fig. 3.3, left panel). Here, each of the generated vectors \mathbf{k}_1 and \mathbf{k}_2 corresponds to a pair of array eigenstates belonging to two adjacent 1D bands. Thus an *inter-band* mixing is significant in both arrays. Consider for definiteness the point X_1 . In this case the wave vector \mathbf{k} (\mathbf{k}_j) of the extended BZ can be represented as $\mathbf{k} = \mathbf{q} + \mathbf{m}$ ($\mathbf{k}_j = \mathbf{q} + \mathbf{m}_j$), with $\mathbf{q} = (Q/2, 0)$. As a result, in ‘‘empty lattice’’ approximation, we have two sets of degeneracy lines. The first one of them corresponds to odd and next even bands of the first array ($q_1 = Q/2$), whereas the second one describes degeneracy of even and next odd bands of the second array ($q_2 = 0$). The corresponding QCB plasmons are even or odd combinations of the j -th array plasmons ($j = 1, 2$). For $j = 1$, we have,

$$\tilde{\theta}_{1,s_1,g,\mathbf{q}} = \theta_{1,s_1,g,\mathbf{q}}, \quad \tilde{\theta}_{1,s_1,u,\mathbf{q}} = \theta_{1,s_1,u,\mathbf{q}} + 2\phi \sum_{n=1}^{\infty} \frac{\zeta_{2n}(q_2)\omega_{2n}(q_2)\zeta_{s_1}(q_1)\omega_{s_1}(q_1)}{\omega_{2n}^2(q_2) - \omega_{s_1}^2(q_1)} \theta_{2,2n,u,\mathbf{q}},\tag{B.14}$$

where

$$\theta_{j,s,g/u,\mathbf{q}} = \frac{1}{\sqrt{2}} (\theta_{j,s,\mathbf{q}} \pm \theta_{j,s+1,\mathbf{q}}).$$

The corresponding eigenfrequencies are

$$\tilde{\omega}_{1,s_1,g,\mathbf{q}}^2 = \omega_{s_1}^2(q_1), \quad \tilde{\omega}_{1,s_1,u,\mathbf{q}}^2 = \omega_{s_1}^2(q_1) - 4\phi^2 \sum_{n=1}^{\infty} \frac{\zeta_{2n}^2(q_2)\omega_{2n}^2(q_2)\zeta_{s_1}^2(q_1)\omega_{s_1}^2(q_1)}{\omega_{2n}^2(q_2) - \omega_{s_1}^2(q_2)}.\tag{B.15}$$

The case $j = 2$ is described similarly after change $1 \leftrightarrow 2$ and $2n \rightarrow 2n + 1$ in Eqs. (B.14) and (B.15).

The second group consists of the crosses of two resonant lines (points Γ and W in Fig. 3.3). These points are also the crosses of two high symmetry lines (this is always true). Here the QCB plasmons, generated by the point $\mathbf{k} = \mathbf{q} + \mathbf{m}$ with $\mathbf{q} \equiv (q, q) = (0, 0)$ (Γ point) or $(Q_0/2, Q_0/2)$ (W point), form two quartets. The first quartet is really generated by the point \mathbf{k}_1 . It consists of four symmetrized combinations of single-array states

$$\tilde{\theta}_{s_1, g, \nu, \mathbf{q}} = \theta_{s_1, g, \nu, \mathbf{q}}, \quad \tilde{\theta}_{s_1, u, \nu, \mathbf{q}} = \theta_{s_1, u, \nu, \mathbf{q}} - 2\phi \sum_{s' \neq s_1} \frac{\zeta_{s'}(q_2) \omega_{s'}(q_2) \zeta_{s_1}(q_1) \omega_{s_1}(q_1)}{\omega_{s'}^2(q_2) - \omega_{s_1}^2(q_1)} \theta_{s', u, \nu, \mathbf{q}}, \quad (\text{B.16})$$

where $\nu = g, u$; the band numbers s_1 and s' are even for $q = 0$ and odd for $q = Q/2$;

$$\theta_{s, g/u, g, \mathbf{q}} = \frac{1}{2} \sum_{j=1,2} \left(\theta_{j, s, \mathbf{q}} \pm \theta_{1, s+1, \mathbf{q}} \right); \quad \theta_{s, g/u, u, \mathbf{q}} = \frac{1}{2} \sum_{j=1,2} (-1)^j \left(\theta_{j, s, \mathbf{q}} \pm \theta_{j, s+1, \mathbf{q}} \right).$$

QCB eigenstates of the second quartet are generated by the point \mathbf{k}_2 . They are obtained from the equations (B.16) by replacing $1 \leftrightarrow 2$. Even array eigenstates are degenerate with the frequencies

$$\omega_{s_j, g, g/u, \mathbf{q}}^2 = \omega_{s_j}(q_j)^2, \quad (\text{B.17})$$

while the odd array eigenstates are split

$$\omega_{s_1, u, g/u, \mathbf{q}}^2 = (1 \pm 2\phi) \omega_{s_1}^2(q_1) - 4\phi^2 \sum_{s' \neq s_1} \frac{\zeta_{s'}^2(q_2) \omega_{s'}^2(q_2) \zeta_{s_1}^2(q_1) \omega_{s_1}^2(q_1)}{\omega_{s'}^2(q_2) - \omega_{s_1}^2(q_1)}. \quad (\text{B.18})$$

Equations (B.10) - (B.18) exhaust all cases of QCB plasmons, generated by the point \mathbf{k}_2 lying on a specific line, via the interference of array plasmons.

B.2 AC Conductivity

For interacting wires, where $\zeta_{js}(q_j) \neq 0$, the correlator (3.19) may be easily calculated after diagonalization of the Hamiltonian (3.7) by means of the transformations considered in Appendix B.1. For the first band, for example, these are the transformations (B.5) and (B.6). As a result, one has:

$$\begin{aligned} \left\langle \left[J_{11\mathbf{q}}(t), J_{11\mathbf{q}}^\dagger(0) \right] \right\rangle &= -2ivg \left(u_{\mathbf{q}}^2 \omega_{+,1\mathbf{q}} \sin(\omega_{+,1\mathbf{q}} t) + v_{\mathbf{q}}^2 \omega_{-,1\mathbf{q}} \sin(\omega_{-,1\mathbf{q}} t) \right), \\ \left\langle \left[J_{11\mathbf{q}}(t), J_{21\mathbf{q}}^\dagger(0) \right] \right\rangle &= -2ivgu_{\mathbf{q}} v_{\mathbf{q}} \left(\omega_{-,1\mathbf{q}} \sin(\omega_{-,1\mathbf{q}} t) - \omega_{+,1\mathbf{q}} \sin(\omega_{+,1\mathbf{q}} t) \right). \end{aligned}$$

where $u_{\mathbf{q}}$ and $v_{\mathbf{q}}$ are defined in Eqs.(B.7). Then, for the optical absorption σ' one obtains

$$\sigma'_{11}(\mathbf{q}, \omega) = \pi vg \left[u_{\mathbf{q}}^2 \delta(\omega - \tilde{\omega}_{+,1\mathbf{q}}) + v_{\mathbf{q}}^2 \delta(\omega - \tilde{\omega}_{-,1\mathbf{q}}) \right] \quad (\text{B.19})$$

$$\sigma'_{12}(\mathbf{q}, \omega) = \pi vgu_{\mathbf{q}} v_{\mathbf{q}} \left[\delta(\omega - \tilde{\omega}_{-,1\mathbf{q}}) - \delta(\omega - \tilde{\omega}_{+,1\mathbf{q}}) \right]. \quad (\text{B.20})$$

For quasimomentum \mathbf{q} away from the resonant coupling line, $u_{\mathbf{q}}^2 \approx 1$ and $v_{\mathbf{q}}^2 \sim \phi_{1\mathbf{q}}^2$ for $\Delta_{\mathbf{q}} > 0$ ($v_{\mathbf{q}}^2 \approx 1$ and $u_{\mathbf{q}}^2 \sim \phi_{1\mathbf{q}}^2$ for $\Delta_{\mathbf{q}} < 0$). Then the longitudinal optical absorption (B.19) (i.e. the

absorption within a given set of wires) has its main peak at the frequency $\omega_{+,1\mathbf{q}} \approx v|q_1|$ for $\Delta_{\mathbf{q}} > 0$ (or $\omega_{-,1\mathbf{q}} \approx v|q_1|$ for $\Delta_{\mathbf{q}} < 0$), corresponding to the first band of the pertinent array, and an additional weak peak at the frequency $\omega_{-,1\mathbf{q}} \approx v|q_2|$, corresponding to the first band of a complementary array. It contains also a set of weak peaks at frequencies $\omega_{2,s\mathbf{q}} \approx [s/2]vQ$ ($s = 2, 3, \dots$) corresponding to the contribution from higher bands of the complementary array (in Eq.(B.19) these peaks are omitted). At the same time, a second observable becomes relevant, namely, the transverse optical absorption (B.20). It is proportional to the (small) interaction strength and has two peaks at frequencies $\omega_{+,1\mathbf{q}}$ and $\omega_{-,1\mathbf{q}}$ in the first bands of both sets of wires.

If the quasimomentum \mathbf{q} belongs to the resonant coupling line $\Delta_{\mathbf{q}} = 0$, then $u_{\mathbf{q}}^2 = v_{\mathbf{q}}^2 = 1/2$. In this case the longitudinal optical absorption (B.19) has a split double peak at frequencies $\omega_{+,1\mathbf{q}}$ and $\omega_{-,1\mathbf{q}}$, instead of a single main peak. The transverse optical absorption (B.20), similarly to the non-resonant case (B.20), has a split double peak at frequencies $\omega_{+,1\mathbf{q}}$ and $\omega_{-,1\mathbf{q}}$, but its amplitude is now of the order of unity. For $|\mathbf{q}| \rightarrow 0$ Eq.(B.19) reduces to that for an array of noninteracting wires (3.20), and the transverse optical conductivity (B.20) vanishes.

The imaginary part of the *ac* conductivity $\sigma''_{jj'}(\mathbf{q}, \omega)$ is calculated within the same approach. Its longitudinal component equals

$$\sigma''_{11}(\mathbf{q}, \omega) = \frac{2vg}{\omega} \left[\frac{u_{\mathbf{q}}^2 \omega_{+,1\mathbf{q}}^2}{\omega_{+,1\mathbf{q}}^2 - \omega^2} + \frac{v_{\mathbf{q}}^2 \omega_{-,1\mathbf{q}}^2}{\omega_{-,1\mathbf{q}}^2 - \omega^2} \right].$$

Beside the standard pole at zero frequency, the imaginary part has poles at the resonance frequencies $\omega_{+,1\mathbf{q}}$, $\omega_{-,1\mathbf{q}}$, and an additional series of high band satellites (omitted here). For quasimomenta far from the resonant lines, only the first pole is well pronounced while amplitude of the second one as well as amplitudes of all other satellites is small. At the resonant lines, the amplitudes of both poles mentioned above are equal. The corresponding expression for $\sigma'_{22}(\mathbf{q}, \omega)$ can be obtained by replacement $1 \leftrightarrow 2$.

The transverse component of the imaginary part of the *ac* conductivity has the form:

$$\sigma'_{12}(\mathbf{q}, \omega) = \frac{2vg}{\omega} u_{\mathbf{q}} v_{\mathbf{q}} \left[\frac{\omega_{-,1\mathbf{q}}^2}{\omega^2 - \omega_{-,1\mathbf{q}}^2} - \frac{\omega_{+,1\mathbf{q}}^2}{\omega^2 - \omega_{+,1\mathbf{q}}^2} \right].$$

It always contains two poles and vanishes for noninteracting wires. For quasimomenta far from the resonance lines the transverse component is small while at these lines its amplitude is of the order of unity.

Appendix C

Tilted QCB

C.1 Geometry, Notions and Hamiltonian

A tilted QCB is a $2D$ grid, formed by two periodically crossed arrays of $1D$ quantum wires or carbon nanotubes. Like in a square QCB, arrays are labelled by indices $j = 1, 2$ and wires within the first (second) array are labelled by an integer index n_2 (n_1). The arrays are oriented along the unit vectors $\mathbf{e}_{1,2}$ with an angle φ between them. The periods of a crossbars along these directions are a_1 and a_2 , and the corresponding basic vectors are $\mathbf{a}_j = a_j \mathbf{e}_j$. In experimentally realizable setups, QCB is a cross-structure of suspended single-wall carbon nanotubes lying in two parallel planes separated by an inter-plane distance d . Nevertheless, some generic properties of QCB may be described under the assumption that QCB is a genuine $2D$ system. We choose coordinate system so that the axes x_j and corresponding basic unit vectors \mathbf{e}_j are oriented along the j -th array. The basic vectors of the reciprocal superlattice for a square QCB are $Q_{1,2} \mathbf{g}_{1,2}$, $Q_j = 2\pi/a_j$ so that an arbitrary reciprocal superlattice vector \mathbf{m} is a sum $\mathbf{m} = \mathbf{m}_1 + \mathbf{m}_2$, where $\mathbf{m}_j = m_j Q_j \mathbf{g}_j$, (m_j integer). Here $\mathbf{g}_{1,2}$ are the vectors of the reciprocal superlattice satisfying the standard orthogonality relations $(\mathbf{e}_i \cdot \mathbf{g}_j) = \delta_{ij}$. The first BZ is $|q_{1,2}| \leq Q_{1,2}/2$.

A single wire of j -th array is characterized by its radius r_j , length L_j , and LL interaction parameter g_j . The minimal nanotube radius is 0.35 nm[54], maximal nanotube length is $L = 1$ mm, and the LL parameter is estimated as 0.3 [18]. In typical experimental setup[9] the characteristic lengths mentioned above have the following values

$$d \approx 2 \text{ nm}, \quad L_j \approx 0.1 \text{ mm},$$

so that the inequalities

$$r_{1,2} \ll d \ll a_{1,2} \ll L_{1,2}$$

are satisfied.

The QCB Hamiltonian

$$H = H_1 + H_2 + H_{12}. \quad (\text{C.1})$$

consists of three terms. The first two of them describes LL in the first and second arrays

$$H_1 = \frac{\hbar v_1}{2} \sum_{n_2} \int_{-L_1/2}^{L_1/2} dx_1 \left\{ g_1 \pi_1^2 (x_1, n_2 a_2) + \frac{1}{g_1} (\partial_{x_1} \theta_1 (x_1, n_2 a_2))^2 \right\},$$

$$H_2 = \frac{\hbar v_2}{2} \sum_{n_1} \int_{-L_2/2}^{L_2/2} dx_2 \left\{ g_2 \pi_2^2 (n_1 a_1, x_2) + \frac{1}{g_2} (\partial_{x_2} \theta_2 (n_1 a_1, x_2))^2 \right\}.$$

The inter-array interaction is described by the last term in Eq.(C.1)

$$H_{12} = \frac{2e^2}{d} \sum_{n_1, n_2} \int dx_1 dx_2 \zeta \left(\frac{x_1 - n_1 a_1}{r_1} \right) \zeta \left(\frac{n_2 a_2 - x_2}{r_2} \right) \times \\ \times \partial_{x_1} \theta_1 (x_1, n_2 a_2) \partial_{x_2} \theta_2 (n_1 a_1, x_2). \quad (\text{C.2})$$

It results from a short-range contact capacitive coupling in the crosses of the bars. The dimensionless envelope function (introduced phenomenologically) $\zeta(\xi_j)$ describes re-distribution of a charge in a tube j induced by the interaction with tube i . This function is of order unity for $|\xi| \sim 1$ and vanishes outside this region so that the dimensionless integral

$$\int \zeta(\xi) e^{ikr_j \xi} d\xi \sim 1$$

is of order unity for all $|k|$ smaller than a certain ultraviolet cutoff.

The QCB Hamiltonian (C.1) is a quadratic form in terms of the field operators, so it can be diagonalized exactly. Such a procedure is rather cumbersome. However, due to the separability of the interaction (C.2) the spectrum can be described analytically.

C.2 Spectrum

Now we consider the spectrum of a generic double QCB. The resonance condition (3.18) is fulfilled not at the BZ diagonal but at the resonant polygonal line. Its part *ODE*, lying in the first quarter of the BZ, is displayed in Fig. C.1 (all figures of this Section correspond to the specific values $v_2 Q_2 = 1$, $v_1 Q_1 = 1.4$). This results in qualitative modifications of the spectrum that are related first of all to the appearance of two points *D* and *E* of the three-fold degeneracy for a titled QCB (Fig. C.1) instead of a single point *W* of four-fold degeneracy for a square QCB (Fig. 3.3).

We start with the resonant line *ODE* (Fig. C.2a). The dispersion curves at its *OD* part and the symmetry properties of the corresponding eigenstates are similar to those at the *OC* resonant line for the square QCB (Fig. 3.3). The only difference is that instead of the

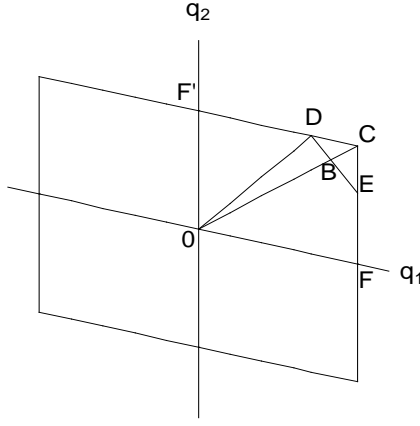


Figure C.1: BZ of a tilted QCB.

four-fold degeneracy at the BZ corner C of the square QCB, there is a three-fold degeneracy at the point D lying at the BZ boundary. A completely new situation takes place at the DE line, where two other modes $(1, 1)$ and $(2, 2)$, corresponding to different arrays and different bands, are degenerate. The interaction lifts this degeneracy and the two middle lines in Fig. C.2a describe even (g) and odd (u) combinations of these modes. The even mode corresponds to the lowest frequency and the odd mode corresponds to the higher one. At the point E one meets another type of a three-fold degeneracy described in more detail in the next paragraph.

Dispersion curves corresponding to quasi momenta lying at the BZ boundary $q_1 = Q_1/2$, $0 \leq q_2 \leq Q_2/2$ (FC line in Fig. C.1) and $q_2 = Q_2/2$, $0 \leq q_1 \leq Q_1/2$ (CF' line in Fig. C.1), are displayed in Fig. C.2b. The lowest and highest curves in the FE part of the latter figure, describe two waves propagating along the second array. They are nearly linear, and deviations from linearity are observed only near the point E where the interaction has a resonant character. Two modes propagating along the first array, in zero approximation, are degenerate with an unperturbed frequency $\omega = 0.7$. The interaction lifts the degeneracy. The lowest of the two middle curves corresponds to $(1, u)$ boson, and the upper of one describes $(1, g)$ boson. Note that $(1, g)$ boson conserves its unperturbed frequency $\omega = 0.7$. The latter fact is related to the symmetry $\zeta_j(\xi) = \zeta_j(-\xi)$ of the separable interaction (3.3). At the point E , the two modes propagating along the first array and the mode propagating along the second array in the second band are degenerate. The interaction lifts the degeneracy, and, as a result, the $(1, u)$ and $(2, 2)$ waves are strongly mixed and the eigen-modes are their even (highest frequency) and odd (lowest frequency) combinations, and the $(1, g)$ mode (middle level).

There are two separate degeneracies within each array at the corner C of a titled QCB BZ. Both of them are related to inter-band mixing conserving array index. The spectral behavior along the CF' boundary of the BZ is similar to that considered above but in the vicinity of the point D of three-fold degeneracy. Here, two modes propagating along the second array

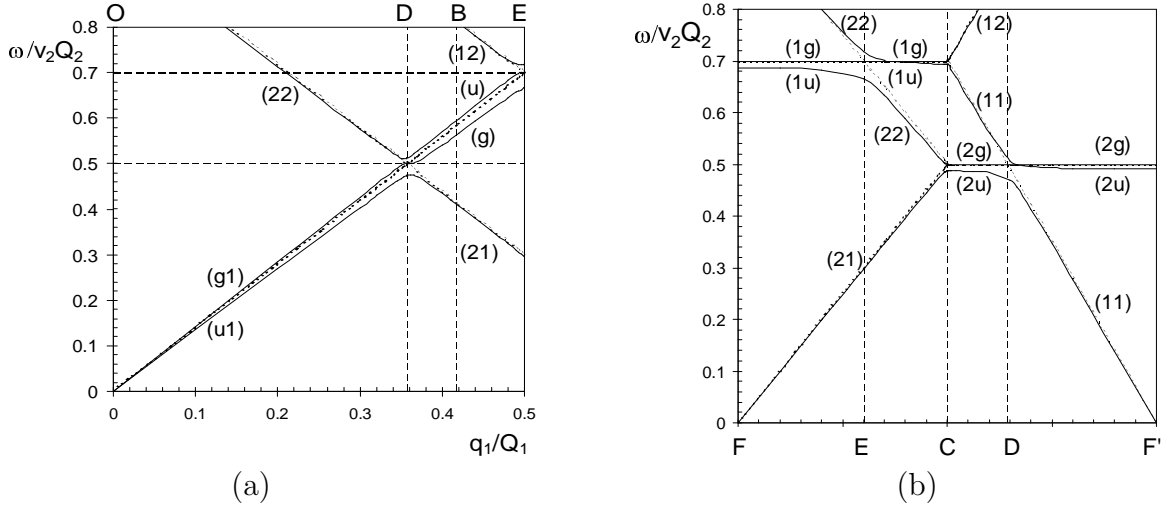


Figure C.2: The energy spectrum of a tilted QCB (solid lines) and noninteracting arrays (dashed lines) for quasimomenta (a) on the resonant line of the BZ (line ODE in Fig. C.1); (b) for quasimomenta at the BZ boundary (line FCF' in the Fig. C.1).

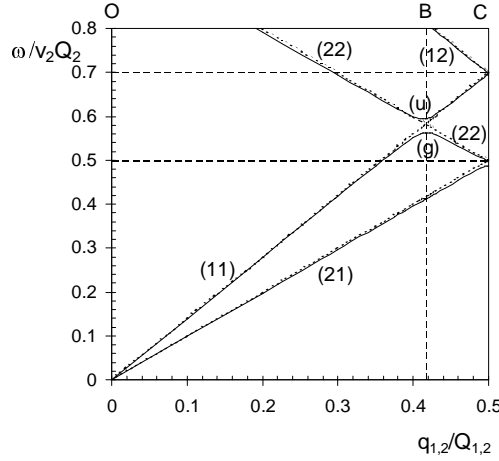


Figure C.3: The energy spectrum of a tilted QCB (solid lines) and noninteracting arrays (dashed lines) for quasimomenta on the BZ diagonal (line OC in Fig. C.1).

in the separable potential approximation (3.10) remain degenerate. This degeneracy is lifted only if deviation from separability is accounted for.

The diagonal OC of a tilted QCB BZ represents a new type of generic line, that crosses a resonant line (Fig. C.3). Here the spectrum mostly conserves its initial systematics, i.e. belongs to a given array, and mostly depends on a given quasimomentum component. However, at the crossing point B , the modes $(1, 1)$ and $(2, 2)$, corresponding to both different arrays and bands, become degenerate (two middle dashed lines in Fig. C.3). Interaction between the wires lifts the degeneracy. The eigenstates of QCB have a definite parity with respect to transposition of these two modes. The lowest and upper of the two middle lines correspond to even (g) and odd (u) mode, respectively.

Like in a square QCB, bosons with quasimomenta close to the resonant lines are strongly mixed bare $1D$ bosons. These excitations are essentially two-dimensional, and therefore lines

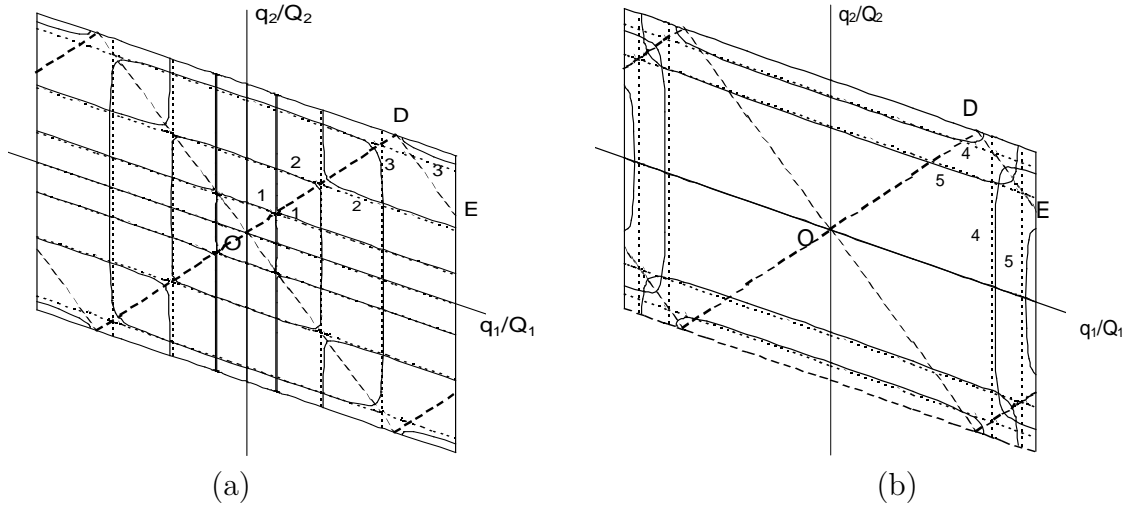


Figure C.4: Lines of equal frequency for a tilted QCB (solid lines) and noninteracting arrays (dashed lines). (a) Lines 1, 2, 3 correspond to frequencies $\omega_1 = 0.1$, $\omega_2 = 0.25$, $\omega_3 = 0.45$. (b) Lines 4, 5 correspond to frequencies $\omega_4 = 0.55$, $\omega_5 = 0.65$.

of equal energy in the vicinity of the resonant lines are modified by the $2D$ interaction (see Figs. C.4a,b). Deviations from $1D$ behavior occur only in this small part of the BZ. For $\omega < 0.5v_2Q_2$ the lines of equal energy within BZ consist of closed line around the BZ center and four open lines (within the extended bands scheme these lines are certainly closed) around the BZ corners (lines 1, 2, 3 in Fig. C.4a). At the line OD in BZ, the modes of QCB are strongly coupled bare bosons propagating along both arrays in the first band.

For $0.5v_2Q_2 < \omega < 0.5v_1Q_1$ (lines 4, 5 in Fig. C.4b) the topology of lines of equal energy is modified. In this case, lines of equal energy within the BZ consist of four open lines. The splitting of lines at the direction DE corresponds to strong coupling of modes propagating along the first array in the first band with those propagating along the second array in the second band.

Appendix D

Triple QCB

D.1 Notions and Hamiltonian

Triple quantum bars is a $2D$ periodic grid with $m = 3$, formed by three periodically crossed arrays $j = 1, 2, 3$ of $1D$ quantum wires. These arrays are placed on three planes parallel to the XY plane and separated by an inter-plane distances d . The upper and the lower arrays correspond to $j = 1, 2$, while the middle array has number $j = 3$. All wires in all arrays are identical. They have the same length L , Fermi velocity v and Luttinger parameter g . The arrays are oriented along the $2D$ unit vectors

$$\mathbf{e}_1 = \left(\frac{1}{2}, \frac{\sqrt{3}}{2} \right), \quad \mathbf{e}_2 = (1, 0), \quad \mathbf{e}_3 = \mathbf{e}_2 - \mathbf{e}_1.$$

The periods of QCB along these directions are equal, $a_j = a$, so we deal with a regular triangular lattice. In what follows we choose $\mathbf{a}_{1,2} = a\mathbf{e}_{1,2}$ as the basic vectors of a superlattice (see Fig. D.1).

The wires within the j -th array are enumerated with the integers n_j . Define $2D$ coordinates along the n_j -th wire \mathbf{r}_j as $\mathbf{r}_j = x_j\mathbf{e}_j + n_j a\mathbf{e}_3$ for upper and lower arrays ($j = 1, 2$) and $\mathbf{r}_3 = x_3\mathbf{e}_3 + n_3 a\mathbf{e}_1$ for the middle array. Here x_j are $1D$ continuous coordinates along the wire. The system of three non-interacting arrays is described by the Hamiltonian

$$H_0 = H_1 + H_2 + H_3,$$

where

$$H_1 = \frac{\hbar v}{2} \sum_{n_1} \int dx_1 \left[g\pi_1^2(x_1\mathbf{e}_1 + n_1 a\mathbf{e}_3) + \frac{1}{g} (\partial_{x_1}\theta_1(x_1\mathbf{e}_1 + n_1 a\mathbf{e}_3))^2 \right], \quad (\text{D.1})$$

$$H_2 = \frac{\hbar v}{2} \sum_{n_2} \int dx_2 \left[g\pi_2^2(x_2\mathbf{e}_2 + n_2 a\mathbf{e}_3) + \frac{1}{g} (\partial_{x_2}\theta_2(x_2\mathbf{e}_2 + n_2 a\mathbf{e}_3))^2 \right], \quad (\text{D.2})$$

$$H_3 = \frac{\hbar v}{2} \sum_{n_3} \int dx_3 \left[g\pi_3^2(x_3\mathbf{e}_3 + n_3 a\mathbf{e}_1) + \frac{1}{g} (\partial_{x_3}\theta_3(x_3\mathbf{e}_3 + n_3 a\mathbf{e}_1))^2 \right], \quad (\text{D.3})$$

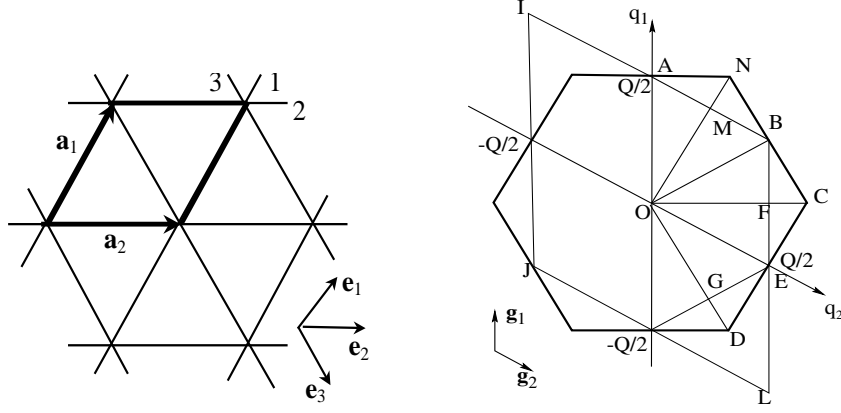


Figure D.1: Triple QCB (left panel). Elementary cell $BIJL$ of the reciprocal lattice and the BZ hexagon of the triple QCB (right panel).

and π_j and $\partial_{x_j}\theta_j$ are canonically conjugate fields describing LL within the j -th array.

Interaction between the excitations in different wires of adjacent arrays j, j' is concentrated near the crossing points with coordinates $n_j\mathbf{a}_j + n_{j'}\mathbf{a}_{j'}$. It is actually Coulomb interaction screened on a distance r_0 along each wire which is described by Hamiltonian

$$H_{int} = H_{13} + H_{23},$$

where

$$H_{j3} = V_0 \sum_{n_j, n_3} \int dx_j dx_3 \Phi \left(\frac{x_j - n_3 a}{r_0} \mathbf{e}_j - \frac{x_3 - n_j a}{r_0} \mathbf{e}_3 \right) \times \\ \times \partial_{x_j} \theta_j (x_j \mathbf{e}_j + n_j a \mathbf{e}_3) \partial_{x_3} \theta_3 (n_3 a \mathbf{e}_j + x_3 \mathbf{e}_3). \quad (\text{D.4})$$

Here the effective coupling strength V_0 is defined by Eq.(3.5), the dimensionless interaction Φ is separable

$$\Phi(\xi_j \mathbf{e}_j + \xi_3 \mathbf{e}_3) = \zeta(\xi_j) \zeta(\xi_3), \quad j = 1, 2, \quad (\text{D.5})$$

and $\zeta(\xi)$ is a dimensionless charge fluctuation in the j -th wire (see Eq. (3.3)).

Such interaction imposes a super-periodicity on the energy spectrum of initially one dimensional quantum wires, and the eigenstates of this superlattice are characterized by a $2D$ quasimomentum $\mathbf{q} = q_1 \mathbf{g}_1 + q_2 \mathbf{g}_2 \equiv (q_1, q_2)$. Here $\mathbf{g}_{1,2}$ are the unit vectors of the reciprocal superlattice satisfying the standard orthogonality relations $(\mathbf{e}_i \cdot \mathbf{g}_j) = \delta_{ij}$, $j = 1, 2$. The corresponding basic vectors of the reciprocal superlattice have the form $Q(m_1 \mathbf{g}_1 + m_2 \mathbf{g}_2)$, where $Q = 2\pi/a$ and $m_{1,2}$ are integers. In Fig. D.1 the elementary cell $BIJL$ of the reciprocal lattice is displayed together with the hexagon of the Wigner-Seitz cell that we choose as the BZ of the triple QCB.

To study the energy spectrum and the eigenstates of the total Hamiltonian

$$H = H_0 + H_{int}, \quad (\text{D.6})$$

we define the Fourier components of the field operators

$$\theta_1(x_1\mathbf{e}_1 + n_1a\mathbf{e}_3) = \frac{1}{\sqrt{NL}} \sum_{s,\mathbf{q}} \theta_{1s\mathbf{q}} e^{i(q_1x_1+q_3n_1a)} u_{s,q_1}(x_1), \quad (\text{D.7})$$

$$\theta_2(x_2\mathbf{e}_2 + n_2a\mathbf{e}_3) = \frac{1}{\sqrt{NL}} \sum_{s,\mathbf{q}} \theta_{2s\mathbf{q}} e^{i(q_2x_2+q_3n_2a)} u_{s,q_2}(x_2), \quad (\text{D.8})$$

$$\theta_3(x_3\mathbf{e}_3 + n_3a\mathbf{e}_1) = \frac{1}{\sqrt{NL}} \sum_{s,\mathbf{q}} \theta_{3s\mathbf{q}} e^{i(q_3x_3+q_1n_3a)} u_{s,q_3}(x_3). \quad (\text{D.9})$$

Here

$$\mathbf{q} = q_1\mathbf{g}_1 + q_2\mathbf{g}_2, \quad q_3 = q_2 - q_1,$$

and $N = L/a$ is the dimensionless length of a wire. In the \mathbf{q} representation, the Hamiltonians H_j (Eqs. (D.1)-(D.3)) and H_{j3} (Eq. (D.4)) can be written as

$$H_j = \frac{\hbar v g}{2} \sum_{s,\mathbf{q}} \pi_{js\mathbf{q}}^+ \pi_{js\mathbf{q}} + \frac{\hbar}{2vg} \sum_{s,\mathbf{q}} \omega_s^2(q_j) \theta_{js\mathbf{q}}^+ \theta_{js\mathbf{q}}, \quad j = 1, 2, 3,$$

$$H_{j3} = \frac{V_0 r_0^2}{2vg} \sum_{s,s',\mathbf{q}} \phi_s(q_3) \phi_{s'}(q_j) \omega_s(q_3) \omega_{s'}(q_j) (\theta_{3s\mathbf{q}}^+ \theta_{js'\mathbf{q}} + h.c.), \quad j = 1, 2,$$

where

$$\omega_s(q) = v \left(\left[\frac{s}{2} \right] Q + (-1)^{s-1} |q| \right), \quad Q = \frac{2\pi}{a},$$

Thus the total Hamiltonian (D.6) describes a system of coupled harmonic oscillators, and can be diagonalized exactly like in the case of double QCB.

D.2 Spectrum

Separability of the interaction (D.5) allows one to derive analytical equations for the spectrum of the total Hamiltonian (D.6). Here we describe the behavior of the spectrum and the corresponding states along some specific lines of the reciprocal space.

To diagonalize the Hamiltonian(D.6), we write down equations of motion

$$[\omega_s^2(q_j) - \omega^2] \theta_{js\mathbf{q}} + \sqrt{\varepsilon} \phi_s(q_j) \omega_s(q_j) \frac{r_0}{a} \sum_{s'} \phi_{s'}(q_3) \omega_{s'}(q_3) \theta_{3s'\mathbf{q}} = 0, \quad (\text{D.10})$$

$$[\omega_s^2(q_3) - \omega^2] \theta_{3s\mathbf{q}} + \sqrt{\varepsilon} \phi_s(q_3) \omega_s(q_3) \frac{r_0}{a} \sum_{j,s'} \phi_{s'}(q_j) \omega_{s'}(q_j) \theta_{js'\mathbf{q}} = 0. \quad (\text{D.11})$$

Here $j = 1, 2$, and ε is defined by Eq.(3.17). The solutions of the set of equations (D.10) - (D.11) have the form:

$$\theta_{js\mathbf{q}} = A_j \frac{\phi_s(q_j) \omega_s(q_j)}{\omega_s^2(q_j) - \omega^2}, \quad j = 1, 2, 3.$$

Substituting this equation into Eqs.(D.10) and (D.11), we have three equations for the constants A_j :

$$A_1 + A_3\sqrt{\varepsilon}F_{q_3}(\omega^2) = 0, \quad A_2 + A_3\sqrt{\varepsilon}F_{q_3}(\omega^2) = 0, \quad A_3 + \sum_{j=1,2} A_j\sqrt{\varepsilon}F_{q_j}(\omega^2) = 0,$$

where

$$F_q(\omega^2) = \frac{r_0}{a} \sum_s \frac{\phi_s^2(q)\omega_s^2(q)}{\omega_s^2(q) - \omega^2}.$$

Dispersion relations can be obtained from the solvability condition for this set of equations

$$\varepsilon F_{q_3}(\omega^2) (F_{q_1}(\omega^2) + F_{q_2}(\omega^2)) = 1.$$

The function $F_{q_s}(\omega^2)$ has a set of poles at $\omega^2 = \omega_s^2(q)$, $s = 1, 2, 3, \dots$. For $\omega^2 < \omega_s^2(q)$, i.e. within the interval $[0, \omega_1^2(q)]$, $F_{q_s}(\omega^2)$ is positive increasing function. Its minimal value F on the interval is reached at $\omega^2 = 0$ and does not depend on the quasi-momentum q

$$F_q(0) = \frac{r_0}{a} \sum_s \phi_s^2(q) = \int d\xi \zeta_j^2(\xi) \equiv F.$$

If the parameter $\varepsilon \equiv \eta^2$ is smaller than the critical value

$$\varepsilon_c = \frac{1}{2F^2},$$

then all the solutions ω^2 of the characteristic equation are positive. When ε increases, the lowest QCB mode softens and its square frequency vanishes *in the whole BZ* at $\varepsilon = \varepsilon_c$. For the exponential interaction model $\zeta(\xi) = \exp(-|\xi|)$, one obtains $\varepsilon_c \approx 1$.

The high symmetry of the triple QCB leads to a number of lines where inter-array or inter-band resonant interaction occurs: *all* lines in Fig. D.1 possess some resonant properties. These lines may be classified as follows:

On the Bragg lines where one of the three array wave-numbers q_j is a multiple integer of $Q/2$, there is a strong intra-band mixing of modes of the j -th array. In Fig. D.1, these lines are the boundaries of the elementary cell of the reciprocal lattice *IJLB*, axes q_1 and q_2 , lines *OB* and *EH*. In particular, along the lines *OA* ($q_2 = 0$) and *OB* ($q_3 = 0$) two modes corresponding to the second and third bands and to the second (*OA*) or third (*OB*) array are mixed. Along the line *AB* ($q_1 = Q/2$) the same mixing occurs between (1, 1) and (1, 2) modes. Moreover, the resonant mixing of different arrays within the same band occurs along the medians *OA*, *OB*, etc. There are two types of such resonance. The first one (e.g., *OA* line) is the resonance between neighboring arrays ($q_1 = -q_3$) and therefore it is of the main order with respect to interaction. The second one (e.g., *OB* line) is the resonance between remote arrays ($q_1 = q_2$) and it is one order smaller.

The second family consists of resonant lines formed by the BZ hexagon boundaries and diagonals. Thus, the diagonal *OC* realizes a first order resonance between the first and the

third arrays $q_1 = q_3$, and the BZ boundaries HD and AN correspond to the same resonance up to an umklapp process ($q_1 = q_3 - Q$ and $q_1 = q_3 + Q$ respectively). Along the diagonal OD and the BZ boundary NC a second order resonance takes place with resonance conditions $q_2 = -q_1$ and $q_2 = -q_1 + Q$ respectively.

In the reciprocal space of the triple QCB there are four different types of crossing points. Two of them include the bases of BZ medians (e.g., points A , B , E and so on). Here one deals with the four-fold degeneracy of the modes corresponding to the first order resonance between the neighboring arrays (e.g., point A , $\omega_{1,s} = \omega_{3,s'}$, $s, s' = 1, 2$), or to the second order resonance between remote arrays (like point B , $\omega_{1,s} = \omega_{2,s'}$, $s, s' = 1, 2$). One more family consists of crossing points of the BZ diagonals and the lines connecting the bases of its medians (points M , F , G and so on). Here one deals with three types of two-fold degeneracy simultaneously. For example, at the point M two separate pairs of modes corresponding to neighboring arrays $(2, 1)$, $(3, 1)$, and $(2, 2)$, $(3, 2)$, are degenerate, as well as two modes corresponding to the first array, $(1, 1)$, $(1, 2)$. Finally the BZ hexagon vertices form the most interesting group of points where the three-fold degeneracy between modes corresponding to all three arrays takes place. The typical example of such a point is the vertex C where the resonance condition $q_1 = -q_2 + Q = q_3 = Q/3$ is satisfied.

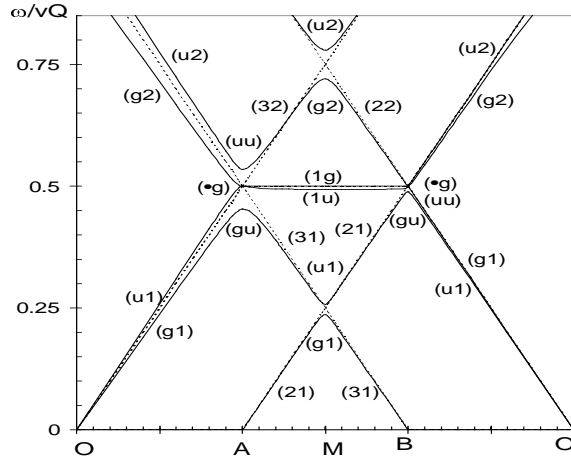


Figure D.2: Dispersion curves at the $OAMBO$ polygon of BZ.

Almost all these peculiarities of the triple QCB spectrum can be illustrated in Fig. D.2 where the dispersion curves along the closed line $OABO$ are displayed. We emphasize once more that in the infrared limit $\omega, \mathbf{q} \rightarrow 0$ triple QCB like double QCB preserves the characteristic LL properties of the initial arrays.

D.3 Observables

The structure of the energy spectrum analyzed above strongly influences optical and transport properties of the triple QCB. As in the case of double QCB (part 3.6), one expects

to observe four peaks of the optical absorption near the points A, B, E, H of the four-fold degeneracy. Then, specific features of space correlators like those considered in D.2 can be observed. But the most pronounced manifestation of a triangular symmetry of the triple QCB are its Rabi oscillations.

Consider the vicinity of the point C of the BZ of three-fold degeneracy, mixing all three arrays,

$$q_1 = q_3 = -q_2 + Q = \frac{Q}{3}, \quad \omega_{11}(Q/3) = \omega_{21}(2Q/3) = \omega_{31}(Q/3) \equiv \omega_0.$$

Equations of motion at this point in the resonance approximation read

$$\left[\frac{d^2}{dt^2} + \omega_0^2 \right] \theta_j + \sqrt{\varepsilon} \phi^2 \omega_0^2 \theta_3 = 0, \quad \left[\frac{d^2}{dt^2} + \omega_0^2 \right] \theta_3 + \sqrt{\varepsilon} \phi^2 \omega_0^2 (\theta_1 + \theta_2) = 0,$$

where $\theta_j \equiv \theta_{j\mathbf{q}}$. General solution of this system looks as

$$\begin{pmatrix} \theta_1(t) \\ \theta_2(t) \\ \theta_3(t) \end{pmatrix} = \theta_0 \begin{pmatrix} 1 \\ -1 \\ 0 \end{pmatrix} e^{i\omega_0 t} + \theta_+ \begin{pmatrix} 1 \\ 1 \\ \sqrt{2} \end{pmatrix} e^{i\omega_+ t} + \theta_- \begin{pmatrix} 1 \\ 1 \\ -\sqrt{2} \end{pmatrix} e^{i\omega_- t},$$

where one of the eigenfrequencies coincides with ω_0 , while the other two are

$$\omega_{\pm} = \omega_0 \sqrt{1 \pm \sqrt{2} \phi^2},$$

and $\theta_{0,\pm}$ are the corresponding amplitudes.

Choosing initial conditions $\theta_1(0) = i\theta_0$, $\dot{\theta}_1(0) = \omega_0 \theta_0$, $\theta_2(0) = \theta_3(0) = 0$, $\dot{\theta}_2(0) = \dot{\theta}_3(0) = 0$, we obtain for the field amplitudes at the coordinate origin

$$\begin{aligned} \theta_1(0, 0; t) &= \frac{\theta_0}{4} \left[\frac{\omega_0}{\omega_+} \sin(\omega_+ t) + \frac{\omega_0}{\omega_-} \sin(\omega_- t) \right] + \frac{\theta_0}{2} \sin(\omega_0 t), \\ \theta_2(0, 0; t) &= \frac{\theta_0}{4} \left[\frac{\omega_0}{\omega_+} \sin(\omega_+ t) + \frac{\omega_0}{\omega_-} \sin(\omega_- t) \right] - \frac{\theta_0}{2} \sin(\omega_0 t), \\ \theta_3(0, 0; t) &= \frac{\theta_0}{2\sqrt{2}} \left[\frac{\omega_0}{\omega_+} \sin(\omega_+ t) - \frac{\omega_0}{\omega_-} \sin(\omega_- t) \right]. \end{aligned}$$

In the limiting case $\varepsilon \ll 1$ these formulas lead to the following time dependence of the field operators in the coordinate origin in real space

$$\begin{aligned} \theta_1(0, 0; t) &= \theta_0 \sin(\omega_0 t) \cos^2 \left(\frac{\sqrt{2\varepsilon} \phi^2}{4} \omega_0 t \right), \\ \theta_2(0, 0; t) &= \theta_0 \cos(\omega_0 t) \sin^2 \left(\frac{\sqrt{2\varepsilon} \phi^2}{4} \omega_0 t \right), \\ \theta_3(0, 0; t) &= \theta_0 \sin(\omega_0 t) \cos \left(\frac{\sqrt{2\varepsilon} \phi^2}{2} \omega_0 t \right). \end{aligned} \tag{D.12}$$

The field operators of all three arrays demonstrate fast oscillations with the resonant frequency ω_0 modulated by a slow frequency. It is the same for the two remote arrays, and doubled for the intermediate array. These beatings are synchronized in a sense that zero intensity on the intermediate array always coincides with the same intensity on one of the remote arrays. At these moments all the energy is concentrated solely within one of the remote arrays. These peculiar Rabi oscillations are displayed in Fig. D.3.

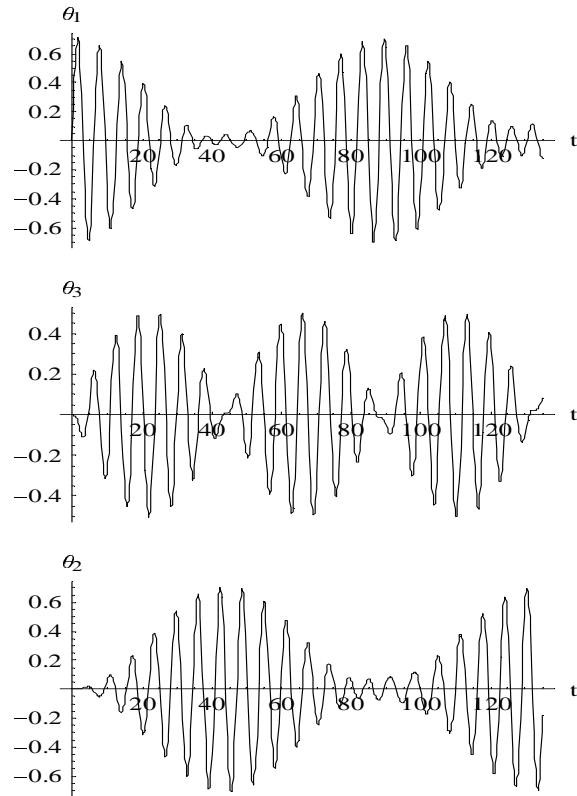


Figure D.3: Periodic energy transfer between three arrays at the triple resonant point C of the BZ.

Appendix E

Derivation of QCB-Light Interaction Hamiltonian

Light scattering on QCB is described by equations (6.1) - (6.7). In this Appendix we briefly explain the main steps which lead to such a description.

1. Nanotube-light interaction, Eq. (6.1). We start with a consideration of a single nanotube of the first array, interacting with an external electromagnetic field. The characteristic time of all nanotube energies, including Coulomb interaction, is of order of an inverse plasmon frequency. The scattering process occurs during much shorter time interval, which is of the order of an inverse photon frequency. Hence, Coulomb interaction is irrelevant for the scattering processes. This enables us to restrict ourselves by a kinetic part of the nanotube Hamiltonian. Within the $\mathbf{k} - \mathbf{p}$ approximation, this part is given by [49]

$$h_{kin} = v_F \int \frac{dx_1 d\gamma}{2\pi} \psi_\alpha^\dagger(x_1, r_0, \gamma) \hbar \mathbf{k} \cdot \vec{\sigma}_{\alpha, \alpha'} \psi_{\alpha'}(x_1, r_0, \gamma). \quad (\text{E.1})$$

In the presence of a magnetic field, one should add $e\mathbf{A}/c$ to the electron momentum operator $\hbar\mathbf{k}$. *An additional part of the Hamiltonian* (E.1) exactly coincides with the nanotube-light interaction Hamiltonian(6.1).

The Hamiltonian (E.1) is diagonalized by a two step canonical transformation. The first one is Fourier transformation

$$\psi_\alpha(x_1, \gamma) = \frac{1}{\sqrt{L}} \sum_{k,m} c_{\alpha,k,m} e^{ikx_1 + im\gamma}, \quad (\text{E.2})$$

where the orbital moment m is restricted by the condition $|m| \leq m_0 = [\pi r_0/a_0]$ due to the finite number of honeycomb cells along the nanotube perimeter ($a_0\sqrt{3}$ is the lattice constant). The second rotation is defined as

$$c_{p,k,m} = \frac{1}{\sqrt{2}} (c_{Akm} + p e^{i\phi_m} c_{Bkm}), \quad p = \pm,$$

where

$$\cos \phi_m = \frac{kr_0}{\sqrt{(kr_0)^2 + m^2}}, \quad \sin \phi_m = \frac{m}{\sqrt{(kr_0)^2 + m^2}}.$$

As a result, the Hamiltonian takes the form

$$H_{kin} = \sum_{p,k,m} \hbar\omega_p(k, m) c_{pkm}^\dagger c_{pkm} \quad (\text{E.3})$$

with eigenfrequencies

$$\omega_p(k, m) = pv_F \sqrt{k^2 + \frac{m^2}{r_0^2}}. \quad (\text{E.4})$$

2. QCB-light interaction, Eq. (6.3). Substituting into Eq. (6.1) the scalar product $\mathbf{A} \cdot \vec{\sigma}$ in the form

$$(\mathbf{A} \cdot \vec{\sigma}) = \begin{pmatrix} 0 & A^- \\ A^+ & 0 \end{pmatrix},$$

where $A^\pm = A_1 \pm iA_\gamma$, we can write the nanotube-light interaction as

$$H_{nl} = \frac{ev_F}{c} \int \frac{dx_1 d\gamma}{2\pi} \left(\psi_A^\dagger A^- \psi_B + h.c. \right).$$

We are interested in an effective QCB-light interaction Hamiltonian obtained in second order of perturbation theory which describes transitions between initial states $|i\rangle$ and final ones $|f\rangle$. Initial states are one-photon states of the electromagnetic field and the electron ground state of the nanotube whereas final states consist of one photon and an electron above the Fermi level. It will be seen later that just these states form a one-plasmon array state. The energy of the incident photon $E = \hbar ck$ is much higher than the excitation energies of the nanotube. Therefore, absorption of the incident photon and radiation of the scattered photon occur practically without retardation. All this results in the interaction Hamiltonian

$$h_{int} = \frac{e^2}{\hbar c} \left(\frac{v_F}{c} \right)^2 \int \frac{dx_1 d\gamma}{2\pi} \int \frac{dx'_1 d\gamma'}{2\pi} \sum_{|v\rangle} \frac{1}{k} \left(\psi_A^\dagger(x'_1, \gamma') A^-(x'_1, 0, 0) \times \right. \\ \left. |v\rangle \langle v| \psi_B(x'_1, \gamma') \psi_B^\dagger(x_1, \gamma) |v\rangle \langle v| A^+(x_1, 0, 0) \psi_A(x_1, \gamma) + A \leftrightarrow B \right), \quad (\text{E.5})$$

which corresponds to the diagram shown in Fig. 6.1a (there is no photons in an intermediate state).

Consider now the matrix element $\langle v| \psi_\alpha(x'_1, \gamma') \psi_\alpha^\dagger(x_1, \gamma) |v\rangle$ which enters this Hamiltonian. Due to our choice of initial and final states, only diagonal elements with respect to both virtual states $|v\rangle$ and sublattice indices α survive. In the $c_{\alpha,k,m}$ representation (E.2), they have the form

$$\langle v| \psi_\alpha(x'_1, \gamma') \psi_\alpha^\dagger(x_1, \gamma) |v\rangle = \frac{1}{L} \sum_{k,k'} \sum_{m,m'} \langle v| c_{\alpha,k,m} c_{\alpha,k',m'}^\dagger |v\rangle e^{ikx_1 - ik'x'_1 + im\gamma - im'\gamma'}.$$

Internal matrix elements on the r.h.s. of the latter equation are

$$\langle v| c_{\alpha,k,m} c_{\alpha,k',m'}^\dagger |v\rangle = \frac{1}{2} \delta_{k,m} \delta_{k',m'}$$

(here the symmetry property $n(E_-(k, m)) + n(E_+(k, m)) = 1$ is used). Therefore

$$\langle v | \psi_\alpha(x'_1, \gamma') \psi_\alpha^\dagger(x_1, \gamma) | v \rangle = \pi \delta(x_1 - x'_1) S(\gamma - \gamma'),$$

where

$$S(\gamma) = \frac{1}{2\pi} \sum_{m=-m_0}^{m_0} e^{im\gamma}.$$

Thus, the interaction (E.5) takes the form

$$h_{int} = \frac{e^2}{\hbar c} \left(\frac{v_F}{c} \right)^2 \int \frac{dx_1 d\gamma d\gamma'}{4\pi k} S(\gamma - \gamma') A^-(x_1, 0, 0) A^+(x_1, 0, 0) \sum_{\alpha} \psi_\alpha^\dagger(x_1, \gamma') \psi_\alpha(x_1, \gamma).$$

The field dependent factor here is

$$A^-(x_1, 0, 0) A^+(x_1, 0, 0) = A_1^2(x_1, 0, 0) + A^2(x_1, 0, 0) \sin(\gamma_A - \gamma') \sin(\gamma_A - \gamma), \quad (\text{E.6})$$

and (A_1, A, γ) are cylindrical components of the vector potential \mathbf{A} (6.2). Taking into account the angular dependence of the field (E.6), we can omit it in the electron operators. Indeed, according to Eq. (E.4) (see also Fig. 2.3) in an energy-momentum region where we work, the $m = 1$ spectral band with nonzero orbital moment is separated from that with $m = 0$ by an energy of order of $\hbar v_F / r_0$, which is much higher than the QCB plasmon energy. Keeping only the zero moment field operators which form the electron density operator

$$\sum_{\alpha} \psi_\alpha^\dagger(x_1) \psi_\alpha(x_1) = \rho(x_1) \equiv \sqrt{2} \partial_{x_1} \theta(x_1),$$

and integrating over γ, γ' , we obtain an interaction Hamiltonian in form

$$h_{int} = \frac{\sqrt{2} e^2}{4k \hbar c} \left(\frac{v_F}{c} \right)^2 \int dx_1 \partial_{x_1} \theta(x_1) \mathbf{A}_1^2(x_1, 0, 0), \quad (\text{E.7})$$

where

$$\mathbf{A}_1 = \mathbf{A} + (\sqrt{2} - 1) A_1 \mathbf{e}_1.$$

Straightforward generalization of this expression to the QCB case leads exactly to the Hamiltonian (6.3).

3. Polarization matrix, Eq. (6.7). To study the scattering process, we should modify the last expression for the interaction Hamiltonian. To proceed further, we define Fourier transforms θ_{j, \mathbf{Q}_j} of the bosonic fields

$$\begin{aligned} \theta_1(x_1, n_2 a) &= \frac{1}{\sqrt{NL}} \sum_{\mathbf{k}_1} \theta_{1, -\mathbf{k}_1} e^{-ik_1 x_1 - iq_2 n_2 a}, \\ \theta_2(n_1 a, x_2) &= \frac{1}{\sqrt{NL}} \sum_{\mathbf{k}_2} \theta_{2, -\mathbf{k}_2} e^{-iq_1 n_1 a - ik_2 x_2}. \end{aligned} \quad (\text{E.8})$$

Here $N = L/a$ is the number of QCB cells in both directions. The electromagnetic field also can be expanded in a sum of harmonics with a wave vector \mathbf{k} and polarization $\lambda = \parallel, \perp$,

$$\mathbf{A}(\mathbf{r}) = \sum_{\mathbf{K}\lambda} \mathbf{n}_{\mathbf{K}\lambda} A_{\mathbf{K}\lambda} e^{i\mathbf{K}\mathbf{r}}. \quad (\text{E.9})$$

The polarization vectors

$$\begin{aligned} \mathbf{n}_{\mathbf{K}\parallel} &= \frac{iK_2\mathbf{e}_1}{\sqrt{K_1^2 + K_2^2}} - \frac{iK_1\mathbf{e}_2}{\sqrt{K_1^2 + K_2^2}}, \\ \mathbf{n}_{\mathbf{K}\perp} &= \frac{K_1K_3\mathbf{e}_1}{K\sqrt{K_1^2 + K_2^2}} + \frac{K_2K_3\mathbf{e}_1}{K\sqrt{K_1^2 + K_2^2}} - \frac{\sqrt{K_1^2 + K_2^2}}{K}\mathbf{e}_3, \end{aligned}$$

are normalized, $|\mathbf{n}_{\mathbf{K}\lambda}| = 1$, and satisfy the orthogonality conditions, $\mathbf{n}_{\mathbf{K}\lambda} \cdot \mathbf{K} = \mathbf{n}_{\mathbf{K}\parallel} \cdot \mathbf{n}_{\mathbf{K}\perp} = 0$. The field operators $A_{\mathbf{K}\lambda}$ satisfy the condition $A_{\mathbf{K}\lambda}^\dagger = A_{-\mathbf{K}\lambda}$, so that $\mathbf{A}^\dagger(\mathbf{r}) = \mathbf{A}(\mathbf{r})$.

Substituting equations (E.8), and (E.9) into the Hamiltonian (6.3), we obtain

$$H_{int} = -i \frac{\sqrt{2NL}}{4} \frac{e^2}{\hbar c} \left(\frac{v_F}{c} \right)^2 \sum_{\mathbf{K}, \mathbf{K}', \mathbf{k}} \sum_{j, \lambda, \lambda'} P_{j; \lambda', \lambda} \left(\frac{\mathbf{K}'}{K'}, \frac{\mathbf{K}}{K} \right) \frac{k_j}{K} A_{\mathbf{K}', \lambda'}^\dagger A_{\mathbf{K}, \lambda} \theta_{j, -\mathbf{k}_j}. \quad (\text{E.10})$$

Here

$$P_{j; \lambda', \lambda} \left(\frac{\mathbf{K}'}{K'}, \frac{\mathbf{K}}{K} \right) = (\vec{\kappa}_{j, \mathbf{K}', \lambda'}^* \cdot \vec{\kappa}_{j, \mathbf{K}, \lambda}) \quad (\text{E.11})$$

is the polarization matrix, $\mathbf{k} = \mathbf{q} + \mathbf{m}$, and

$$\vec{\kappa}_{j, \mathbf{K}, \lambda} = \mathbf{n}_{\mathbf{K}\lambda} + (\sqrt{2} - 1) (\mathbf{n}_{\mathbf{K}\lambda} \cdot \mathbf{e}_j) \mathbf{e}_j.$$

In the case of normal incidence, Eqs. (E.11), (E.12) result in form (6.7) of polarization matrix.

4. Scattering Hamiltonian, Eq. (6.6). In the next step, we express the Fourier transforms of the Bose fields θ via creation (a^\dagger) and annihilation (a) operators of the array plasmons

$$\theta_{j, -\mathbf{k}_j} = \sqrt{\frac{g}{2|k_j|}} (a_{j, -\mathbf{k}_j} + a_{j, \mathbf{k}_j}^\dagger).$$

The electromagnetic field amplitudes $A_{\mathbf{K}, \lambda}$ should also be expressed via photon creation (c^\dagger) and annihilation (c) operators

$$A_{\mathbf{K}, \lambda}(t) = \sqrt{\frac{\hbar c}{2VK}} (c_{\mathbf{K}, \lambda} + c_{-\mathbf{K}, \lambda}^\dagger).$$

Substituting these expansions into Eq. (E.10) we obtain the final form of the effective interaction. *In the case of normal incidence, this interaction is written as*

$$H_{int} = \frac{i\sqrt{gNL}}{V} \left(\frac{ev_F}{2cK} \right)^2 \sum_{\mathbf{K}, \mathbf{K}'} \sum_{j, \lambda, \lambda'} h_{\lambda', \lambda}(\mathbf{k}') c_{\mathbf{K}', \lambda'}^\dagger c_{\mathbf{K}, \lambda}, \quad (\text{E.12})$$

where $h_{\lambda', \lambda}(\mathbf{K}')$ is the Hamiltonian (6.6), where $\lambda_f, \lambda_i, \mathbf{K}$ are replaced by $\lambda', \lambda, \mathbf{K}'$.

5. Scattering cross section, Eqs. (6.4) - (6.5). Standard procedure based on the Fermi golden rule leads to the following expression of the differential scattering cross section per unit QCB square

$$\frac{1}{L^2} \frac{d\sigma}{d\omega do} = \frac{1}{\pi} \left(\frac{V k_f}{L c \hbar} \right)^2 \overline{|\langle f | H_{int} | i \rangle|^2} \delta \left(\frac{\varepsilon_i - \varepsilon_f}{\hbar} \right) \quad (\text{E.13})$$

(here bar denotes averaging with respect to polarization of both incident light and scattered quanta). Choose an initial ket-state $|i\rangle$ such that it contains an incident photon with momentum \mathbf{K}_i , frequency $\Omega_i = cK_i$, and polarization λ_i , and does not contain any QCB plasmon. This state can be written as $|i\rangle = |\mathbf{K}_i\rangle_l \otimes |0\rangle_p$, where $|0\rangle_p$ is the plasmon vacuum, $|\mathbf{K}_i\rangle_l = c_{\mathbf{K}_i, \lambda_i}^\dagger |0\rangle_l$, and $|0\rangle_l$ is the photon vacuum. A final bra-state $\langle f|$ contains a scattered photon with momentum \mathbf{K}_f , frequency $\Omega_f = cK_f$, and polarization λ_f . It contains also a QCB plasmon P with the frequency ω_P (its quantum numbers will be specified below). The final state is written as $\langle f| = \langle P| \otimes \langle \mathbf{K}_f|$, where $\langle \mathbf{K}_f| = \left(c_{\mathbf{K}_f, \lambda_f}^\dagger |0\rangle_l \right)^\dagger$.

A matrix element of the interaction which enters Eq. (E.13), is

$$\langle f | H_{int} | i \rangle = \langle P | \overline{H}_{int} | 0 \rangle_p, \quad (\text{E.14})$$

where

$$\begin{aligned} \overline{H}_{int} &\equiv \langle \mathbf{K}_f, \lambda_f | H_{int} | \mathbf{K}_i, \lambda_i \rangle = -\frac{i\sqrt{gNL}}{V} \left(\frac{ev_F}{2cK} \right)^2 \sum_{j, \mathbf{k}} \frac{k_j}{\sqrt{|k_j|}} \delta_{\mathbf{K}_f, \mathbf{K}_i - \mathbf{k}} \times \\ &\times P_{j; \lambda_f, \lambda_i} \left(\frac{\mathbf{K}_f}{K_f}, \frac{\mathbf{K}_i}{K_i} \right) \left(a_{j, -\mathbf{k}_j} + a_{j, \mathbf{k}_j}^\dagger \right), \end{aligned} \quad (\text{E.15})$$

where $\mathbf{K}_{i, f}^\parallel = \mathbf{K}_{i, f} - (\mathbf{K}_{i, f} \cdot \mathbf{e}_3) \mathbf{e}_3$. In the case of normal incidence Eqs. (E.13) - (E.15) are equivalent to Eqs. (6.3) - (6.6).

Bibliography

- [1] J. Voit, Rep. Prog. Phys. **58**, 977 (1994).
- [2] L.D. Landau, Sov. Phys. JETP, **3**, 920 (1957).
- [3] L.D. Landau, Sov. Phys. JETP, **8**, 70 (1959).
- [4] L.S. Levitov, A.M. Tsvelik, Phys. Rev. Lett. **90**, 016401 (2003).
- [5] P.W. Anderson, Science **235**, 1196 (1987).
- [6] M.R. Diehl, S.N. Yaliraki, R.A. Beckman, M. Barahona, and J.R. Heath, Angew. Chem. Int. Ed. **41**, 353 (2002).
- [7] B.Q. Wei, R. Vajtai, Y. Jung, J. Ward, R. Zhang, G. Ramanath, and P. M. Ajayan, Nature **416**, 495 (2002).
- [8] Y. Luo, C.P. Collier, J.O. Jeppesen, K.A. Nielsen, E. Delonno, G. Ho, J. Perkins, H-R. Tseng, T. Yamamoto, J.F. Stoddardt, J.R. Heath, Chem. Phys. Chem. **3**, 519 (2002).
- [9] T. Rueckes, K. Kim, E. Joselevich, G. Y. Tseng, C. L. Cheung, and C. M. Lieber, Science **289**, 94 (2000).
- [10] H. Dai, Surface Science, **500**, 218 (2002).
- [11] A.B. Dalton, S. Collins, E. Muñoz, J.M. Razal, V.H. Ebron, J.P. Ferraris, J.N. Coleman, B.G. Kim, and R.H. Baughman, Nature **423**, 703 (2003).
- [12] G.Y. Tseng and J.C. Ellenbogen, Science **294**, 1293 (2001).
- [13] J. E. Avron, A. Raveh, and B. Zur, Rev. Mod. Phys. **60**, 873 (1988).
- [14] Y. Avishai, and J. M. Luck, Phys. Rev. B **45**, 1074 (1992).
- [15] F. Guinea, and G. Zimanyi, Phys. Rev. B **47**, 501 (1993).
- [16] R. Mukhopadhyay, C.L. Kane, and T. C. Lubensky, Phys. Rev. B **63**, 081103(R) (2001).

- [17] M. Bockrath, D.H. Cobden, J. Lu, A.G. Rinzler, R.E. Smalley, L. Balents, P.L. McEuen, *Nature* **397**, 598 (1999).
- [18] R. Egger, A. Bachtold, M.S. Fuhrer, M. Bockrath, D.H. Cobden, and P.L. McEuen, in *Interacting Electrons in Nanostructures*, p. 125, R. Haug, and H. Schoeller (Eds.), Springer (2001).
- [19] X. G. Wen, *Phys. Rev. B* **42**, 6623 (1990).
- [20] H. J. Schultz, *Int. J. Mod. Phys.* **1/2**, 57 (1991).
- [21] V.J. Emery, E. Fradkin, S.A. Kivelson, and T.C. Lubensky, *Phys. Rev. Lett.* **85**, 2160 (2000).
- [22] A. Vishwanath and D. Carpentier, *Phys. Rev. Lett.* **86**, 676 (2001).
- [23] R. Mukhopadhyay, C. L. Kane, and T. C. Lubensky, *Phys. Rev. B* **64**, 045120 (2001).
- [24] C.S. Hern, T.C. Lubensky, and J. Toner, *Phys. Rev. Lett.* **83**, 2745 (1999).
- [25] S.L. Sondhi and K. Yang, *Phys. Rev. B* **63** 054430 (2001).
- [26] C.L. Kane, R. Mukhopadhyay, and T.C. Lubensky, *Phys. Rev. Lett.* **88**, 036401 (2002).
- [27] A.H. Castro Neto and F. Guinea, *Phys. Rev. Lett.* **80**, 4040 (1998).
- [28] E. Buchstab, A.V. Butenko, and V.V. Pilipenko, *Sov. J. Low Temp. Phys.* **11**, 357 (1985).
- [29] E. Buchstab, A.V. Butenko, N.Ya. Fogel, V.G. Cherkasova, and R.L. Rosenbaum, *Phys. Rev. B* **50**, 10063 (1994).
- [30] G. Mihaly, I. Kezsmarki, F. Zambroszky, and L. Forro, *Phys. Rev. Lett.* **84**, 2670 (2000).
- [31] Y. Maeno, H. Hashimoto, K. Yoshida, S. Nishizaki, T. Fujita, J.G. Bednorz, and F. Lichtenberg, *Nature* **372**, 532 (1994).
- [32] I. Terasaki, Y. Sasago, and K. Uchinokura, *Phys. Rev. B* **63** R12685 (1997).
- [33] S.M. Loureiro, D.P. Young, R.J. Cava, R. Jin, Y. Liu, P. Bordet, Y. Qin, H. Zandbergen, M. Godinho, M. Núñez-Regueiro, and B. Batlogg, *Phys. Rev. B* **63** 094109 (2001).
- [34] I. Tsukada, T. Yamamoto, M. Takagi, T. Tsubone, S. Konno, and K. Uchinokura, cond-mat/0012395, to be published in *J. Phys. Soc. Jpn.*
- [35] T. Valla, P.D. Johnson, Z. Yusof, B. Wells, Q. Li, S.M. Loureiro, R.J. Cava, M. Mikami, Y. Mori, M. Yoshimura, and T. Sasaki, *Nature* **417**, 627 (2002).

- [36] S. Tomonaga, Prog. Theor. Phys. (Kyoto), **5**, 544 (1950).
- [37] J.M. Luttinger, J. Math. Phys. **4**, 1153 (1963).
- [38] J. von Delft and H. Schoeller, Ann. der Physik **7**, 225 (1998).
- [39] C.L. Kane, M.P.A. Fisher, Phys. Rev. B **46**, 15233 (1992).
- [40] U. Meirav, M.A. Kastner, M. Heiblum, and S.J. Wind, Phys. Rev. B **40**, 5871 (1989).
- [41] G. Timp, in *Mesoscopic Phenomena in Solids*, edited by B.L. Altshuler, P.A. Lee, and R.A. Webb (Elsevier, Amsterdam, 1990).
- [42] S.V. Zaitsev-Zotov, Yu.A. Kumzerov, Yu.A. Firsov, and P. Monceau, J. Phys.: Condens. Matter **12**, L303 (2000).
- [43] E. Slot, M.A. Holst, H.S.J. van der Zant, and S.V. Zaitsev-Zotov, Phys. Rev. Lett. **93**, 176602 (2004).
- [44] A.N. Aleshin, H.J. Lee, Y.W. Park, and K. Akagi, Phys. Rev. Lett. **93**, 196601 (2004).
- [45] H.J. Schulz, G. Guniberti, P. Pieri, in *Field Theories for Low-Dimensional Matter Systems*, (G. Morandi et. al., Eds.), Springer, N-Y, 2002.
- [46] K. Sasaki, Phys. Rev. B **65**, 195412 (2002).
- [47] S. Iijima, Nature (London) **354**, 56 (1991).
- [48] S. Iijima and T. Ichihashi, Nature (London) **363**, 603 (1993).
- [49] H. Ajiki and T. Ando, J. Phys. Soc. Jpn. **65**, 505 (1996).
- [50] T. Ando, J. Phys. Soc. Jpn. **74**, 777 (2005).
- [51] R. Egger and A.O. Gogolin, Eur. Phys. J. B **3**, 281 (1998).
- [52] X. Blase, L.X. Benedict, E.L. Shirley, and S.G. Louie, Phys. Rev. Lett. **72**, 1878 (1994).
- [53] O.M. Yevtushenko, G.Ya. Slepyan, S.A. Maksimenko, A. Lakhtakia, and D.A. Romanov, Phys. Rev. Lett. **79**, 1102 (1997).
- [54] S.G. Louie in *Carbon Nanotubes*, M.S. Dresselhaus, G. Dresselhaus, Ph. Avouris (Eds.), Topics Appl. Phys. **80**, 113 (2001), Springer, Berlin 2001.
- [55] R. Egger, A.O. Gogolin, Phys. Rev. Lett. **79**, 5082 (1997).
- [56] I. Kuzmenko, S. Gredeskul, K. Kikoin, and Y. Avishai, Low Temp. Physics, **28**, 539 (2002) [Fiz. Nizkikh Temp., **28**, 752 (2002)].

- [57] K. Kikoin, I. Kuzmenko, S. Gredeskul, and Y. Avishai, in *Proceedings of NATO Advanced Research Workshop “Recent Trends in Theory of Physical Phenomena in High Magnetic Fields”* (Les Houches, France, February 25 – March 1, 2002), p.89.
- [58] I. Kuzmenko, S. Gredeskul, K. Kikoin, and Y. Avishai, *Phys. Rev. B* **67**, 115331 (2003).
- [59] S. Gredeskul, I. Kuzmenko, K. Kikoin, and Y. Avishai, *Physica E* **17**, 187 (2003).
- [60] S. Gredeskul, I. Kuzmenko, K. Kikoin, and Y. Avishai, *Proceeding of NATO Conference MQO*, Bled, Slovenia, September 7-10, 2003, p.219.
- [61] I. Kuzmenko, S. Gredeskul, K. Kikoin, and Y. Avishai, *Phys. Rev. B* **69**, 165402 (2004).
- [62] I. Kuzmenko, S. Gredeskul, *HAIT. Journal of Science and Engineering* **1**, 130 (2004).
- [63] I. Kuzmenko, *Nanotechnology* **15**, 441 (2004).
- [64] F. Stern, *Phys.Rev. Lett.* **18** 546 (1967).
- [65] I. Kuzmenko, S. Gredeskul, K. Kikoin, and Y. Avishai, *Phys. Rev. B* **71**, 045421 (2005).
- [66] I. Kuzmenko, *Physica B* **359-361**, 1421 (2005).